To the Graduate Council:

I am submitting herewith a dissertation written by George Richard Dyer entitled "Time-Resolved X-ray Energy Spectrometry as a Plasma Diagnostic Method for the Oak Ridge Tokamaks." I recommend that it be accepted in partial fulfillment of the requirements for the degree of Doctor of Philosophy, with a major in Physics.

Owen C. Eldridge, Major Professor

We have read this dissertation
and recommend its acceptance:

Accepted for the Council:

Vice Chancellor
Graduate Studies and Research

TIME-RESOLVED X-RAY ENERGY SPECTROMETRY AS A PLASMA DIAGNOSTIC METHOD FOR THE OAK RIDGE TOKAMAKS

A Dissertation

Presented for the

Doctor of Philosophy

Degree

The University of Tennessee, Knoxville

George Richard Dyer

March, 1980

THIS DISSERTATION

IS DEDICATED TO

MY TEACHERS

ACKNOWLEDGMENTS

So many people have helped me in this project that a complete list of names is impractical, but I am grateful for the assistance they gave. Several people have provided special aid, and I want to thank them specifically.

Phil Edmonds prodded and advised me and served as devil's advocate through these five years of research. Sam DeCamp provided necessary mechanical assistance, especially during the rush jobs. Bill Wagner and Dennis Webber helped with troubleshooting, installation and maintenance of the equipment. Russ Overbey, Ann Stewart, and Harold Ketterer wrote the computer programs which made the data collection and processing possible.

George Kelly and Hutch Neilson helped with a variety of electronic, mathematical, and theoretical problems. Julian Dunlap, Glen Haste, and Masanori Murakami were always willing to explain plasma physics to a novice. Charles Crume and Don Arnurius gave special assistance with the RECNO calculations.

My thesis committee, L. A. Berry, O. C. Eldridge, J. L. Dunlap, E. G. Harris, R. L. Becker, and E. J. Kennedy, were patient and willing to grant the extension necessary for completion of this thesis. O. B. Morgan, John Sheffield, and Mike Saltmarsh were generous in allowing me to pursue the research, and Jim Pearce and Jim Madison helped relieve the pressures of my routine responsibilities. R. P. Jernigan provided administrative help many times.

Special thanks go to the people who rescued me in these last hurried days: Gene Watkin, Judy Neeley, Susan Bell, Sandra Schwartz and Jane Martin, who prepared the figures, and Terry Hagan, who typed, proofread, corrected, and re-typed through several rearrangements of the thesis.

Craig Harris said the magic words, "you'll never finish!" in 1965; my wife, Barbara, has encouraged me when I thought those words were true.

To all of you, and to many more not named, my sincerest thanks. I could not have finished without your help.

ABSTRACT

A method for measuring electron temperature (T_e) and estimating effective ionic charge (Z_{eff}) of a tokamak plasma by x-ray energy spectrometry is described. With a ten-millisecond time resolution, the technique defines values of T_e and Z_{eff} throughout the duration of single tokamak discharges.

A discussion of the x-ray emission spectrum from a tokamak plasma is presented, and the complicating effects of plasma-detector geometry, plasma temperature and density profiles, and impurity radiation are analyzed. The necessary data collection system is described, and the consequences of finite energy resolution, pulse pileup, and other deleterious effects are investigated. Results of these considerations are combined in a procedure to calculate T_e and Z_{eff} from x-ray energy data and plasma density information, and to estimate the accuracy and reliability of the derived values.

The computational procedure is applied to five different classes of tokamak discharges and the results are compared with T_e and Z_{eff} values independently derived through a Thomson-scattering diagnostic. These comparisons show that, in general, agreement between the x-ray diagnostic and accepted techniques is good, and demonstrate the advantages of a time-resolved measurement capable of spanning an entire discharge. Where discrepancies do exist between x-ray and Thomson-scattering results, there is other evidence that the basic physics of those particular discharges is not understood. It is

concluded that the x-ray technique provides a useful and unique on-line diagnostic, yielding T_e and Z_{eff} determinations in good agreement with other measurements for well-behaved plasmas, and providing additional information to aid in understanding anomalous ones.

TABLE OF CONTENTS

LIST OF TABLES

LIST OF FIGURES

CHAPTER 1

X-RAY DIAGNOSTIC TECHNIQUES FOR PLASMAS

1.1 INTRODUCTION

One of the most successful magnetic confinement systems in current fusion research is the tokamak, a machine in which a toroidal plasma is confined by the synchronous action of a strong toroidal magnetic field, a poloidal field due to current flowing in the plasma, and a weak vertical field which controls plasma expansion along the major radius of the torus. The literature contains major review articles on tokamak design and operation.[1,2]

Tokamak research became a part of the fusion effort at Oak Ridge in 1971, when ORMAK became operational. Until that time, the program at ORNL had concentrated on steady-state confinement techniques. Since a tokamak is a pulsed experiment, with a discharge duration of 100-300 ms in machines such as ORMAK, plasma diagnostics which could follow the rapid temporal evolution of tokamak plasmas were required. A part of the research effort in the Fusion Energy Division was thus applied to diagnostic development. The apparatus to be described here was initially conceived as providing a plasma temperature determination by the technique of x-ray energy spectrometry of bremsstrahlung; the measurement was to span the complete plasma discharge and yield 10-ms time resolution. During successive applications to ORMAK, ISX-A, and ISX-B, the technique has been developed to give a time-resolved estimate of plasma Z_{eff} as well,

using contemporaneous electron density data from a microwave interferometer.

1.2 SURVEY OF PREVIOUS WORK

Since electromagnetic radiation is one of the principal mechanisms for energy loss from a hot ionized gas,[3] or plasma, it is reasonable that spectrometry of the escaping radiant energy is an important diagnostic tool for determining plasma parameters. Radiation is produced as a result of the acceleration of charged particles. The least massive particles are the most easily accelerated, so electrons are responsible for most of the radiation loss from plasmas. Depending on the specific process, electron-produced radiation falls into one of four categories.[4] Bremsstrahlung is produced during an elastic coulomb collision between an electron and a positive ion; this is sometimes called free-free radiation because the electron is free before and after the collision. If the electron is captured by the ion, recombination or free-bound radiation results. When the electron passes from a higher- to a lower-energy bound state in a partially ionized atom, line or bound-bound emission occurs. The circular motion of an energetic free electron in a magnetic field produces the fourth category, electron cyclotron radiation.

The maximum energy of radiation from a plasma depends on the temperature of the electrons. For plasmas with an electron temperature of 10^7 degrees K, or about 10^3 eV, typical of many past and current thermonuclear experiments, bremsstrahlung and recombination spectral energies extend to the 1-10 keV soft x-ray

range. Thus, analysis of soft x radiation should provide useful diagnostic information in this temperature regime.

1.2.1 Absolute Intensity Techniques

The simplest use of x-ray emission is in visualizing the plasma. Various researchers have employed pinhole cameras to study regions of intense emission in a variety of machines.[5-7] Usually sources of hard x-rays, such as regions where high-energy "runaway" electrons hit limiters or vacuum vessel walls, dominate x-ray pictures of tokamaks.

The intensity of the radiation from a plasma is a function of its composition, density, and temperature. Assuming composition and density are known, plasma temperature can be inferred from the absolute intensity of x-ray emission. This technique was used to estimate temperatures in the Scylla theta-pinch experiment,[8] but results were misleading because assumptions for the plasma composition were wrong.

1.2.2 Filter and Detector Method

Some form of spectrometry is needed if any information besides total intensity is to be gained from the plasma x radiation. The simplest x-ray detector is photographic film. By combining film with absorbing filters, an x-ray spectrum can be inferred from exposures at two or three energy intervals. This method has been investigated by workers at the Naval Research Laboratory and its use on tokamaks has been suggested.[9]

Film is relatively insensitive as an x-ray detector, and provides no time resolution. An electronic detector can overcome both these

difficulties. The first application of this technique in thermonuclear research combined plastic scintillators and photomultipliers with absorption filters to measure electron temperatures in Scylla.[10]

Better detectors have simplified the filter technique. Several types of semiconductor diode detectors are currently available and offer fast time response and good efficiency over the soft x-ray energy range. Researchers at Frascati have investigated the use of metallic filters and silicon diodes to measure temperatures of thermonuclear plasmas.[11]

1.2.3 Diffraction Spectrometry

While filter-detector methods provide some spectral information, energy resolution is poor enough to require assumptions about detailed spectral shape. This disadvantage is eliminated by diffraction spectrometry, a technique with intrinsically good wavelength resolution. Diffraction spectrometers have been used to identify plasma impurities by line radiation as well as to define thermal spectra.[12] A curved-crystal spectrometer with a position-sensitive detector has been proposed as a tokamak diagnostic at PPPL.[13]

1.2.4 Energy Spectrometry

The advent of semiconductor detectors with both high efficiency and good energy resolution presented an effective alternative to diffraction spectrometry. By the late 1960's, lithium-drifted silicon detectors with energy resolution of 150 eV at 1 keV were commercially available.[14] These detectors have been applied to a variety of plasma

devices, including the tokamaks at Princeton, Massachusetts Institute of Technology, Fontenay aux Roses, and Oak Ridge.

The most elaborate energy spectrometry system is installed on the Princeton PDX device. Twelve separate detectors are employed in four arrays. Each detector in an array covers a part of the x-ray spectrum defined by absorption filters, and each array collects x-ray data from a different chord through the plasma. Data collection, aperture selection, and detector position are computer controlled. The x-ray spectrometer is a major diagnostic on the PDX, providing electron temperature and profile measurements. Time resolution is 60 ms. Conventional pulse-height analysis techniques are used, and pulse pileup is eliminated by using three energy channels and commercial pileup rejection systems.[15]

A simpler spectrometer has been used at MIT to provide x-ray spectral information. The single detector system is gated on for times as short as 1 ms, and spectra are collected over 20 plasma discharges.[16]

A third system has been used on the WEGA experiment in France. Published specifications give 5-ms time resolution and four spectra per discharge with 350 eV energy resolution. The system uses a single detector with pulsed-optical feedback and a parallel pulse-height analyzer. A temperature is computed directly from the energy spectrum, with no corrections for profile or impurity effects.[17]

At Oak Ridge, a single detector with pulsed-optical feedback and a conventional multichannel analyzer was used on ORMAK to obtain soft x-ray spectra. Severe count rate limitations and susceptibility to

overloads caused by hard x-rays limited its usefulness. Spectra were integrated over several discharges to obtain adequate statistics.[18,19]

1.3 OBJECTIVES OF PRESENT WORK

The limitations of the original soft x-ray energy spectrometer on ORMAK motivated a proposal for a system which would work at higher count rates, recover quickly from overloads, and resolve line radiation from any metallic impurities which the plasma might contain. Previous experience with silicon detectors[20] suggested that energy resolution of better than 500 eV could be attained at counting rates of over 10^5 per second. Thus, a system which could acquire a spectrum within the time span of a single tokamak discharge seemed realizable.

1.3.1 Time Resolution Throughout a Plasma Discharge

Discussions with several members of the Fusion Energy Division Staff emphasized the importance of time resolution in tokamak diagnostic information. A typical discharge for the Oak Ridge tokamak lasts 150-250 ms, and a typical neutral-particle injector pulse lasts 40-100 ms, so a diagnostic time constant that is short in comparison with these intervals is required. On the other hand, an energy spectrometer is basically a pulse-height analyzer, and so must process each detected photon individually. At the highest rate considered feasible, $\sim 10^5$ pulses can be analyzed per second. Statistical validity requires approximately 10^3 counts per spectra, so a minimum counting time of 10 ms per spectrum seems practicable.

A second aspect of time resolution involves continuity of measurement. For example, the Thomson-scatter measurement takes place

in approximately 50 ns, but a maximum of only four measurements per tokamak cycle is possible. Thus, to span a plasma discharge cycle with 10 ms resolution, Thomson-scattering data must be accumulated during several successive discharges. Interesting nonrepetitive events will likely be missed, unless an alternate diagnostic method is provided to examine the complete time span of each discharge. These considerations set the first objective of the x-ray energy spectrometer: continuous coverage of each plasma discharge with a time resolution of 10 ms.

1.3.2 Electron Temperature Information

An obvious parameter for an x-ray energy spectrometer to measure is electron temperature, T_e, since intensity vs energy for a bremsstrahlung spectrum is given by the simple expression[21]

$$I(E) = C\, e^{-E/T_e} \qquad (1\text{-}1)$$

X rays from all positions along the central chord of the plasma contribute to an observed spectrum, and this was expected to complicate the spectral analysis and interpretation. Nevertheless, the x-ray temperature measurement was expected to correlate with and complement the Thomson-scattering data for a given discharge, and to yield a T_e vs time plot like that of Fig. 1-1.

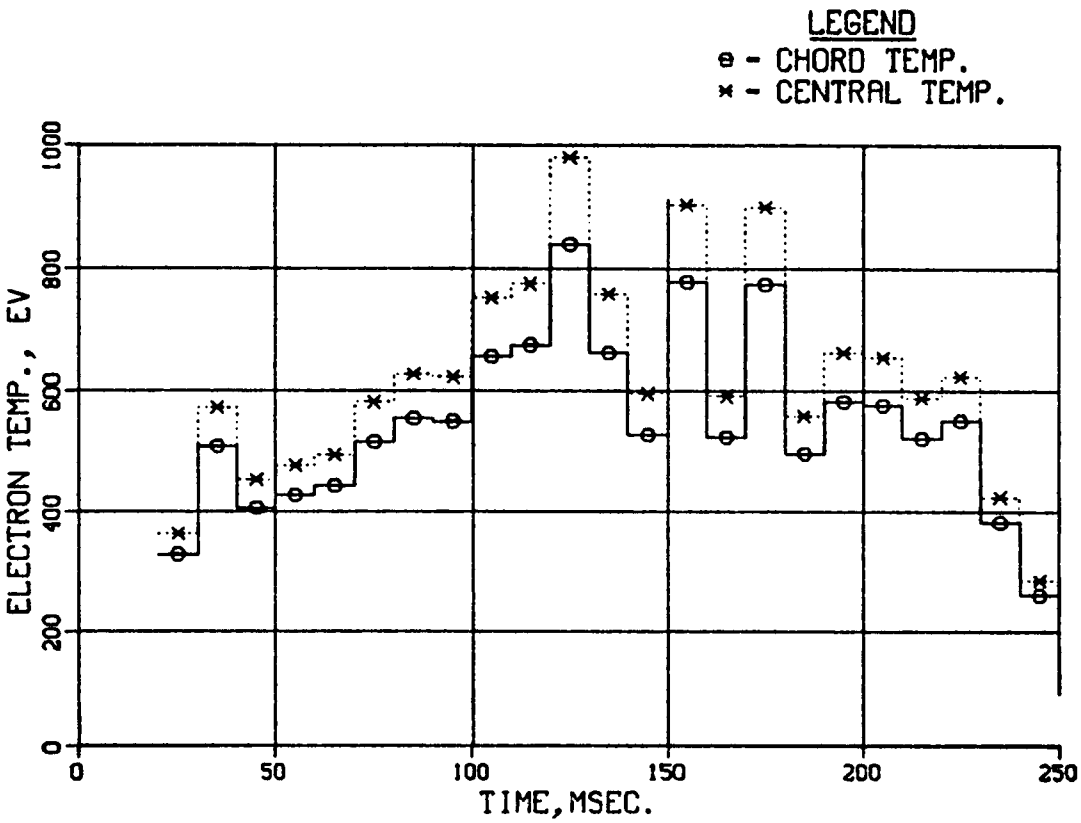

FIGURE 1-1. A plot of chord-integral and peak electron temperatures as a function of time for a tokamak discharge

1.3.3 Qualitative Plasma Information

An energy spectrum carries a great deal of information in addition to electron temperature. If the plasma contains impurity species such as iron or copper, these elements radiate a line spectrum which is detectable at a glance. Non-equilibrium plasma conditions appear as a deviation from linearity in the intensity plot or as a composite with more than one slope. Conversely, a well-behaved plasma yields a linear spectrum with no striking features. Thus, an examination of the x-ray energy spectrum as a function of time would provide a quick appraisal of plasma conditions. Figure 1-2 illustrates a possible spectral display, showing characteristic iron radiation at ~6.4 keV.

1.3.4 Quantitative Impurity Measurement

The spectrometer had actually been in use for some time when a careful consideration of error sources and their effects on energy data revealed that small concentrations of impurities in the plasma influence the shape as well as the relative intensity of the observed x-ray spectra. During a discussion of impurity effects, it was suggested that the x-ray data might be used in conjunction with microwave measurements of electron density to provide time-resolved estimates of plasma impurity concentration or effective ion charge, Z_{eff}.

This objective is more difficult than the preceding ones, since Z_{eff} measurements require a determination of absolute intensities as well as detailed calculations of enhancement of x-radiation by plasma impurities. Further, enhancement factors depend on details of plasma

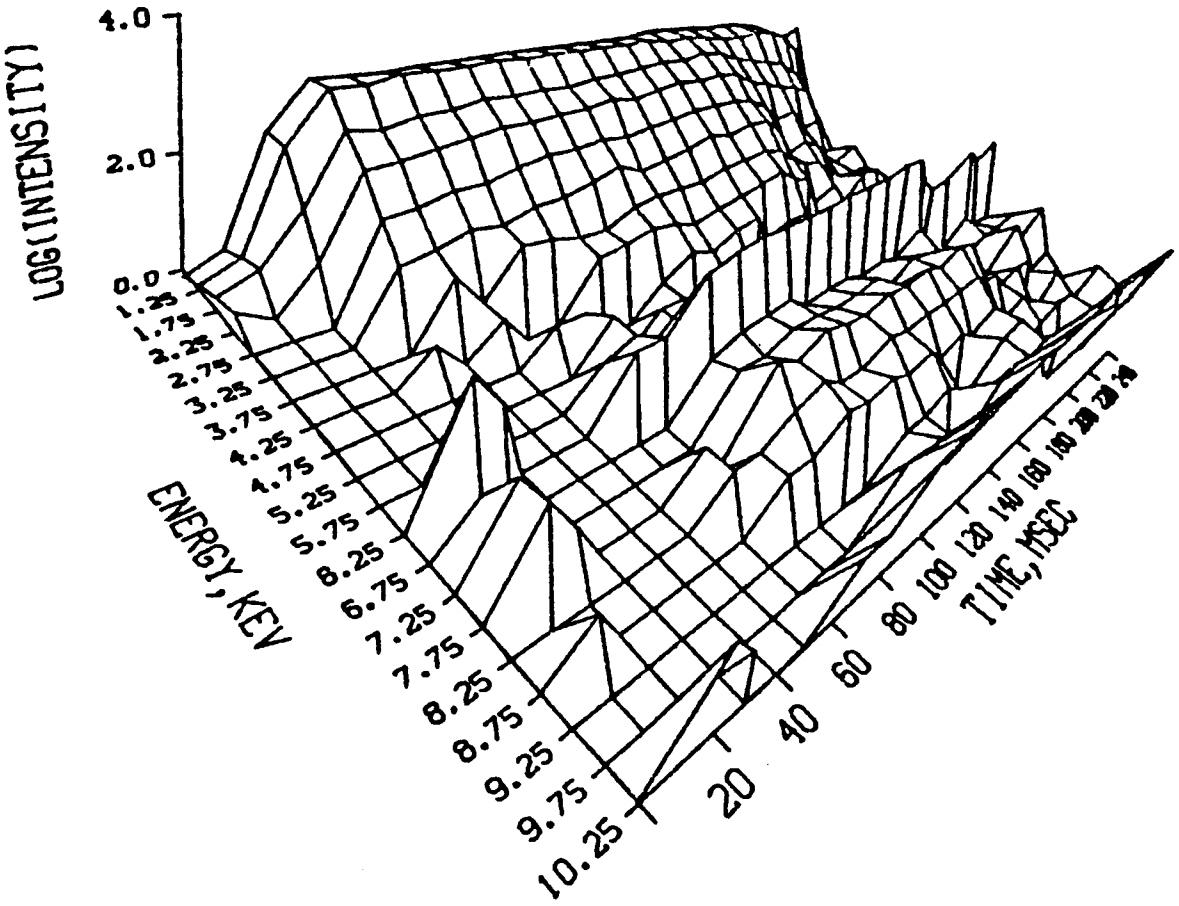

FIGURE 1-2. A three-axis plot showing the time evolution of soft x-ray energy spectra during a tokamak discharge

temperature, density, and impurity distribution as a function of radius along the spectrometer viewing chord. Provided a satisfactory computational model can be devised, x-ray and density data can be combined to estimate Z_{eff} as a function of time, as illustrated by Fig. 1-3. This estimate is independent of the usual Spitzer resistivity calculation.

1.3.5 System Simplicity

The final objective can more properly be called a constraint, since a limited budget and restricted access to the tokamak itself confined the x-ray experiment to a single-chord, single-detector system. From an operating standpoint, this is an advantage, since one spectrometer is simpler to use and maintain than a multiple system. However, data reduction and error correction must depend on calculated effects derived from mathematical plasma models to a greater extent than would be necessary for a system which provided spatial information as well as energy spectra.

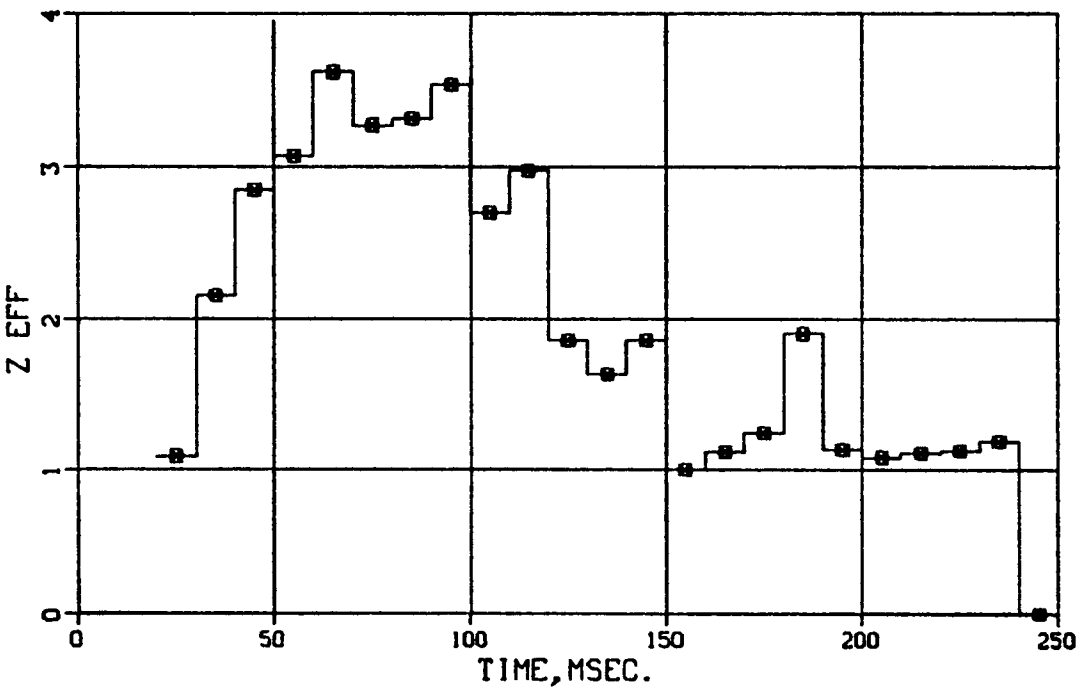

FIGURE 1-3. A plot of Z_{eff} vs time as derived from x-ray energy spectrometer and microwave interferometer data collected during a tokamak discharge

CHAPTER 2

THEORY OF MEASUREMENTS

2.1 INTRODUCTION

A hot plasma is a copious source of electromagnetic radiation. The intensity and spectral distribution of the radiation is a function of plasma temperature, density, composition and geometry. Given a geometry, an experimental determination of the other three parameters is necessary for an understanding of plasma heating and confinement. For tokamak plasmas with temperatures in the vicinity of 1 keV, analysis of the x-ray spectrum in the 1-10 keV energy range can provide information on electron temperature and plasma purity.

Since any single method of measurement has its specific limitations, a variety of diagnostic techniques for any given plasma parameter is desirable. An examination of results of several methods, and a consideration of the distinctive aspects of each, increases confidence in the conclusions drawn, and provides insights which a single technique could not furnish. A comparison of the x-ray energy spectrometry method with other techniques for temperature and impurity determinations points out some of these aspects.

2.2 ALTERNATE METHODS FOR MEASURING T_e

Several methods have been used for determining or estimating electron temperature (T_e) during the history of fusion energy research. Some of these do not extend to the temperature range produced in tokamaks, and some are experimentally so difficult that they have fallen into disuse. For tokamaks, temperature

determinations by diamagnetic measurements and by optical spectrometry are generally in the last category and will be mentioned for historical interest. The three methods most used at present include Thomson scattering of ruby laser light, observation of electron cyclotron radiation intensity, and measurement of thermal x-ray spectral intensity vs energy.

2.2.1 T_e From Diamagnetic Measurements

When a plasma exists in a strong magnetic field, the electrons and ions move in spiral orbits around the field lines.[22] The spiral motion, by Lenz's law, generates a magnetic field which opposes the applied field, and so the plasma exhibits diamagnetism. The change in the magnetic flux within the plasma during a tokamak discharge is related to the plasma current, pressure, and minor radius by the relation[23]

$$\delta\phi = \frac{2\pi}{c^2 H_\theta} (I^2 - 2\pi a^2 p) . \qquad (2\text{-}1)$$

If $\delta\phi$, I, and a can be measured, the plasma pressure p can be calculated, and the thermal energy in the plasma can be found by the relation

$$a^2 p = \frac{2W}{3\pi} . \qquad (2\text{-}2)$$

The thermal energy is related to plasma density, ion temperature and electron temperature by the integral

$$W = \int n_e \, (T_e + \gamma T_i) \, dS \qquad (2\text{-}3)$$

over the plasma cross section. For reasonable models of temperature and density dependence along the minor radius a, the value of $(T_e + \gamma T_i)$ can be calculated when the density n_e is known. When γT_i is small compared to T_e, the diamagnetic effect provides a method of determining T_e.

In practice, a diamagnetic measurement is a delicate experiment, involving a small difference in large signals from various magnetic circuits associated with the tokamak. Modern SCR supplies commonly used to power the field-producing windings add electrical noise which is difficult to filter out.[24] In addition, the tokamak is inherently a low-β machine, so the diamagnetic effect is small. All these factors combine to make the diamagnetic technique hard to use, compared to methods which measure electron motion directly.

2.2.2 T_e From Optical Spectrometry

One direct measurement of internal plasma conditions is given by optical spectrometry of line radiation from heavy impurity species. Although the plasma is mostly pure hydrogen, enough atoms of heavier elements are present to contribute a significant fraction of the total radiant energy loss. Metallic impurities such as iron, nickel, and

chromium from stainless steel vacuum components have excitation energies too high to become completely ionized at present tokamak plasma temperatures, so these elements produce line radiation in the ultraviolet and soft x-ray regions. The relative intensities of discrete lines at two excitation energies $W_1 < W_2$ are governed by the ratio

$$\ell n\ I_1 - \ell n\ I_2 = (W_2 - W_1)/kT_e \qquad (2\text{-}4)$$

at least to a first approximation.[25] Thus, the local plasma temperature can be determined in principle by a measurement of the intensity ratio of line radiation.

In practice, accurate measurements of intensity ratios in the ultraviolet region are difficult, involving elaborate calibrations because optical components and detectors exhibit energy-dependent characteristics. Very complex optical spectra and varying background radiation add to the difficulties encountered in using this method to measure T_e.

2.2.3 T_e From Electron Cyclotron Radiation

The spiral motion of plasma electrons in a magnetic field has been mentioned earlier. These accelerated electrons radiate at the cyclotron frequency[26]

$$\omega_e = \frac{eB}{mc} \qquad (2\text{-}5)$$

so frequency is directly proportional to magnetic field strength, a quantity which is known as a function of machine geometry and coil currents. Thus, radiation from any point within the plasma can be monitored by tuning to the cyclotron frequency corresponding to the field at that point. For a fixed cyclotron frequency, the intensity of the emitted radiation is a function of electron temperature.[27]

These characteristics suggest that electron cyclotron radiation provides an accurate profile measurement of electron temperature (i.e., temperature as a function of plasma minor radius). However, the intensity function is complicated by such variables as plasma opacity, reflections in the containment vessel, waveguide geometry, and receiving technique; the electron-cyclotron spectrometer must be calibrated against a source of known temperature (or by another method which measures absolute temperature) in order to provide quantitative temperature information.[28]

2.2.4 T_e From Thomson-Scattering Measurements

A diagnostic method which does provide an absolute temperature determination for hot electrons uses the Doppler-shifted spectrum of a Q-switched ruby laser focussed at the spatial point of measurement. The laser provides an intense light pulse with a narrow optical bandwidth, lasting ~10 ns. The spectrum of the light which is Thomson-scattered by plasma electrons is analyzed; for a Maxwellian electron distribution, this spectrum has a Gaussian profile centered

on the laser frequency, with half-width depending on temperature according to the relation[29]

$$I(\nu - \nu_o) = C_1 e^{-C_2/T_e} \qquad (2\text{-}6)$$

The laser method is unique in providing an absolute temperature measurement at a localized (in space and time) plasma point. It requires rather sophisticated apparatus for successful implementation, great care in design to maximize signal-to-noise ratio in the spectrometer and subsequent electronics,[30] and is usually restricted to one to four measurements per plasma discharge because of laser duty-cycle limitations. However, its singular spatial and temporal resolution has led to its almost universal application as a tokamak diagnostic technique.

2.2.5 T_e From X-ray Spectrometry

A second technique which provides an absolute temperature measurement is spectrometry of the thermal x rays emitted by a hot plasma. For bremsstrahlung from a hydrogen plasma with electrons at temperature T_e, the x-ray intensity as a function of energy is given as[31]

$$dI(E) = C\, e^{-E/T_e}\, dE \qquad (2\text{-}7)$$

so temperature can be found as the negative inverse slope of $\ell n(I)$ vs E.

In practice, the simple relation of Eq. (2-7) is complicated by plasma temperature and density profiles, impurity species, and several less important effects. The method provides measurements throughout a tokamak discharge with ~10 ms time resolution, and the equipment comprised by the spectrometer is relatively simple. In addition to temperature, the x-ray method provides information on plasma impurity content.

2.3 ALTERNATE METHODS FOR MEASURING Z_{eff}

A central problem of current fusion energy research is the control of impurity species (i.e., any element except hydrogen) in experimental plasmas. Since radiation losses are enormously enhanced by the presence of heavy ions,[32] it is essential to the success of a fusion reactor to eliminate these impurities. The purity of a plasma can be measured by its "effective ionic charge" (Z_{eff}) defined as[33]

$$Z_{eff} = \frac{\Sigma\ N_i\ Z_i^2}{\Sigma\ N_i\ Z_i} \qquad (2\text{-}8)$$

where the sum is taken over the impurity species that are present, and Z_i is the charge carried by the (positive) species ion. For a pure hydrogen plasma, $Z_{eff} = 1$.

The measurement of plasma Z_{eff} is more difficult than a temperature determination. Z_{eff} is a sum of terms, because several

impurity species are present at once. A complicated spatial distribution depending on profiles of density, temperature and impurity concentration, as well as transport phenomena which influence species ionization states, makes a direct measurement of Z_{eff} impossible. Instead, Z_{eff} is estimated by comparing experimental results with calculations made from mathematical plasma models.

2.3.1 Z_{eff} From Plasma Resistance Measurements

A tokamak is essentially an electrical transformer with the plasma serving as a single-turn secondary winding and carrying a current of $\sim 10^5$ A (in the Oak Ridge machine). The plasma current is driven by a loop voltage; both current and voltage are measured as a function of time for every discharge. An application of Ohm's law produces an effective resistance as a function of time for each discharge.

The resistivity of a plasma with a given temperature and ionic charge has been calculated by Lyman Spitzer and his colleagues; the equation is[34]

$$\rho = C\, Z\, T_e^{-3/2}\, \ell n\, \Lambda \qquad (2\text{-}9)$$

where C and Λ have been tabulated for various conditions. If the temperature profile is known at some time during a discharge cycle, the effective resistance expected for a pure hydrogen plasma (Z = 1) can be calculated by using Eq. (2-9) in a surface integral over the plasma cross section. The ratio of the experimental effective

resistance to that found from the hydrogen model produces an estimate of $Z \sim Z_{eff}$.

Since profile measurements at Oak Ridge are provided by the Thomson-scattering diagnostic, several discharges are required to produce a profile, and the profile is measured at a specific time during the plasma discharge. The resistive method thus produces averaged measurements for a sequence of discharges, for discrete times during the discharge. Uncertainties in Z_{eff} estimates are introduced by electrical noise on voltage and current signals.

2.3.2 Z_{eff} by Ion Scattering

Experimental observations of scattered high-energy ions from the tokamak plasma can also be used to find Z_{eff}.[35] If an energetic beam of neutral hydrogen is injected tangentially to the plasma current flow, the fast ions resulting from charge exchange interactions will be scattered by the cooler ambient plasma. The number of scattered fast ions and the magnitude of the scattering angle are both greater if the ambient plasma contains heavy impurities, so a plasma with a high Z_{eff} will scatter fast ions more effectively than a pure hydrogen plasma. The spectrum of scattered ions is obtained by the charge-exchange spectrometer on the tokamak. Expected spectra can be calculated for various profiles of temperature, density, and impurity distribution, using the impurity species suspected to be present in the plasma. Matching observed and calculated spectra yield a Z_{eff} estimate.[36]

The ion-scattering method is limited to experiments involving neutral beam injection. The injectors contribute their own impurity

species to the plasma and further complicate Z_{eff} estimates. Extensive calculations involving many plasma parameters are necessary to produce the comparison spectra used in this technique, and the specific models employed in the calculations affect the end result. The charge-exchange spectrometer does collect several spectra during a single neutral beam injection pulse and thus provides time-resolved Z_{eff} measurements.

2.3.3 Z_{eff} by X-ray Intensity Measurements

The intensity of the plasma x-ray emission is enhanced by impurity species. The intensity distribution of a thermal spectrum depends on electron density, electron temperature, and the particular impurities present in the plasma. If the electron density and profile are known, the intensity expected from a pure hydrogen plasma can be calculated for the geometrical parameters of the spectrometer, using the temperature information provided by the $\ell n(I)$ vs E data. The ratio of observed spectral intensity to that calculated for pure hydrogen is the enhancement produced by plasma impurities.

For the same geometrical arrangement, intensities can be calculated for various concentrations of impurities. As usual, the calculations are made for specific models of density and temperature and for particular impurity species. Enhancement factors can be calculated as a function of temperature and Z_{eff}. Thus, for a given temperature and enhancement, Z_{eff} can be estimated.

Electron density vs time is available from microwave measurements for most tokamak discharges. The x-ray spectrometer provides T_e measurements, so Z_{eff} estimates with 10 ms resolution are provided by

this method. As it turns out, results are not strongly affected by the specific density and temperature models used in enhancement calculations, but are dependent on the impurity species.

For any of the methods discussed, the determination of a numerical value for Z_{eff} depends on modelling calculations as well as experimental results. However, each of the methods uses a unique set of parameters, so a comparison of results from the three techniques is desirable.

2.4 THE X-RAY SPECTRUM FROM A HOT PLASMA

The problem of calculating x-ray intensity as a function of energy has been the focus of much theoretical effort, beginning with Kramers in 1923.[37] He derived an expression for bremsstrahlung intensity vs energy by using the classical formula for radiation from a decelerating electron and applying Bohr's correspondence principle to the results to limit the maximum energy of emitted x-rays. This semiclassical formula was corrected by Gaunt[38] to include quantum-mechanical effects. Later workers generalized the intensity expression to include radiation from free-bound as well as free-free electron-ion interactions.[39]

The complete expression for x-ray intensity incident on the spectrometer detector from the tokamak plasma is a function of many parameters. Basic spectrometer characteristics such as efficiency and energy resolution modify the differential intensity equation, and plasma-detector geometry limits the radiation incident on the detector. Plasma profile effects and composition further alter the basic expression. Beginning with the formula for radiation from a

pure hydrogen plasma, these various complicating factors will be considered in sequence.

2.4.1 The Spectrum From a Uniform Hydrogen Plasma

At thermonuclear temperatures, pure hydrogen is fully ionized, so its x-ray emission is by bremsstrahlung, or free-free radiation. The bremsstrahlung intensity per unit frequency interval per second emitted by N_e electrons per cm^3 interacting with N_i ions per cm with nuclear charge Z_i is[40]

$$dI_\nu(\nu) = A\, N_e\, N_i\, Z_i^2\, (\chi_H/kT_e)^{1/2}\, \bar{g}_{ff}\quad e^{-h\nu/kT_e}\, d\nu \qquad (2\text{-}10)$$

where χ_H is the ionization energy of hydrogen, $\bar{g}_{ff}$ is the free-free Gaunt factor average over a Maxwellian velocity distribution corresponding to the temperature T_e, and A has the value

$$A = \frac{32\,\pi^{1/2}\, e^4\, h}{3^{3/2}\, c^3\, m_e^2} = 11.72 \times 10^{-40}\ \text{erg} \cdot \text{cm}^3 \qquad (2\text{-}11)$$

In terms of unit energy interval, the intensity per steradian for hydrogen ($N_e = N_i$, $Z_i = 1$) becomes

$$d\, I_\nu(E) = C\, N_e^2\, T_e^{-1/2}\, e^{-E/T_e}\, dE \qquad (2\text{-}12)$$

where E, T_e, and χ_H are in units of eV, $\bar{g}_{ff} = 1$, and the constant C is

$$C = \frac{A\,\chi_H^{1/2}}{4\,\pi\,h} = 7.63 \times 10^{-15}\ (eV)^{1/2}\ cm^3\ s^{-1} \qquad (2\text{-}13)$$

Since the x-ray spectrometer produces an energy spectrum, Eq. (2-12) is the form needed to calculate the spectrometer response for hydrogen bremsstrahlung.

Since the energy spectrometer has a finite energy resolution ΔE, determined largely by the 500 eV energy span per pulse-height analyzer channel, and requires a finite time Δt = 10 ms to acquire a spectrum, the spectrum must be described by an integral of Eq. (2-12) over ΔE and Δt. For a channel j with an average energy E_j and energy limits $(E_j - \Delta E/2,\ E_j + \Delta E/2)$ the integrated intensity

$$I_V(E_j) = C\ N_e^2\ T_e^{-1/2} \int_o^{\Delta t} dt \int_{E_j - \Delta E/2}^{E_j + \Delta E/2} e^{-E/T_e}\ dE \qquad (2\text{-}14)$$

or

$$I_V(E_j) = 2C\ \Delta t\ N_e^2\ T_e^{1/2}\ \sinh\ (\Delta E/2T_e)\ e^{-E_j/T_e} \qquad (2\text{-}15)$$

Equation (2-15) gives the intensity from a unit volume (1 cm^3) of plasma, integrated over the spectrum acquisition time and the channel energy width. A third integral over the plasma volume within the

field of view of the detector is necessary to compute the total intensity recorded at energy E_j:

$$I(E_j) = \int_V \Omega \; I_V(E_j) \; dV \qquad (2\text{-}16)$$

where Ω is the solid angle subtended by the exposed area of the detector at the plasma volume element dV.

As described in Appendix A, Section A.3, the plasma volume which illuminates the detector is approximately a cylinder with diameter d_p and length 2a, where a is the minor radius of the plasma torus (a = 25 cm in ISX, 20 cm in ORMAK). The integral for $I(E_j)$ becomes

$$I(E_j) = \Omega \; I_V \; (E_j) \int_{-a}^{a} \pi \; (d_p/2)^2 \; dr \qquad (2\text{-}17)$$

since $I_V(E_j)$ is independent of position in the plasma volume. The final expression for $I(E_n)$ is

$$I(E_j) = \pi \; \Omega \; C \; R \; \Delta t \; d_p^2 \; N_e^2 \; T_e^{1/2} \; \sinh \; (\Delta E/2T_e) \; e^{-E_j/T_e} \qquad (2\text{-}18)$$

Equation (2-18) gives the calculated integral intensity stored in channel j during a 10 ms counting interval. An energy spectrum is made up of data from several adjacent channels. If typical values Ω = 4.52×10^{-8} steradians and d_p = 0.399 cm are taken from Table A-2 and inserted with the numerical values T_e = 1000 eV, N_e = 5×10^{13} per

cm^3, $C = 7.63 \times 10^{-15}$, a = 25 cm, ΔE = 500 eV and Δt = 10 ms into Eq. (2-18), a spectrum can be calculated. Table 2-1 gives the results.

If a plot of $\ell n\ I(E_j)$ vs E_j is made, the resulting points fall on a straight line, as shown in Fig. 2-1. This line can be defined mathematically by fitting the standard straight line equation

$$Y = mX + b_o \tag{2-19}$$

to the given points $(\ell n\ I(E_j),\ E_j)$ listed in Table 2-1 by the standard least-squares method.[41] When this is done, m and b_o are given by the expressions

$$m = \frac{K \Sigma\ E_j\ \ell n\ I(E_j) - \Sigma\ E_n\ \Sigma\ \ell n\ I(E_j)}{K \Sigma\ (E_j)^2 - (\Sigma\ E_j)^2} \tag{2-20}$$

and

$$b_o = \frac{\Sigma\ \ell n\ I\ (E_j)}{K} - m\ \frac{\Sigma\ E_j}{K} \tag{2-21}$$

where K is the number of data points $(\ell n\ I(E_j),\ E_j)$ used in the calculation. A comparison of Eq. (2-19) with the logarithmic form of Eq. (2-18),

TABLE 2-1. The calculated x-ray energy spectrum for a homogeneous hydrogen plasma at T_e = 1000 eV

Channel Number	Average Channel Energy (E_n)	Integrated Intensity $\ell n\ I(E_n)$	$\ell n\ I(E_n)$
1	750	406,792	12.92
2	1250	246,732	12.42
3	1750	149,650	11.92
4	2250	90,768	11.42
5	2750	55,053	10.92
6	3250	33,392	10.42
7	3750	20,253	9.92
8	4250	12,284	9.42

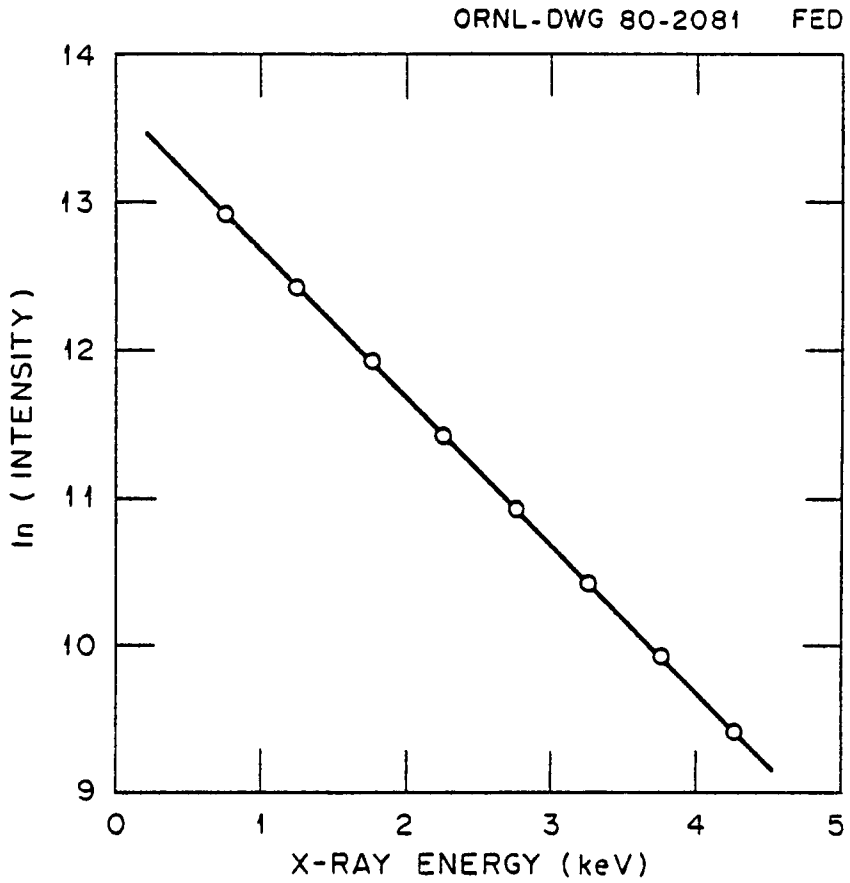

FIGURE 2-1. A plot of $\ell n\ I_j$ vs E_j for a homogeneous hydrogen plasma, with the superimposed linear least-squares fit

$$\ell n\ I(E_j) = \ell n\ I(E=0) - \frac{E_j}{T_e} \qquad (2\text{-}22)$$

where

$$I(E=0) = \pi\ \Omega\ C\ R\ \Delta t\ d_p^2\ N_e^2\ T_e^{1/2}\ \sinh\ (\Delta E/2T_e) \qquad (2\text{-}23)$$

reveals that

$$m = -\ T_e^{-1} \qquad (2\text{-}24)$$

and

$$b_o = \ell n\ I(E=0) \qquad (2\text{-}25)$$

Equations (2-24) and (2-25) provide the basis for the procedure used in analyzing the experimental data collected by the energy spectrometer. The total counts N_j in each channel of an experimental spectrum are converted to a corresponding intensity $I(E_j)$ by multiplying by the average energy of the channel.

$$I(E_j) = N_j\ E_j \qquad (2\text{-}26)$$

A straight line is fitted to the resulting data array, using the

least-squares method. The slope m is calculated from Eq. (2-20), and the plasma electron temperature is defined by Eq. (2-24). The intercept b_o is identified with I(E=0) given in Eq. (2-23); this quantity depends on spectrometer geometry and plasma parameters, and is important in plasma impurity calculations, as will be shown.

2.4.2 The Spectrum From a Nonuniform Hydrogen Plasma

In the last section, the x-ray intensity at the detector was calculated under the assumption that the hydrogen plasma was uniform in density and temperature. However, experimental plasmas exhibit nonuniform temperature and density, varying from a relatively cold, tenuous edge to a hot, dense center. This behavior as a function of position can be described by a profile. Assuming the plasma is cylindrically symmetrical along the minor radius, a, possible models for tokamak profiles have the form

$$S_e(r) = S_e(\max) \left[1 - (r/a)^m \right]^n \qquad (2\text{-}27)$$

where S_e stands for electron density or temperature, and m and n vary the profile shape. Some possible shapes are illustrated in Fig. 2-2. The three profiles used here are the triangular (m=1, n=1), the parabolic (m=2, n=1), and the squared-parabolic (m=2, n=2).

Since both density and temperature vary with radial position r, the intensity integral over the plasma volume [cf. Eq. (2-17)] becomes

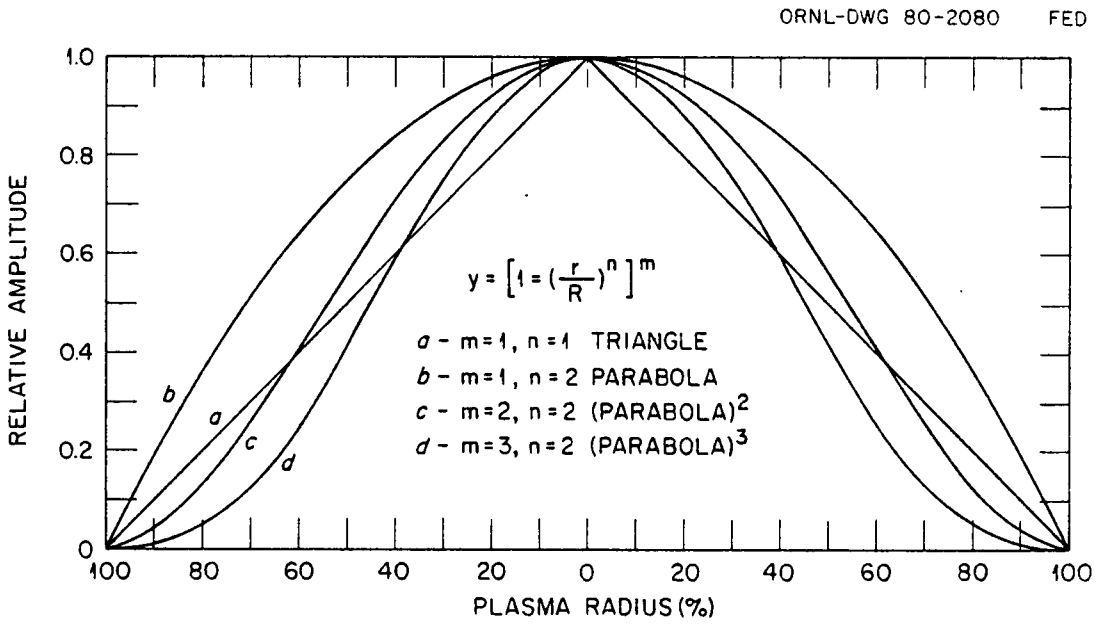

FIGURE 2-2. Profile shapes used to model T_e and N_e variations along the minor radius of a tokamak plasma

$$I(E_j) = \pi\ \Omega\ (d_p/2)^2 \int_{-a}^{a} I_V(E_j,r)\ dr \qquad (2\text{-}28)$$

where $I_V(E,r)$ contains $N_e(r)$ and $T_e(r)$. This complicating factor in the intensity calculation affects both the derived temperature and zero-energy intensity. For example, assume triangular profiles for both density and temperature:

$$N_e(r) = N_e(\max)(1 - r/a) \qquad (2\text{-}29)$$

$$T_e(r) = T_e(\max)(1 - r/a) \qquad (2\text{-}30)$$

For $T_e(\max) = 1000$ eV, $N_e(\max) = 5 \times 10^{13}$ per cm^3, and for the same numerical values used in calculating Table 2-1, the energy spectrum including profile effects is given in Table 2-2.

The data points ($\ell n\ I(E_j)$, E_j) listed in Table 2-2 are plotted in Fig. 2-3. The superimposed straight line is the least-squares fit to these points. The slight nonlinearity in the data set would not be detectable in an experimental spectrum, due to normal statistical fluctuations. The temperature derived from the spectral slope is 842 eV, 19% lower than the central temperature. If the experimental plasma profiles are known, the central temperature may be found from the chord-integral temperature by applying a correction factor. Figure 2-4 gives the correction factor for central temperature,

TABLE 2-2. The calculated x-ray energy spectrum for a hydrogen plasma with triangular T_e and N_e profiles, for $T_e(max)$ = 1000 eV

Channel Number	Average Channel Energy E in eV	Integrated Intensity I(E)	ℓn I(E)
1	750	125,342	11.74
2	1250	65,645	11.09
3	1750	35,312	10.47
4	2250	19,337	9.87
5	2750	10,728	9.28
6	3250	6,011	8.70
7	3750	3,396	8.13
8	4250	1,930	7.57

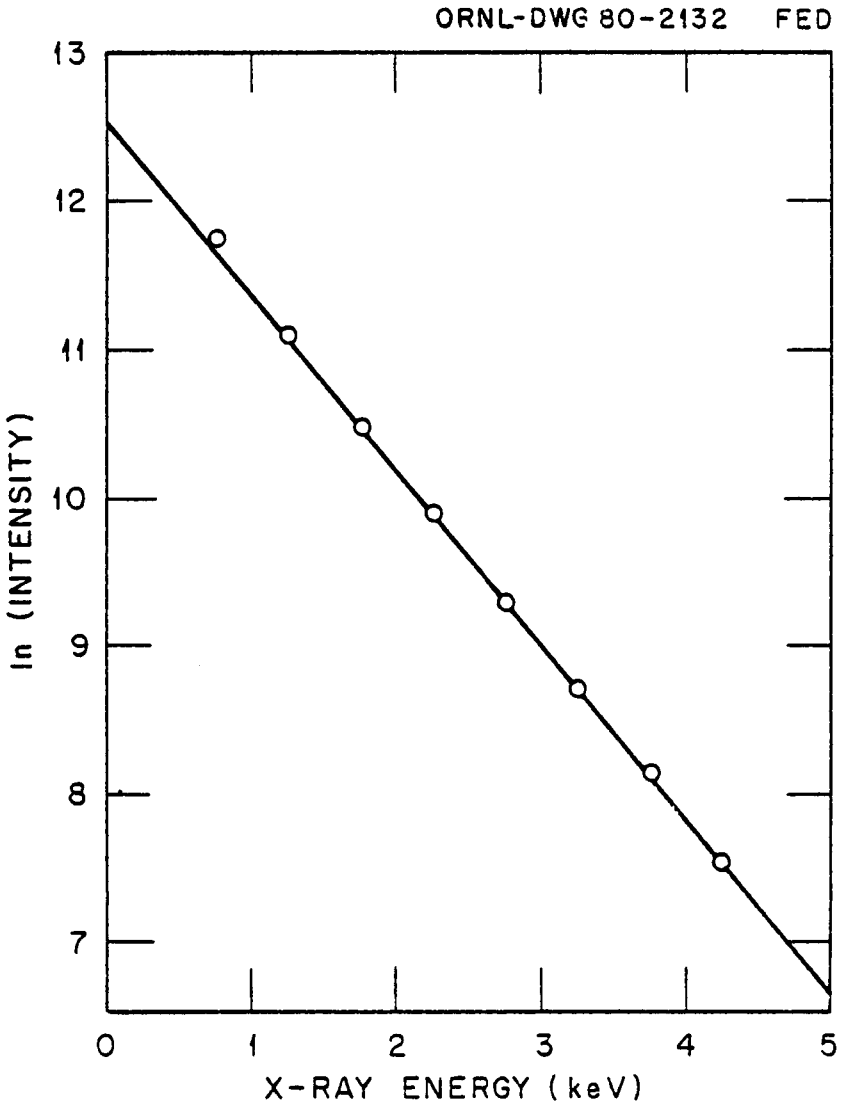

FIGURE 2-3. A plot of $\ell n\ I_j$ vs E_j for a hydrogen plasma with triangular N_e and T_e profiles, with the superimposed linear least-squares fit

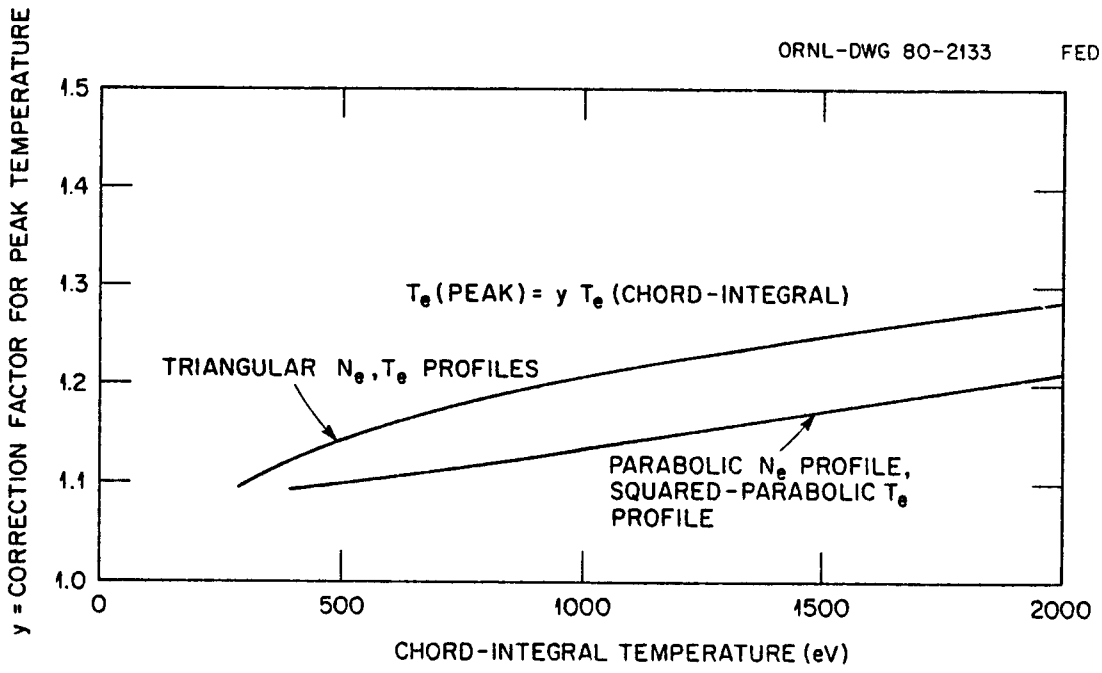

FIGURE 2-4. The correction factor y for finding central T_e from the chord-integrated value, for a hydrogen plasma with various T_e and N_e profiles

plotted as a function of the chord-integral value, for two possible sets of profiles.

2.4.3 The Spectrum from a Nonuniform Plasma Containing Impurities

Experimental plasmas always contain ion species besides hydrogen, and radiation from these impurities modifies the observed x-ray spectrum. Depending on the atomic number of the impurity species and the local plasma temperature, the dominant radiation mechanism may be free-free interactions, producing bremsstrahlung with a differential intensity given by a generalization of Eq. (2-12):

$$dI_{ff})\ (E) = C\ N_e\ T_e^{-1/2}\ (\Sigma\ N_i\ Z_i^2\ \bar{g}_{ff})\ e^{-E/T_e}\ dE \qquad (2\text{-}31)$$

or free-bound interactions, producing recombination radiation with a differential intensity[42]

$$dI_{fb}(E) = C\ N_e\ T_e^{-1/2}\ (\Sigma\ N_i\ Z_i^2\ \bar{g}_{fbi})\ e^{-E/T_e}\ dE \times$$

$$\left\{\sum_i \frac{\xi}{n^3}\frac{\chi_i}{T_e}\ e^{-\chi_i/T_e} + \sum_\nu \frac{2\chi_n}{T_e}\ \frac{Z_i^2}{(n+\nu)^3}\ \exp\ \frac{Z_i^2\ \chi_i}{(n+\nu)^2\ T_e}\right\} \qquad (2\text{-}32)$$

or bound-bound interactions, producing line radiation with a differential intensity[43]

$$dI_{bb}(E) = N_e N_i S(T_e, E) dE \qquad (2\text{-}33)$$

In the expression for I_{bb}, $S(T_e, E)$ is an ionization cross section averaged over the Maxwellian electron velocity distribution of the plasma.

Notice that the free-bound intensity I_{fb} has the same exponential dependence $\exp(-E/T_e)$ as the bremsstrahlung formula, but the recombination intensity is higher than the bremsstrahlung because of the summation terms accounting for the partially ionized states of the impurity ions. Thus, the bremsstrahlung and recombination spectra have the same shape, but the intensity of the recombination radiation is enhanced by the multiplicity of possible recombination states. The magnitude of this enhancement depends on the plasma temperature, the total ionization potential χ_i of an impurity species, and the ionization potential χ_n of each of its n electrons. As a general rule, recombination radiation is more intense for greater ionic charge Z_i, and exceeds the bremsstrahlung until $T_e > 3\,\chi_i$.[44]

Since the recombination intensity is potentially the dominant part of the total x-ray emission from a plasma, it is important to consider the possible impurity species and their respective spectral contributions. However, the formidable complexity of Eq. (2-32) makes calculations for a number of species and a range of plasma

temperatures unwieldy, even on a large computer. A more manageable approach is to calculate enhancements for the impurity species which residual gas analysis and spectrometry show to be present in the plasma. The x-ray spectrometer energy range of 1-10 keV spans line radiation energies of metals such as titanium, stainless steel components, copper, and the heavier metals such as tungsten and gold. Since metallic lines are not found in typical x-ray spectra, these elements are excluded in impurity calculations. The line radiation of such contaminants as carbon, nitrogen, and oxygen falls below the 1 keV low-energy cutoff of the x-ray spectrometer, and so these elements only enhance the continuous spectrum. There is evidence from residual gas analysis and optical spectrometry that oxygen is usually the dominant plasma impurity, so this element is taken as the typical impurity species; the enhancement calculations which follow assume that the plasma is a hydrogen-oxygen mixture.

Consider the component of the x-ray spectrum that is due to oxygen. Since line radiation for oxygen falls below the 1 keV spectral cutoff, the differential intensity is a sum of Eqs. (2-31) and (2-32). When these equations are integrated over the resolution ΔE of the spectrometer [cf. Eq. (2-14)] they take the form

$$\Delta I_{ff} = N_i Z_i^2 F(E, T_e) \qquad (2\text{-}34)$$

and

$$\Delta I_{fb} = N_i Z_i^2 \text{ (sum of recombination terms) } F(E, T_e) \qquad (2\text{-}35)$$

where

$$F(E, T_e) = 2 C N_e T_e^{1/2} \sinh (\Delta E/2T_e) e^{-E/T_e} \qquad (2\text{-}36)$$

and $\bar{g}_{ff} = \bar{g}_{fb} = 1$. The sum of Eqs. (2-34) and (2-35) becomes

$$\Delta I_{Ox} = N_i Z_i^2 \gamma(Z_i, T_e) F(E, T_e) \qquad (2\text{-}37)$$

for

$$\gamma(Z_i, T_e) = 1 + \text{(sum of recombination terms)}. \qquad (2\text{-}38)$$

Equations (2-37) and (2-34) differ by the factor $\gamma(Z_i, T_e)$. If a functional representation for γ is available, the total continuous radiation from oxygen can be treated like bremsstrahlung.

The oxygen enhancement vs T_e for three ionization states has been published in graphical form by researchers at Princeton.[45] Figure 2-5 duplicates the graphical information. Empirical formulas for the curves are:

$$Z_i = 8, \ln \gamma = 1.66 e^{-0.86 \ln T_e} \qquad (2\text{-}39)$$

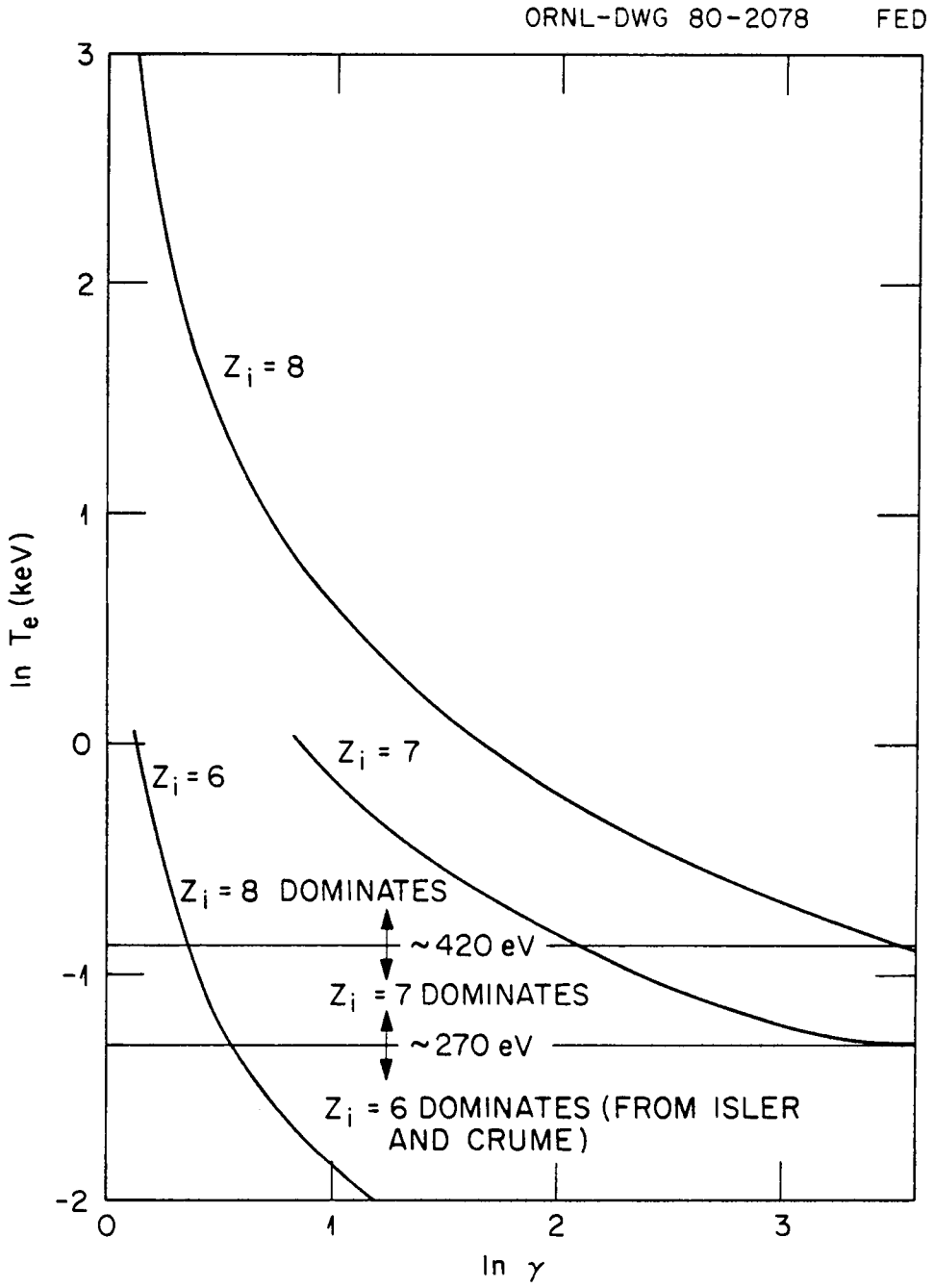

FIGURE 2-5. Radiation enhancement factors (relative to bremsstrahlung) vs T_e for the three highest ionization states of oxygen

$$Z_i = 7,\ \ln \gamma = 0.85\ e^{-1.03\ \ln T_e} \tag{2-40}$$

$$Z_i = 6,\ \ln \gamma = 0.14\ e^{-1.06\ \ln T_e} \tag{2-41}$$

Data from an Oak Ridge study[46] provide information on the plasma temperature range in which each of the three oxygen ionization states is dominant. Figure 2-6 gives radial profiles of plasma parameters (top) and concentration of oxygen ions (bottom). From this figure, $Z_i = 8$ dominates above $T_e \sim 420$ eV; $Z_i = 6$, below 270 eV; and $Z_i = 7$, between these two temperatures.

The x-ray spectrum from a hydrogen-oxygen plasma can be calculated by using Eq. (2-37) and the proper expression for γ in conjunction with the hydrogen bremsstrahlung formula,

$$\Delta I_H = N_e\ F(E,\ T_e) \tag{2-42}$$

(Plasma charge neutrality for hydrogen requires $N_i = N_e$.) The total radiation intensity from unit volume of mixed plasma is

$$\Delta I = 2C\ N_e^2\ T_e^{1/2} \sinh (\Delta E/2T_e)(1 + b\ \gamma\ Z_i^2)\ e^{-E/T_e} \tag{2-43}$$

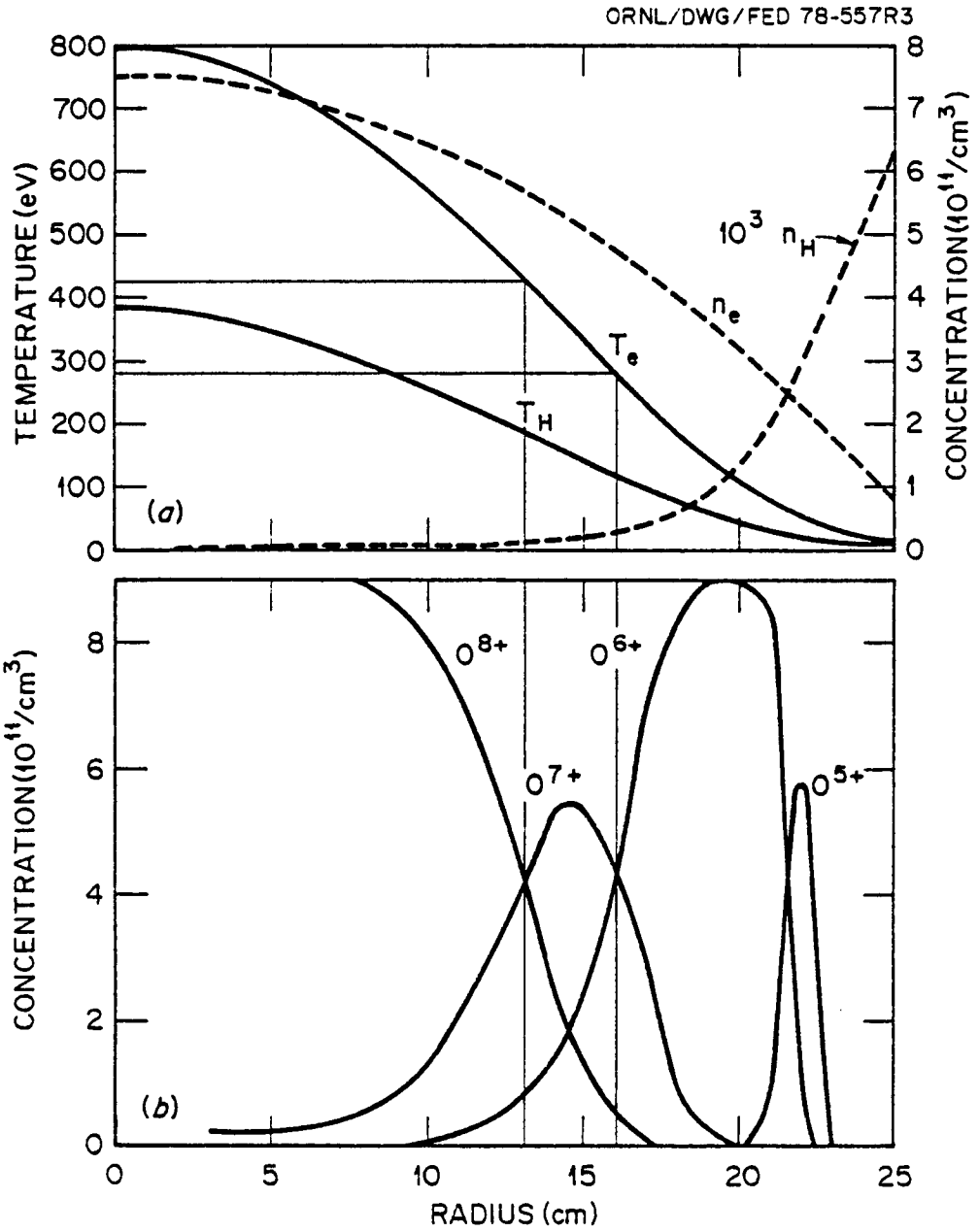

FIGURE 2-6. The distribution of oxygen ionization states as a function of plasma radius and temperature

where b is the (small) fraction giving the ratio of oxygen to hydrogen in the plasma,

$$b = N_i \text{ (oxygen)}/N_i\text{(hydrogen)} \ . \qquad (2\text{-}44)$$

The integrated intensity recorded in a spectrum is found by multiplying Eq. (2-43) by the time interval Δt, the solid angle Ω, and integrating over the plasma volume defined by the system geometry. Suitable radial profiles for N_e and T_e must be used in the integral. For channel j of the spectrum,

$$I(E_j) = \pi\ C\ \Omega\ d_p^2 \int_o^a N_e^2(r)\ T_e^{1/2}(r)\ \sinh\left[\Delta E/2T_e(r)\right] \times \left\{1 + b\ \gamma(Z_i,\ T_e)\right\}\ e^{-E_j/T_e(r)}\ dr \qquad (2\text{-}45)$$

For the same numerical parameters used in calculating Table 2-2, using triangular profiles for N_e and T_e, and for b = 0.04, an energy spectrum calculated by Eq. (2-45) is given in Table 2-3. This spectrum is plotted in Fig. 2-7, along with a superimposed least-squares linear fit. The temperature derived from the spectral slope is 792 eV, 26% lower than the central value. For the 4% oxygen case, $\ell n\ I(E=0) = 15.73$, compared with 12.57 for the pure hydrogen plasma; the difference in intensities represents an enhancement of 23.5 due to the oxygen impurity!

TABLE 2-3. The calculated x-ray energy spectrum for a plasma with 4% oxygen impurity, triangular T_e and N_e profiles, and $T_e(max)$ = 1000 eV

Channel Number	Average Channel Energy E in eV	Integrated Intensity I(E)	ℓn I(E)
1	750	2,850,167	14.86
2	1250	1,399,357	14.15
3	1750	713,533	13.48
4	2250	374,140	12.83
5	2750	200,399	12.21
6	3250	109,132	11.60
7	3750	60,214	11.01
8	4250	33,576	10.42

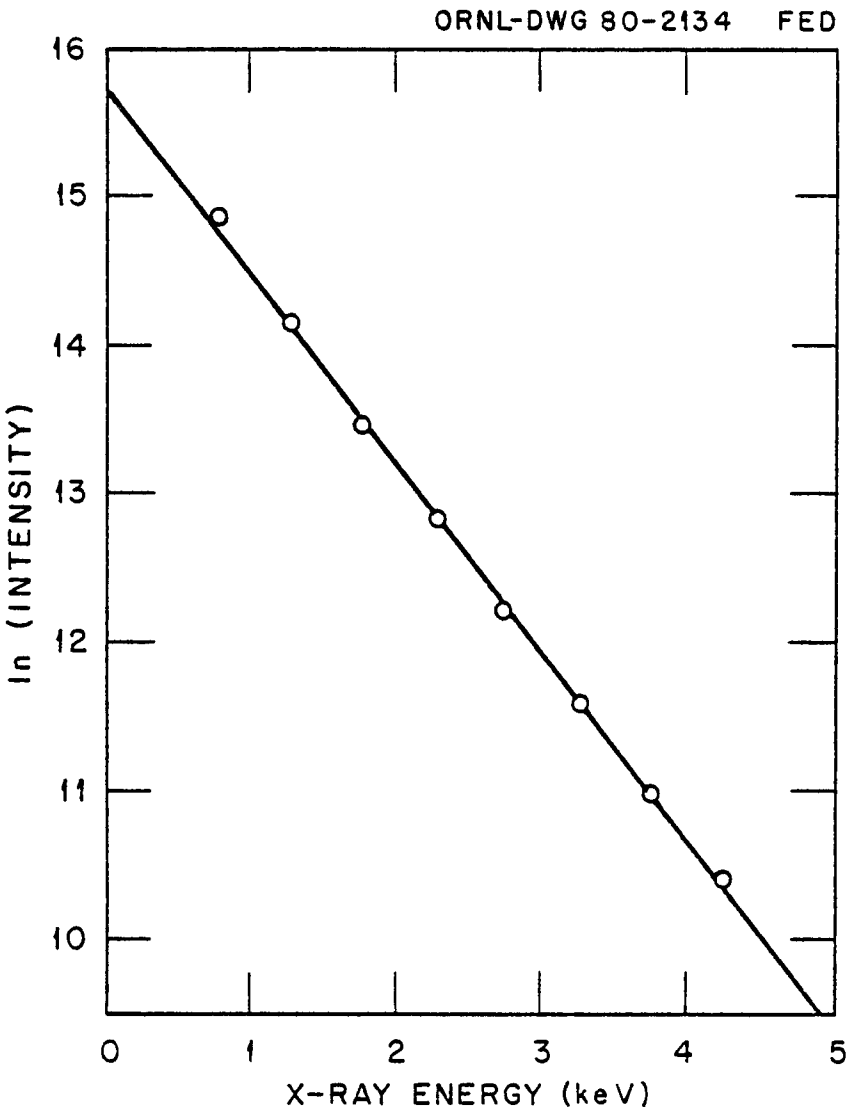

FIGURE 2-7. A plot of $\ell n\ I_j$ vs E_j for a plasma with 4% oxygen impurity and triangular T_e and N_e profiles, with the superimposed linear least-squares fit

An examination of Eq. (2-45) reveals that the enhancement concept may be taken one step further; the total intensity formula has the same form as the hydrogen bremsstrahlung multiplied by a single enhancement factor η,

$$I(\text{total}) = \eta(T_e, \%0)\ I(\text{hydrogen}) \ . \qquad (2\text{-}46)$$

A program developed at ORNL by E. C. Crume and others[47] begins with Eqs. (2-31) and (2-32) and solves for total x-ray intensity from first principles. The usual plasma parameters N_e, T_e, $b = \{ N(\text{oxygen})/N(\text{hydrogen}) \}$ are required, along with profiles and plasma-detector geometry. In addition, the code (called RECNO) uses published tables of oxygen ionization potentials and recombination cross sections in combination with an impurity transport model to predict the impurity contribution to the x-ray continuum. RECNO also calculates Z_{eff}, the effective ionic charge of the plasma

$$Z_{eff} = \frac{\Sigma\ N_i\ Z_i^2}{\Sigma\ N_i\ Z_i} \qquad (2\text{-}47)$$

at different plasma radii.

If RECNO is used to calculate a series of energy spectra [cf. Table 2-3] for different temperatures and different impurity concentrations, a table may be constructed which gives total

enhancement of η as a function of T_e and Z_{eff} for given plasma profiles. Figure 2-8 illustrates the behavior of η with increasing Z_{eff}, for a fixed T_e(central) of 1000 eV, using triangular N_e and T_e profiles. (The plasma with $Z_{eff} = 1.005$ is taken as essentially pure hydrogen.) Tables 2-4 and 2-5 summarize RECNO calculations for two sets of plasma profiles. Triangular profiles emphasize variations in those parameters which are profile sensitive, since the triangular distribution is sharply peaked and provides a relatively large change in temperature and density in the central region of the plasma. Parabolic N_e and squared-parabolic T_e profiles more nearly represent typical experimental profiles for tokamaks.

Using electron temperatures derived from least-squares fits to RECNO spectra, correction factors y to find central temperatures as a function of Z_{eff} and plasma profiles can be generated. Figure 2-9 shows the range of y as a function of T_e from least-squares fits over the range of Z_{eff}. For the models given, the mean value of y can be found from the empirical formula

$$y(\text{mean}) = 1.3 \times 10^{-4}\, T_e\ (\text{chord-integral, eV}) + 1.06 \qquad (2\text{-}48)$$

In Fig. 2-10, Z_{eff} vs $\ell n\ \eta$ is plotted for the three values of T_e(central) and for the two profile sets given in Tables 2-4 and 2-5. Note that triangular and parabolic/squared-parabolic profiles give results that are essentially identical. This implies that the accuracy of Z_{eff} determinations by x-ray spectrometry is not greatly

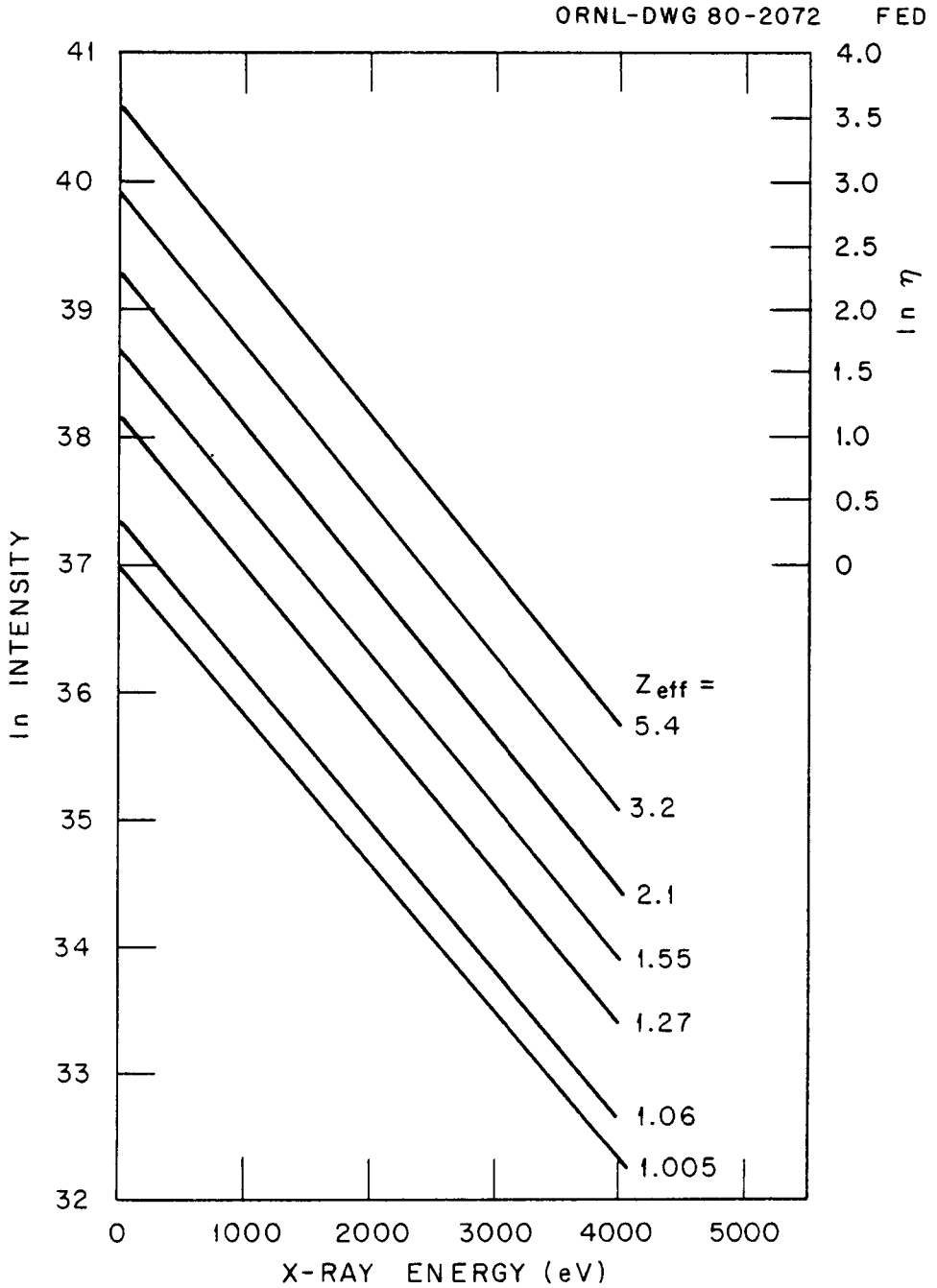

FIGURE 2-8. A plot of ℓn I vs E for various concentrations of oxygen in a plasma with triangular N_e and T_e profiles and $T_e(max)$ = 1000 eV

TABLE 2-4. Results of RECNO calculations for triangular N_e, T_e, and impurity distribution profiles

T_e(Central)	b × 100	Z_{eff}	T_e(ℓsf)	Y	ℓnI (E=0)	ℓn η
500 eV	0.01	1.004	436	1.146	37.90	0.0
	0.1	1.041	436	1.147	38.41	0.51
	0.5	1.204	436	1.147	39.42	1.52
	1.0	1.408	435	1.148	40.00	2.10
	2.0	1.816	435	1.148	40.64	2.74
	4.0	2.632	435	1.148	41.30	3.40
	8.0	4.264	435	1.148	41.98	4.08
1000 eV	0.01	1.005	851	1.175	37.58	0.0
	0.1	1.055	842	1.187	37.93	0.35
	0.5	1.273	830	1.205	38.76	1.18
	1.0	1.547	826	1.211	39.29	1.71
	2.0	2.096	823	1.215	39.89	2.31
	4.0	3.190	821	1.218	40.54	2.96
	8.0	5.385	820	1.219	41.21	3.63
2000 eV	0.01	1.006	1596	1.253	37.36	0.0
	0.1	1.056	1578	1.267	37.54	0.18
	0.5	1.280	1542	1.297	38.08	0.72
	1.0	1.560	1522	1.314	38.50	1.14
	2.0	2.121	1508	1.326	39.02	1.66
	4.0	3.238	1497	1.336	39.62	2.26
	8.0	5.485	1491	1.341	40.26	2.90

TABLE 2-5. Results of RECNO calculations for parabolic N_e and impurity distribution profiles, and a squared-parabolic T_e profile

T_e(Central)	b × 100	Z_{eff}	T_e(ℓsf)	Y	ℓnI (E=0)	ℓn η
500 eV	0.01	1.004	457	1.094	38.33	0.0
	0.1	1.044	457	1.093	38.84	0.51
	0.5	1.219	458	1.091	39.86	1.53
	1.0	1.437	458	1.091	40.44	2.11
	2.0	1.875	458	1.091	41.08	2.75
	4.0	2.750	459	1.090	41.74	3.41
	8.0	4.500	459	1.090	42.42	4.09
1000 eV	0.01	1.005	894	1.118	37.99	0.0
	0.1	1.055	886	1.128	38.31	0.32
	0.5	1.275	874	1.144	39.10	1.11
	1.0	1.549	870	1.149	39.61	1.62
	2.0	2.099	867	1.153	40.21	2.22
	4.0	3.198	866	1.155	40.85	2.86
	8.0	5.394	865	1.156	41.51	3.52
2000 eV	0.01	1.006	1676	1.193	37.76	0.0
	0.1	1.056	1657	1.207	37.93	0.17
	0.5	1.280	1612	1.241	38.46	0.70
	1.0	1.560	1594	1.255	38.86	1.10
	2.0	2.117	1576	1.269	39.37	1.61
	4.0	3.235	1563	1.280	39.98	2.22
	8.0	5.470	1556	1.285	40.61	2.85

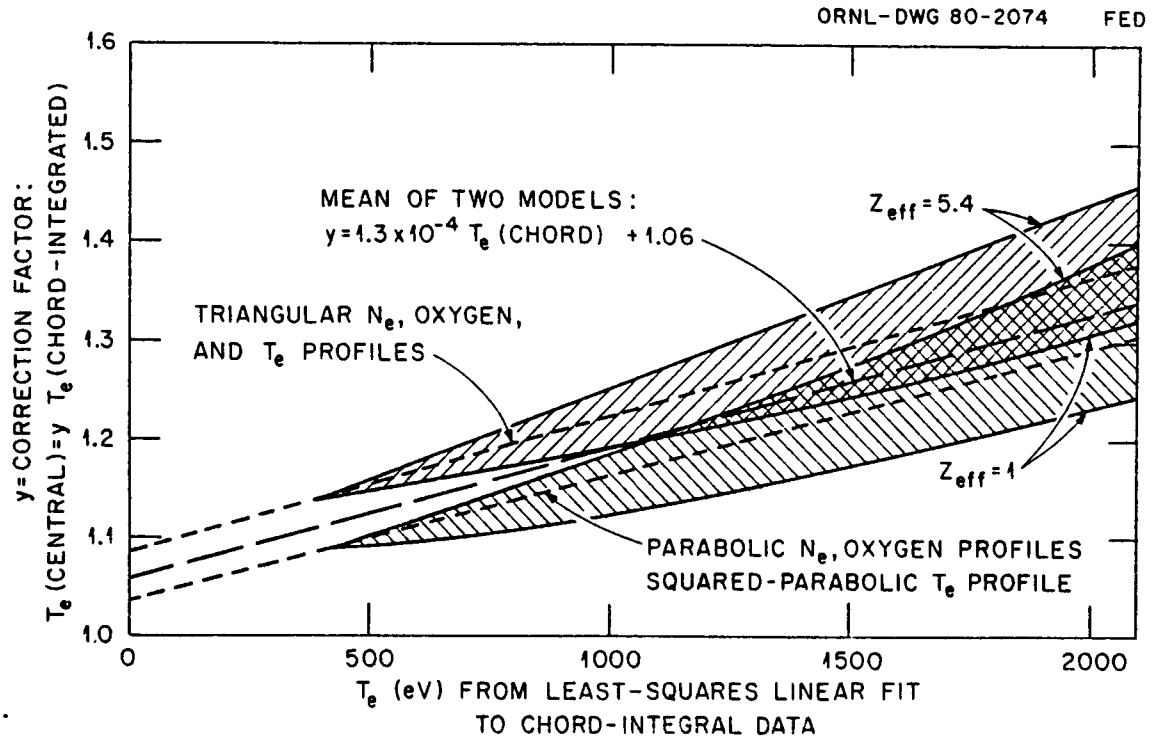

FIGURE 2-9. The correction factor y for finding central T_e from the chord-integrated value, showing the effects of profiles and Z_{eff}

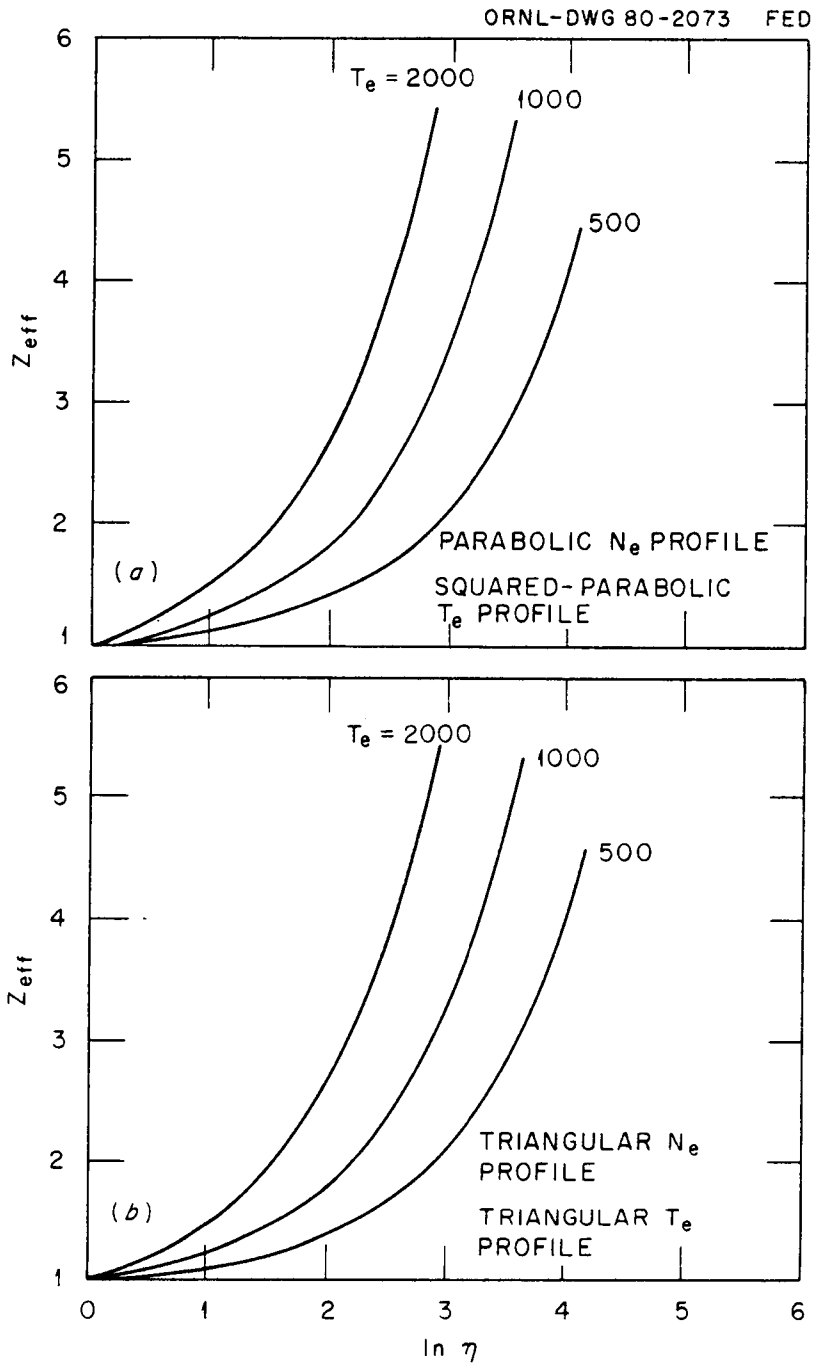

FIGURE 2-10. Plots of Z_{eff} vs $\ell n\ \eta$ for oxygen in a hydrogen plasma, for parabolic N_e and N_{ox} profiles and a squared-parabolic T_e profile (top), and triangular N_e, N_{ox}, and T_e profiles (bottom)

affected by the specific plasma model used. An empirical formula that relates Z_{eff} to T_e(central) and η is

$$Z_{eff} = 1 + \alpha(\ell n\ \eta)^{\beta} \tag{2-49}$$

where

$$\alpha = (2.63 \times 10^{-7})\ T_e^{1.94} \tag{2-50}$$

and

$$\beta = 3.75\ e^{-3.4 \times 10^{-4}\ T_e} \tag{2-51}$$

and where T_e(central) is in eV and η is the enhancement in I(E=0) for an impure plasma, compared to a pure hydrogen plasma with the same profiles, density, temperature, and geometry.

Knowledge of the functional dependence of Z_{eff} vs η makes possible an estimation of Z_{eff} for an experimental plasma. The experimental x-ray energy spectrum provides a chord-integrated temperature and a zero-energy intensity. The chord-integrated temperature is corrected by the factor y given in Eq. (2-48) to the central T_e value. Electron density data (from another diagnostic, such as the microwave interferometer), T_e(central), suitable profiles, and plasma-detector geometry are used in Eq. (2-28) to calculate the

intensity expected from pure hydrogen. The enhancement of the experimental plasma over pure hydrogen is found as

$$\ell n\ \eta = \ell n\ i(E=0)_{Experimental} - \ell n\ I(E=0)_{Hydrogen} \qquad (2\text{-}52)$$

and this value of η along with the T_e(central) derived from the spectrum is used in Eq. (2-49) to solve for Z_{eff}.

CHAPTER 3

ERROR SOURCES AND ERROR ANALYSIS

3.1 INTRODUCTION

The accuracy of T_e and Z_{eff} measurements by x-ray energy spectrometry can be influenced by a variety of factors. Some potential errors can be avoided by careful system design. However, several factors intrinsic to the analysis method must be investigated to ensure that they do not affect results to an unacceptable extent. Table 3-1 lists possible error sources by category.

3.2 ELECTRONIC ERRORS

The electronic system of the energy analyzer provides examples of both avoidable and intrinsic error sources. Careful design and component selection minimize several potentially harmful effects, but energy channel width and pulse pileup produce unavoidable spectral distortion.

3.2.1 Gain and Count-Rate Errors

Gain linearity and stability are two system parameters that directly affect x-ray energy measurements, but variations in these can be controlled. Careful tests of the pulse amplifying system verify that errors from these sources are negligible. Gain is initially calibrated and periodically checked by using the 5.9 keV x-ray line spectrum from iron-55. Tests with a calibrated pulser confirm pulse-height analyzer linearity. Amplifier gain is calibrated to 2% accuracy.

TABLE 3-1. Possible sources of error in x-ray measurements of plasma parameters

I. Electronic errors
Gain calibration
Gain nonlinearity
Gain stability
Baseline shift with count rate
Amplifier noise
Pulse-height analyzer deadtime
Finite PHA channel width
Pulse pileup at high count rates
II. Detector errors
Detector transparency
Detector absorption
Incomplete charge collection
Energy resolution
III. Detector-plasma geometry
Fluorescence and x-ray scatter at detector
Wall radiation
Profile effects
IV. Plasma effects
Attenuation along plasma path
Non-Maxwellian plasma
Short-period (MHD) fluctuations
Line radiation
Quantum-mechanical effects
Impurity effects
V. Modelling and statistical errors

Rate-dependent errors such as baseline shift and oscillatory instabilities are important at the data rates necessary in ths diagnostic, so the absence of these has been verified during initial system tests. Periodic oscilloscope checks confirm that baseline shift, oscillations, and ground-loop noise are absent during experimental runs.

3.2.2 Finite Pulse-Height Channel Width

An intrinsic electronic parameter which does affect analyzed data is pulse-height analyzer channel width. The relatively small number of channels (20) implies that a single channel spans at least 5% of the measured spectrum, and usually more, since typical spectra occupy 6 to 12 channels. A small number of channels is expedient for two reasons: the parallel analysis technique is cumbersome for a large number of channels, and the small number of counts per spectrum makes a large number of channels statistically unprofitable.

The exponential shape of the x-ray energy spectrum dictates that more counts fall into the lower half of a given channel than into the upper half, so the count contribution is skewed toward lower energies. This introduces some spectral distortion when each channel is assigned an average energy, and all events recorded in channel j are assigned an energy E_j. To find the effect of this distortion on derived T_e, consider the distribution function

$$d\,N(E) = \frac{A}{E}\, e^{-E/T_e}\, dE \qquad (3\text{-}1)$$

which gives the number of counts expected in the energy interval (E, E + dE). (A discussion of this distribution function and its derivation is found in Appendix B.) Equation (3-1) can be integrated over the energy interval $(E_n - \Delta E/2, E_n + \Delta E/2)$ to find the counts in channel n.

$$N_n = \int_{E_n - \Delta E/2}^{E_n + \Delta E/2} (A/E)\, e^{-E/T_e}\, de \qquad (3\text{-}2)$$

Equation (3-2) may be evaluated by expanding the integrand as a Taylor's series about E_n and keeping the first two terms of the expansion.

$$N_n = \frac{A\,\Delta E}{E_n} e^{-E_n/T_e} \left[1 + \frac{(\Delta E)^2}{24} \left\{ \frac{2}{E_n^2} + \frac{2}{E_n\, T_e} + \frac{1}{T_e^2} \right\} \right] \qquad (3\text{-}3)$$

Since intensity $I(E) = N \cdot E$, and since $\ell n(1 + \beta) \simeq \beta$, an expression for the integrated intensity represented by channel n can be found from Eq. (3-3).

$$\ell n\, I_n = \ell n(A\,\Delta E) - E_n/T_e + \frac{(\Delta E)^2}{24} \left\{ \frac{2}{E_n^2} + \frac{2}{E_n T_e} + \frac{1}{T_e^2} \right\} \qquad (3\text{-}4)$$

The derivative of Eq. (3-4) with respect to E_n yields

$$\frac{d\ \ell n\ I_n}{d\ E_n} = -\frac{1}{T_e} - \frac{(\Delta E)^2}{24}\left\{\frac{2}{E_n^3} + \frac{1}{E_n^2 T_e}\right\} \tag{3-5}$$

Equation (3-5) gives the slope of the $\ell n\ I$ vs E spectrum in the vicinity of E_n. If the spectrum were linear, the slope would be $-(1/T_e)$; the presence of the term in $(\Delta E)^2$ is a measure of the spectral distortion due to finite channel width. To find the error in a temperature derivation due to this spectral distortion, define a variable Q which includes the effects of finite channel width

$$Q = \frac{d\ \ell n\ I_n}{dE_n} \tag{3-6}$$

and let the true plasma temperature be

$$T_e = -1/Q + \delta T_e \tag{3-7}$$

Then $\delta T_e/T_e$ is a measure of the error introduced by finite channel width. Substitution of Eqs. (3-5) and (3-6) into (3-7) produces

$$\frac{\delta T_e}{T_e} \simeq \frac{1}{12}\frac{(\Delta E)^2}{(E_n)^2}\left\{\frac{2T_e}{E_n} + 1\right\} \tag{3-8}$$

Equation (3-8) shows that the effect of finite channel width on T_e derived from an experimental spectrum is greatest when E_n is small. From Eq. (3-5), the absolute value of $d \ell n I_n$ vs $d E_n$ is larger than $1/T_e$ by the error factor, so T_e determined from the distorted spectrum is smaller than the true value by δT_e. Plots of $\delta T_e/T_e$ vs E for three values of T_e are given in Fig. 3-1. Only the first four spectrometer channels are affected by more than 1%, so when a least-squares fit is applied to the total spectrum, finite channel width introduces negligible error in temperature calculations.

3.2.3 Pulse Pileup

A second intrinsic parameter of the spectrometer electronics which affects the collected spectrum is pulse width. A minimum pulse width of 1-2 μs is required for adequate energy resolution, so even with tail pileup rejection, a significant fraction of amplifier pulses pile up at 10^5 counts per second. The severity of the spectral distortion caused by this pileup is a function of pulse shape as well as pulse width and counting rate. A detailed analysis of the pileup problem has been published,[48] and is included as Appendix B. Results of this analysis for a triangular approximation to the linear amplifier pulse shape, a nominal electron temperature of 1000 eV, and pileup fraction K ranging up to 0.5 are given in Fig. 3-2. The pileup fraction,

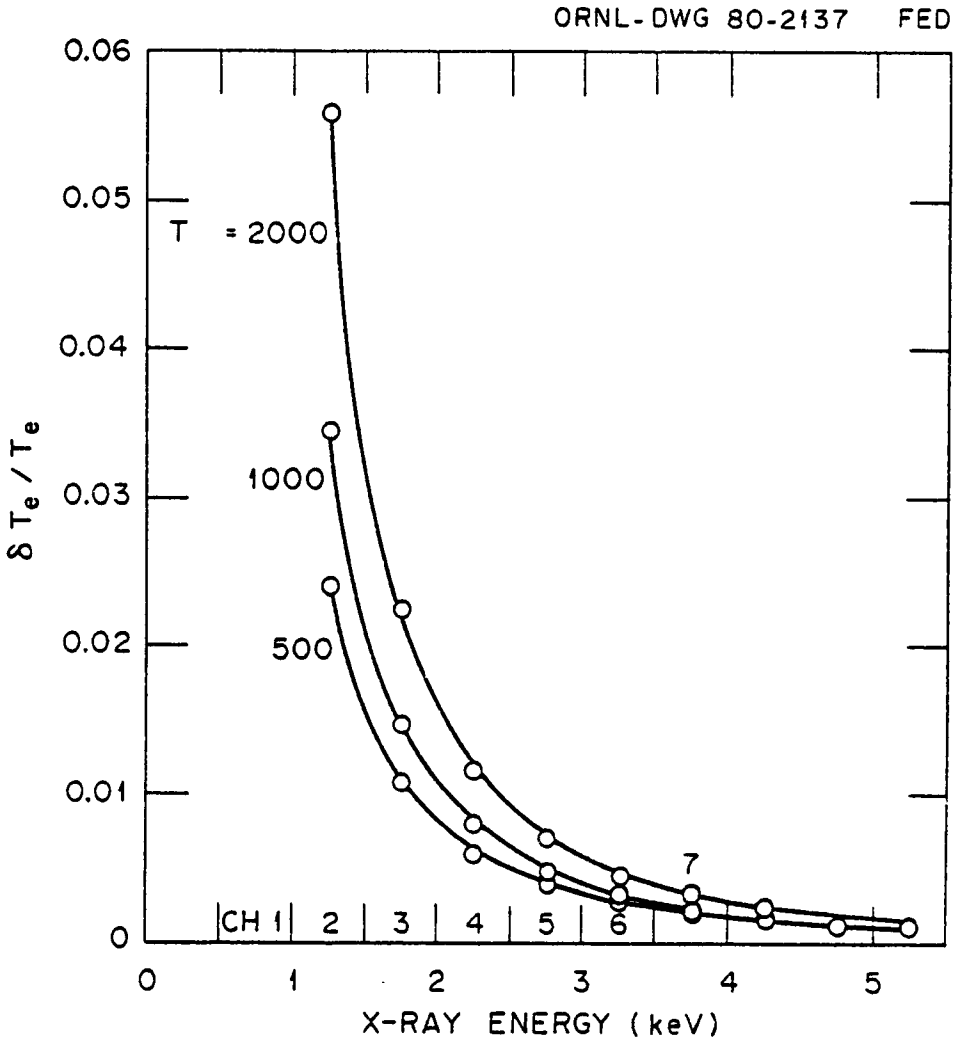

FIGURE 3-1. The fractional error in T_e caused by the ℓn I(E) vs E nonlinearity resulting from an energy channel width of 500 eV

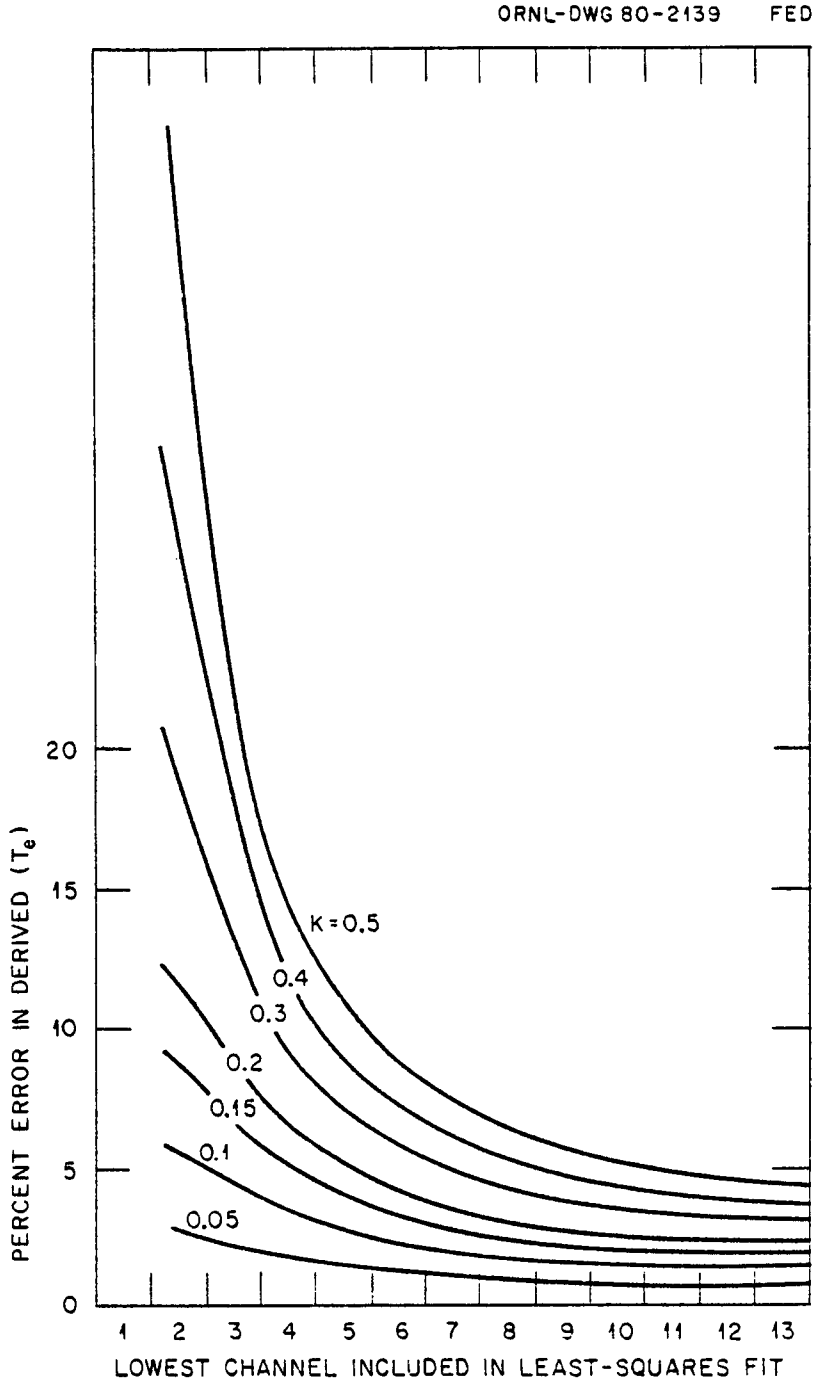

FIGURE 3-2. The percentage error in T_e derived by a least-squares fit to a pileup-distorted spectrum, as a function of lowest-channel energy

$$K = \frac{\tau}{T} \tag{3-9}$$

where τ is amplifier pulse width and T is mean time between pulse arrivals, gives the total fraction of points in an energy spectrum which are two-pulse sums. Since pileup removes single counts from lower energies in a spectrum and inserts two-pulse counts at higher energies, a temperature derived from a pileup-distorted spectrum is too large, compared to the true value. The combination of tail pileup rejection and pulse summing effects also reduces the total counts in a distorted spectrum, compared to the true number. Both these effects must be considered in calculations.

If temperature is derived from a least-squares fit to experimental spectral points, lower-energy points contribute the worst error in the calculation. The simplest expedient for reducing pileup-induced error in temperature calculations is to exclude the most erroneous data points. The fraction K of pileup pulses actually included in the experimental spectrum for a 2 μs pulse width is

$$K = \frac{10^{-6} \Sigma N_j}{10^{-2}} \tag{3-10}$$

where 10^{-6} s is the width of the leading half of the pulse (tail pileup rejection excludes tail sum pulses from the spectrum) and $10^{-2}/\Sigma N_j$ is the spectrum acquisition time divided by total counts,

giving the average time between pulses. When the value of K as calculated by Eq. (3-9) is applied to Fig. 3-2, the spectral channels which should be excluded from a least-squares fit to produce a temperature derivation with acceptable accuracy can be determined. For example, if the error in T_e due to pileup distortion is limited to 8%, and K = 0.3, then spectral channels below channel 5 must be excluded from the least-squares fit. Table 3-2 lists the lowest channels to be included in a temperature calculation for a 2 μs pulse width, if accuracy is to be 8% or better.

3.3 DETECTOR ERRORS

3.3.1 Detector Efficiency

The detector may introduce errors into an experimental measurement because of variations in efficiency over the required energy range and poor energy resolution. Detector efficiency may be affected by poor charge collection, transparency of the diode at high x-ray energies, and absorption of low-energy x-rays before they reach the active volume of the detector. In a carefully manufactured diode, the charge-collection deficit is noticeable only at the highest possible energy resolution. Checks with an iron-55 source show no conspicuous departure from a Gaussian energy resolution curve, so charge collection is satisfactory for the present detector. Detector transparency is not a factor at the spectral limit of 10 keV, since a 3-mm thickness of silicon transmits only 10^{-11} of the incident radiation at this energy. The third factor in detector efficiency, absorption at low energies, is harder to evaluate.

TABLE 3-2. Lowest allowed channel vs total counts in a spectrum, for no more than 8% error in T_e from a least-squares fit

ΣN_n in 10 ms Spectrum	Pileup Fraction K	Lowest Allowed Channel in LSF
0-1500	0-0.15	2
1500-2000	0.15-0.2	3
2000-3000	0.2-0.3	4
3000-4000	0.3-0.4	5
≥4000	≥0.4	No calculation allowed

Absorption occurs in the beryllium entrance window of the detector cryostat, in the gold electrode vacuum-deposited on the front face of the diode, and in the partially sensitive region just under the gold electrode. If the manufacturer's estimates of the thickness of each of these materials is used,[49] a calculation of x-ray transmission vs energy can be made from the equation

$$I = I_o \exp\{-\sum_i \mu_i \rho_i x_i\} \qquad (3\text{-}11)$$

where μ, ρ, and x are the mass absorption coefficient, specific gravity, and thickness of each of the three absorbing layers. If the calculated absorption for 1.25×10^{-3} cm of beryllium, 2×10^{-6} cm of gold, and 10^{-5} cm of silicon is compared with experimental data, the predicted absorption is much greater than that actually observed. Figure 3-3 shows typical experimental data points for a well-behaved plasma at 500 eV measured temperature. The superimposed straight line is a least-squares fit to all but the lowest-energy data point. The dotted curve is the predicted spectral shape due to absorption effects. Obviously, the experimental data are less affected by absorption than is predicted. Since the manufacturer's figures are upper limits on thickness, and since absorption of thin sections is difficult to calculate because of porosity, oxide layers, and other complications,[50] the evidence of Fig. 3-3 is taken to show that absorption is not a significant problem down to approximately 1 keV.

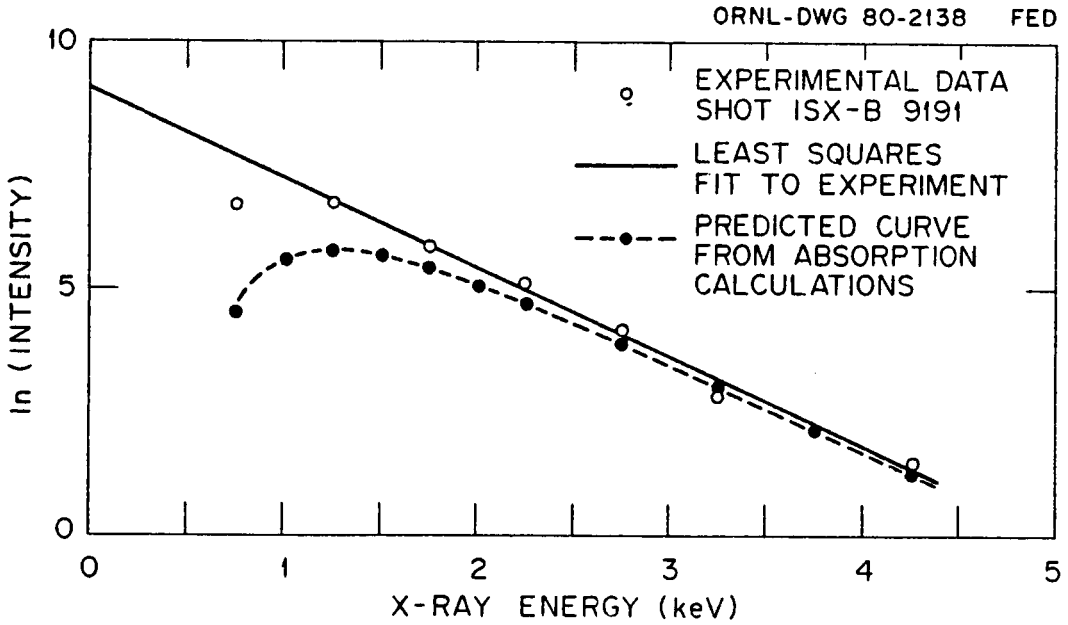

FIGURE 3-3. A comparison of experimental data with calculated absorption vs energy, for ORTEC x-ray detector

3.3.2 Energy Resolution

Although energy resolution is included in detector faults, the total spectrometer determines the resolution which can be achieved in a given application. The resolution of the present system under typical experimental conditions is ~400 eV, exclusive of the pulse-height analyzer resolution discussed previously. Finite resolution tends to disperse spectral features; its effects are apparent for line spectra, where broadening is evident, but the effects on a continuous spectrum are less obvious. The number distribtuion for counts (or photons) per energy interval given in Eq. (3-1)

$$dN(E) = \frac{A}{E} e^{-E/T_e} dE \qquad (3\text{-}12)$$

can be used in conjunction with the Gaussian energy resolution spreading function

$$F(E, E') = \frac{1}{0.6\,\Delta\,\pi^{1/2}} \exp - \left\{\frac{E - E'}{0.6\,\Delta}\right\}^2 \qquad (3\text{-}13)$$

to determine the effect of finite resolution on spectral shape. The function of Eq. (3-13) is derived from the usual Gaussian form in terms of σ by substituting the full-width-at-half-maximum Δ, commonly used in specifying detector energy resolution.[51]

$$0.6\,\Delta = \sigma\sqrt{2} \qquad (3\text{-}14)$$

The product of the original photon count distribution, Eq. (3-12), and the resolution spreading function, Eq. (3-13), is integrated over the spectral range accepted by the detector to define a new photon distribution including system energy resolution.

$$dN'(E) = \int_{E_o}^{E_{max}} \frac{A}{E} e^{-E/T_e} \times \frac{1}{0.6\,\Delta\,\pi^{1/2}} e^{-\left\{\frac{E-E'}{0.6\,\Delta}\right\}^2} dE \qquad (3\text{-}15)$$

This function is not analytic, but a numerical integration for Δ = 400 eV gives the results plotted in Fig. 3-4, for electron temperatures from 300 eV to 1200 eV. Note that for energies above 1.4 keV (= E_o + Δ) the slope of the new distribution is essentially equal to that of the original. This calculation assumes that the lower energy E_o has a sharp cutoff; actual experimental spectra fall away more gradually at the low energy limit, and so experimental spectra are not as distorted by resolution effects as Fig. 3-4 indicates. In any case, the spectral broadening caused by 400 eV resolution does not adversely affect calculations made on spectral slope, and the spectral intensity is displaced by an insignificant amount.

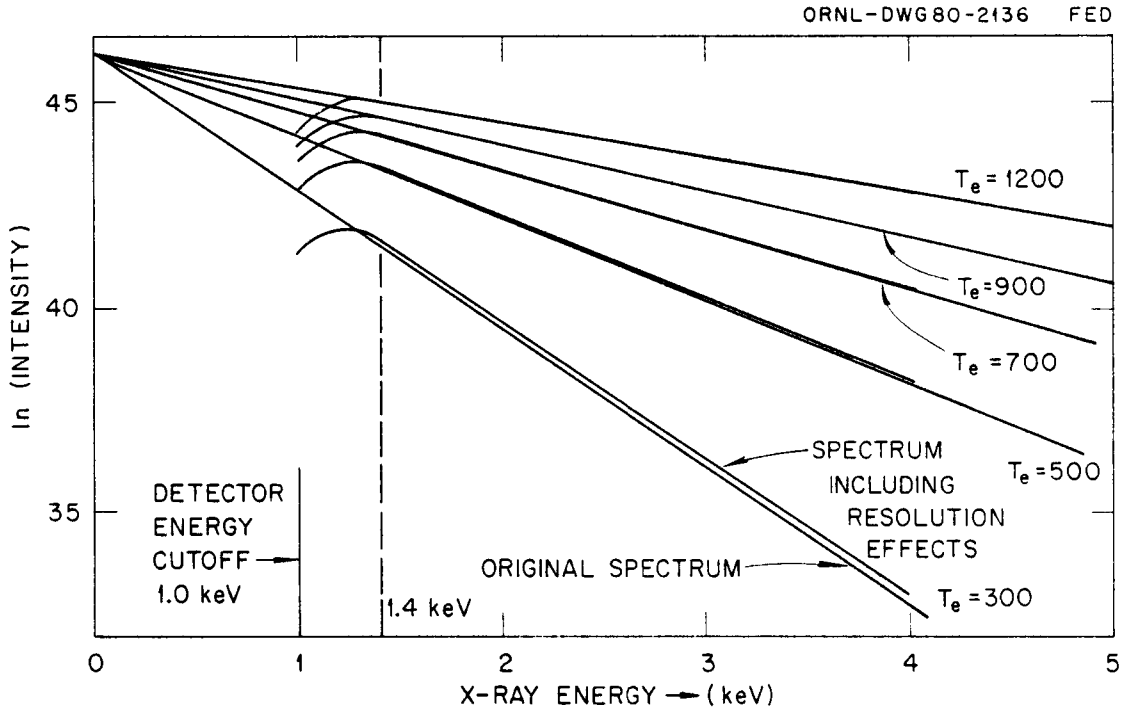

FIGURE 3-4. The calculated effect of 400 eV FWHM resolution on continuous spectra at various temperatures

3.4 DETECTOR-PLASMA GEOMETRY

3.4.1 Fluorescence and Scattered Radiation

The detector is almost 3 m from the plasma center line, so careful design is necessary to restrict the detector field of view to exclude surfaces which might fluoresce under electron bombardment, or scatter radiation into the detector. Detector geometry is discussed in Appendix A, Section A.3. Figures included there show the arrangement of apertures that block all direct radiation from the detector except for a thin cone through the plasma center. Only a small part ($\sim$1 cm^2) of the vacuum vessel wall behind the plasma is in direct view of the detector. The detector geometry has been visually checked on the tokamak (during glow discharge cleaning) with an optical window in place of the detector, to affirm that a clear path into the vacuum vessel does exist.

Fluorescent radiation typically contains the characteristic x-ray lines of the fluorescing material, so the absence of fluorescence can be inferred from the absence of line spectra in experimental plasmas. This absence is not surprising, since the tokamak is carefully designed to avoid collisions of energetic electrons with the vacuum vessel walls. Sources of radiation other than the directly viewed plasma have been eliminated by $\sim$10 cm of lead shielding at the detector. The effectiveness of the shield and the absence of radiation except from the plasma can be determined by closing the vacuum valve between detector and tokamak. This valve is opaque to soft x-rays. Spectra taken under this condition show only random (usually one or two) counts in channel 1 or channel 20.

The absence of scattered radiation is more difficult to ascertain. At soft x-ray energies, small-angle elastic scattering is the most probable process, and this would not drastically change the measured spectral shape or intensity. The design of the aperture system minimizes scattering and reflecting surfaces, so scattered radiation is not expected to be a problem.

3.4.2 Profile Effects

Profile effects occur because energy spectra from both the cold plasma edge and the hot plasma center are summed in the detector. These effects are inherent in a single-detector system looking along a plasma chord. Profile effects enter the whole problem of spectral interpretation and impurity estimation in such a fundamental way that they must be treated extensively in the theory of measurements (see Chapter 2). They are mentioned here for completeness.

3.5 PLASMA EFFECTS

3.5.1 Plasma Stability

Several effects due to the composition and thermodynamic equilibrium of the tokamak plasma can influence results of x-ray measurements. The plasma is transparent to its own radiation at x-ray energies,[52] so plasma attentuation is not a problem. However, short-period plasma oscillations influence x-ray count rate and spectral shape. In at least one plasma discharge on ISX-B, [number 9191, shown in Fig. 1-1, p. 8] x-ray sawtooth oscillations were nearly synchronous with x-ray spectral acquisition times. For this discharge, alternate low and high electron temperatures were observed.

Plasma oscillations also affect counting rate at the spectrometer, so severe oscillations may cause pileup in data over part of a counting interval. Finally, various heating methods or plasma instabilities may disturb local thermodynamic equilibrium, the existence of which is a major premise in temperature calculations. If the electron velocity distribution is not Maxwellian in a local plasma volume, the x-ray spectrum from that volume does not follow the exponential intensity rule, and hence a "temperature" measurement on that spectrum is not valid. A display of x-ray spectra as a function of time into a discharge is especially useful for spotting nonexponential slopes and other signs of ill behavior (for example, the iron radiation demonstrated by Fig. 1-2, p. 10).

3.5.2 Plasma Composition

Radiation from a plasma depends critically on the composition of the plasma as well as its stability during a discharge. Any impurities present in the plasma enhance x radiation. Heavier elements emit line radiation in the 1-10 keV range, so significant concentrations of these should be identifiable by line radiation. Some experimental conditions have produced identifiable line radiation from iron, nickel, and copper; but these conditions are the exception rather than the rule. Usually, plasma purity must be inferred from enhancement of the continuous spectrum, relative to the calculated intensity for pure hydrogen. (See Section 2.3.)

Calculations of spectral intensity and shape done so far have assumed that a classical derivation for bremsstrahlung (essentially as given by Kramers)[53] holds true. However, there are quantum mechanical

corrections to this derivation which become significant under certain conditions. The formulas for free-free and free-bound intensity given in Section 2.3 include correction factors $\bar{g}_{ff}$ and $\bar{g}_{fb}$, taken as equal to unity in that section. Over the temperature range encountered in tokamaks, $\bar{g}_{fb} = 1$ is a good approximation, so intensities calculated where impurity radiation is a major part of the spectrum are valid for this approximation. For a pure hydrogen spectrum, $\bar{g}_{ff}$ varies over the range 0.15-1.2 for x radiation in the range 1-10 keV and temperatures in the 200-2000 eV range.[54] Thus, calculations of the absolute intensity and spectral shape for pure hydrogen should include the proper Gaunt factor.

The only hydrogen bremsstrahlung calculation in this paper is done in Z_{eff} determinations. For the experimental plasma-detector geometry, temperature, and electron density, an expected intensity from pure hydrogen is determined. The ratio of the experimentally observed intensity to that resulting from the hydrogen computation gives the enhancement η. For computational convenience, the hydrogen intensity is calculated for spectrometer channel 4, $E_j = 2250$ eV. At this energy, the necessary Gaunt factor value can be found from Fig. 3-5. An empirical formula, derived from data published by Karzas and Latter,[55] fits the plot between temperature limits of 300 and 3000 eV.

$$\ln \bar{g}_{ff} = 0.26 \ln T_e(\text{eV}) - 2.08 \qquad (3\text{-}16)$$

The corrected bremsstrahlung intensity for channel 4 is

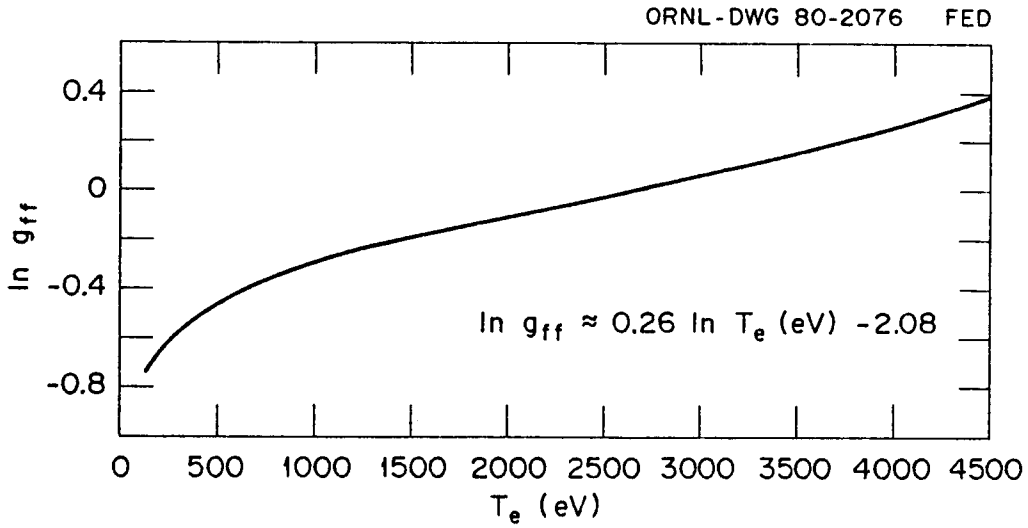

FIGURE 3-5. A plot of $\ell n\ \bar{g}_{ff}$ vs T_e (eV) calculated for E = 2250 eV

$$\ell n\ I = \ell n\ I(\text{classical}) + \ell n\ \bar{g}_{ff}\ (T_e) \qquad (3\text{-}17)$$

3.6 MODELLING AND STATISTICAL ERRORS

Experimental data must be processed by a standard procedure to produce results which are free of personal biases or interpretations. A standard procedure implies a mathematical model to which all data are compared and by which validity of data is judged. As discussed in Chapter 2, the logarithmic expression for x-ray intensity vs energy approximates a straight line, even when profile and impurity effects are present in the spectrum. Therefore, a least-squares linear fit to experimental data has been adopted as the basic model from which intensity and temperature calculations are made. The standard spectral relationship is

$$\lambda(E) = \lambda(0) - E/T_e \qquad (3\text{-}18)$$

where $\lambda(E) = \ell n\ I(E)$. Equation (3-18) is fitted to the experimental data set (E_j, λ_j), where $\lambda_j = \ell n\ (N_j \cdot E_j)$. The electron temperature from the integrated spectrum is

$$T_e = \frac{n(\Sigma\ E_j)^2 - \Sigma(E_j)^2}{n(\Sigma\ E_j)(\Sigma\ \lambda_j) - \Sigma\ E_j\ \lambda_j} \qquad (3\text{-}19)$$

for n data points. The intensity is measured at the zero-energy intercept:

$$\lambda(0) = \frac{\Sigma\ \lambda_j}{n} + \frac{\Sigma\ E_j}{n\ T_e} \qquad (3\text{-}20)$$

A deviation of experimental data points from the straight-line model may be either random or systematic. Appreciable systematic errors warn that the modelling assumptions are not valid for the data set. Severe pulse pileup, non-Maxwellian plasma conditions, and line radiation in the spectrum are possible causes of systematic errors. A measure of systematic error is obtained from the coefficient of determination[56] for the data set:

$$\mathrm{COD} = \frac{\{n\ \Sigma\ E_j\ \lambda_j - \Sigma\ E_j\ \Sigma\ \lambda_j\}^2}{\{n\ \Sigma\ E_j^2 - (\Sigma\ E_j)^2\}\{n\ \Sigma\ \lambda_j^2 - (\Sigma\ \lambda_j)^2\}} \qquad (3\text{-}21)$$

When COD = 1, the data set has no systematic deviation from a linear fit; when COD = 0.9 or less, an examination of the spectral data is advisable.

Random deviations of the data points from the linear fit are expected because of statistical fluctuations. The statistical validity of a temperature calculation can be measured by the standard

deviation of the slope of Eq. (3-16). For the slope $b_o = (-1/T_e)$, the variance is[57]

$$V = \frac{n \Sigma \lambda_j^2 - (\Sigma \lambda_j)^2}{n(n-2)} - \frac{(n \Sigma E_j \lambda_j - \Sigma E_j \Sigma \lambda_j)^2}{n(n-2)\{n \Sigma E_j^2 - (\Sigma E_j)^2\}} \tag{3-22}$$

Statistically, this means that to 66% confidence,

$$b_o - V^{1/2} \leq b_{oTrue} \leq b_o + V^{1/2} \tag{3-23}$$

Since $b_o = -1/T_e$, the standard deviation in T_e is given by

$$SD = \frac{V^{1/2}}{V - (1/T_e)^2} \tag{3-24}$$

For a normal spectrum, the standard deviation is usually 5-10% of the temperature.

CHAPTER 4

EXPERIMENTAL RESULTS

4.1 INTRODUCTION

This chapter presents analyses of representative data from three generations of Oak Ridge tokamaks: ORMAK, ISX-A, and ISX-B. The data have been selected to demonstrate the contribution of time-resolved T_e and Z_{eff} measurements to the general understanding of tokamak behavior and to show the correlation of x-ray data with the results from other plasma diagnostics. In the following examples, frequent comparisons are made between the results found from x-ray energy analysis and those from the Thomson-scattering laser data and resistivity calculations. Most of the examples use data collected over a sequence of discharges. Since the x-ray analyzer can resolve a single discharge into 25 time intervals, the reason for using averaged data for most of the illustrations may be questioned. However, sequences and averages provide the only method for arriving at comparative results for the two diagnostic techniques, and even with averages, caveats exist.

Laser data provide the accepted comparison for electron temperature measurements, and generate experimental temperature and density profiles for resistivity calculations. However, the laser is limited to four (at most) instantaneous measurements during a discharge. Each measurement gives temperature and relative density at a specific spatial point in the plasma and at a specific time into the discharge. (For many sequences, technical problems have limited laser

data to only one or two points per discharge.) Thus, profiles and time histories must be built up point by point over several discharges, and valid conclusions require that all discharges in a sequence be nearly identical. Usually two or three laser measurements of each space-time point in a profile are made during sequential discharges. This lengthens the total process of obtaining a profile, so most sequences are documented by laser data for only one or two times during the discharge. Even these data are averages in only a limited sense, since each plasma profile is inferred from measurements made at discrete spatial points and spanning many discharges.

In contrast, the x-ray diagnostic acquires a time history of T_e for each discharge in the sequence. However, time resolution is only 10 ms, and observed data are line-integral (as opposed to the point measurements from the laser). Since most sequences include discharges with noticeably different density or temperature histories, x-ray data varies from discharge to discharge. Consequently, the most nearly comparative data seems to be that from the laser and the x-ray, each "averaged" in its own peculiar way over several discharges. The x-ray data are averaged by adding successive data matrices together, spectrum by spectrum and channel by channel, and using the resulting composite data array just as if it had come from a single discharge. In most cases, x-ray analyses agree with Thomson-scatter T_e measurements and Spitzer resistivity Z_{eff} estimates. One notable exception involves electron-cyclotron heating, the last example presented.

The analysis process which converts spectrometer counts per channel into quantitative T_e and Z_{eff} results is quite complex, and the primary discussion of the steps involved is dispersed through two chapters and two appendices. A better understanding of the complete analysis procedure will come from a study of Appendix C, which lists the operations required and the equations used for extracting numerical T_e and Z_{eff} values from spectrometer data. Most of the figures and tables presented in this chapter are reproductions of computer-generated tables and plots; and so some of the column headings and notations may seem obscure, unless Appendix C is reviewed before these figures are examined.

4.2 ORMAK DATA: ELECTRON HEATING BY NBI

One of the first tokamak experiments in which time-resolved x-ray energy analysis contributed significantly to the description and understanding of an important plasma effect took place in December, 1976.[58] That experiment involved injection of 340 kW of power, carried by a beam of neutral hydrogen, into an established low-density plasma in ORMAK. The anticipated effect, heating of plasma electrons by the energetic neutral beam, was documented by the x-ray diagnostic and by Thomson scattering. X-ray data provided a time-resolved history of each discharge in the sequence, while Thomson-scattering measurements were made point by point during 35 discharges, for various times and plasma radii.

A three-axis plot of x-ray data summed over 15 tokamak discharges during the neutral beam injection sequence is shown in Fig. 4-1. Due to timing changes in the analysis routine made since this data was

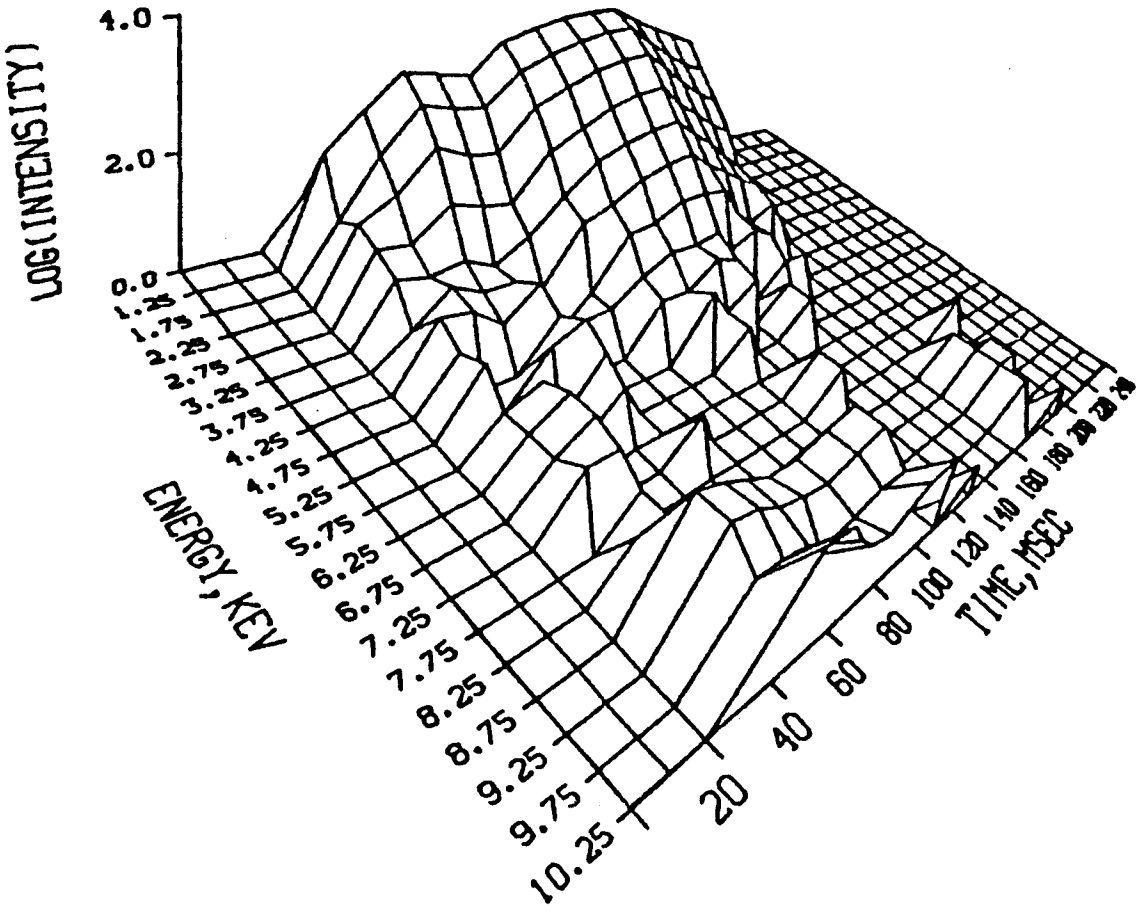

FIGURE 4-1. A three-axis plot of x-ray spectra for the ORMAK NBI electron heating experiment

collected, the discharge begins at the 20 ms time point. Approximately 40 ms later, neutral beam injection begins to raise both plasma temperature and x-ray intensity; the "thermal ridge" grows higher (in intensity) and less steep (as spectra extend to higher energies). Some electrical noise and possibly sporadic line radiation shows as peaks and ridges above 6 keV, but the energy region below 3 or 4 keV has the characteristic appearance of thermal bremsstrahlung, except for the first spectrum at the 30 ms time.

Unprocessed spectrometer data for the 15 discharges is summed to give the listing shown in Table 4-1. The first column of figures gives the time at which a spectrum was stored, in 10 ms intervals. Columns 2-10 list the counts contained in the first 9 energy channels of the pulse-height analyzer for the given time interval, and the last column (channel 20) lists the high-energy ($\geq$ 10 keV) x-rays detected. Thus, the matrix can contain a maximum of 25 energy spectra, one spectrum per row. Counts in channel one are lower than those in channel two because a discriminator in the pulse-height analyzer is purposely set to cut off the spectrum at 750-800 eV. Note that most spectra contain 10^3-10^5 counts, so statistical fluctuations should be small.

When the data in Table 4-1 is subjected to the routines described in Appendix C, the listing given in Table 4-2 results. The first and second columns give the lowest and highest spectrometer channels used in the least-squares calculation. The third channel lists the mean value of the data-collection interval. (This value has been corrected to reflect the true time; e.g., 15 ms corresponds to the spectrum

TABLE 4-1. A listing of unprocessed spectrometer data summed over 15 discharges in an ORMAK NBI sequence

0	0	0	0	0	0	0	0	0	0	0
10	0	0	0	0	0	0	0	0	0	0
20	0	0	0	0	0	0	0	0	0	0
30	9	70	7	11	7	4	1	4	2	154
40	10	308	73	25	6	3	4	3	0	121
50	11	1196	446	127	22	4	2	1	0	35
60	9	939	313	71	15	2	2	4	2	20
70	4	775	273	63	12	5	1	0	1	12
80	16	2600	1016	340	86	22	12	1	1	26
90	27	4069	1761	677	191	72	20	10	3	36
100	62	5696	2751	1126	354	120	44	12	6	7
110	76	6948	3603	1558	543	177	66	24	6	8
120	66	7253	3950	1718	614	212	85	25	7	10
130	27	4233	1948	794	241	98	37	21	2	1
140	20	2581	929	353	119	48	20	5	4	2
150	12	1643	500	178	58	19	10	2	2	1
160	11	1090	333	102	33	9	6	4	0	1
170	0	239	64	26	7	0	0	1	0	4
180	0	16	1	0	0	0	0	0	0	3
190	0	0	0	0	0	0	0	0	0	1
200	0	0	0	0	0	0	0	0	0	0
210	0	0	0	0	0	0	0	0	0	0
220	0	0	0	0	0	0	0	0	0	0
230	0	0	0	0	0	0	0	0	0	0
240	0	0	0	0	0	0	0	0	0	0

TABLE 4-2. Calculated x-ray data for a sum of 15 discharges in an ORMAK NBI sequence

LO	HI	TIME	TE	TE PEAK	COD	ERR	TOTCTS	ZEFF
2	6	15.	531.99	600.70	0.99	8.75	543.	0.00
2	6	25.	415.04	462.33	0.97	7.82	1833.	0.00
2	6	35.	385.25	427.66	0.98	8.11	1368.	0.00
2	6	45.	460.90	516.17	0.99	8.10	1142.	0.00
2	6	55.	518.10	584.08	0.98	7.18	4104.	0.00
2	6	65.	630.73	720.29	0.98	6.82	6839.	0.00
2	6	75.	674.99	774.72	0.97	6.59	10116.	0.00
2	6	85.	727.85	840.39	0.96	6.45	12933.	0.00
2	6	95.	761.77	882.92	0.96	6.41	13874.	0.00
2	6	105.	688.88	791.91	0.98	6.74	7375.	0.00
2	6	115.	652.62	747.14	1.00	7.08	4061.	0.00
2	6	125.	574.00	651.27	1.00	7.45	2413.	0.00
2	6	135.	524.00	591.13	1.00	7.76	1578.	0.00

taken between 10 and 20 ms after the beginning of the tokamak discharge.) Chord-integral and estimated peak electron temperature are found in the fourth and fifth columns; the coefficient of determination (COD = 1 is good) in the sixth; and the estimated standard deviation expressed in eV is given in the seventh. The total counts in each spectrum (needed for an estimation of pulse pileup) is listed in the eighth column, and Z_{eff} is given last. In this case, density information could not be recalled from the data archives, and so Z_{eff} is not calculated..

For the data shown here, all calculations were performed between channels two and six, inclusive, to avoid nonthermal spectral components. The resulting COD values indicate good linearity in all spectra, and the statistical error is less than 2% for any T_e value. (The error column only lists calculated statistical errors, so other error sources, such as pileup, may increase the error to 8-10%.)

If the temperature data in Table 4-2 is plotted against time, the graph in Fig. 4-2 results. The 40-ms duration of neutral beam injection is indicated on the time axis. Just before injection begins, x-ray measurements give $T_e \approx 400$ eV. Temperature rises steadily during injection and continues to increase for ~20 ms after injection stops reaching a maximum central value of ~900 eV. The plot clearly shows the temperature buildup and decay times characteristic of electron heating by NBI.

Figure 4-3 gives the T_e vs time information originally published for this study.[59] At the time of the experiment, several aspects of the present theory of measurement were not developed, so x-ray data

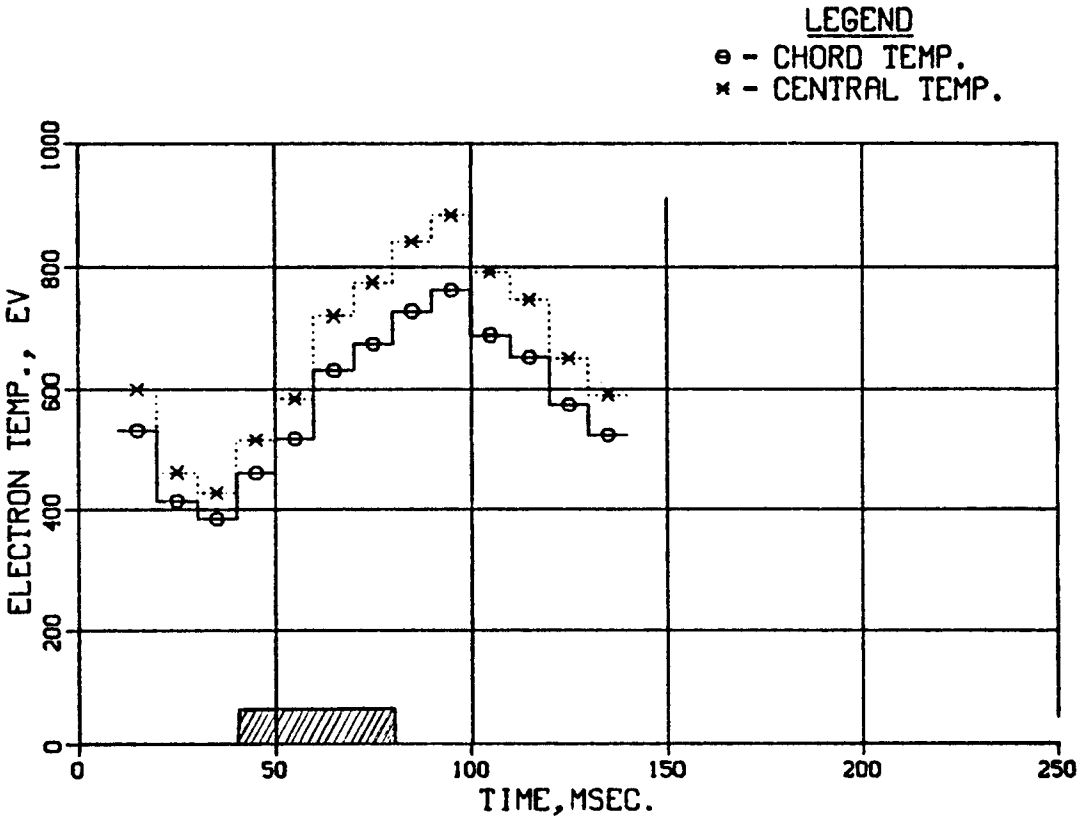

FIGURE 4-2. A plot of T_e vs time for 15 discharges in the ORMAK NBI electron-heating experiment

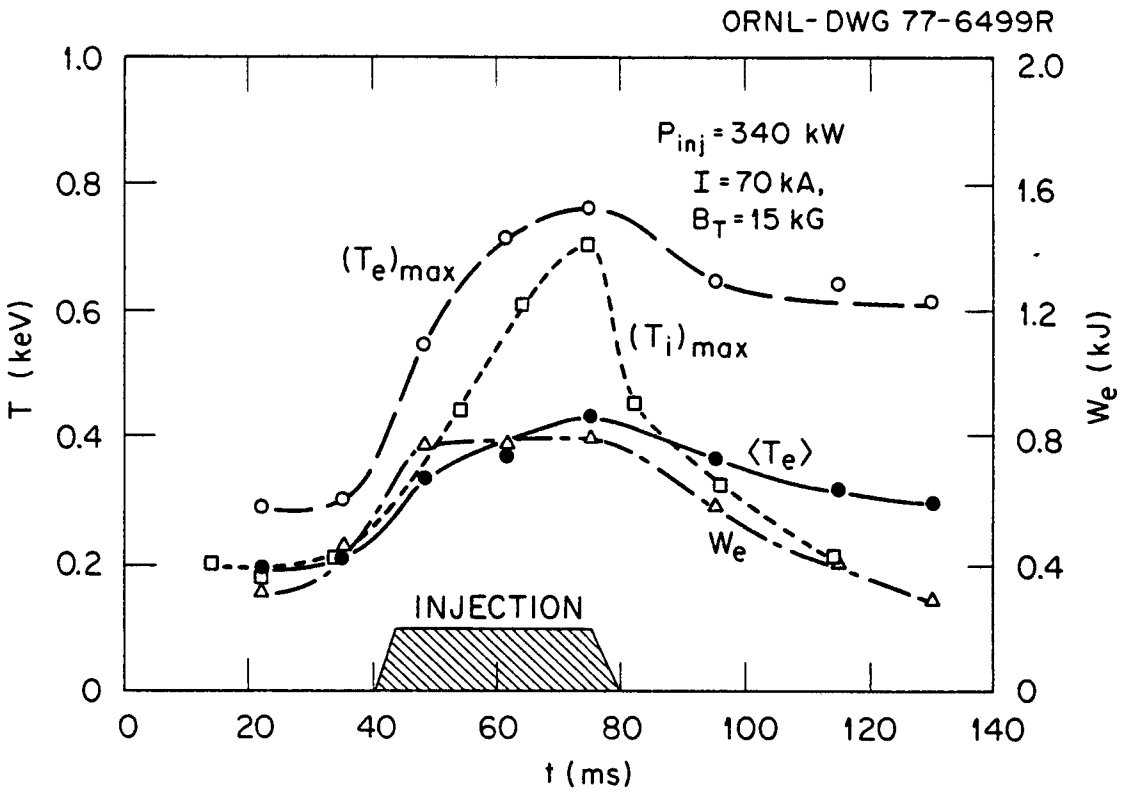

FIGURE 4-3. A summary of T_e vs time values derived from Thomson-scattering data for the ORMAK electron-heating experiment

were used mainly to demonstrate temporal behavior; the quantitative temperature values were obtained by Thomson scattering. However, a comparison of Figs. 4-2 and 4-3 demonstrates the excellent agreement of present calculations with the original quantitative data.

4.3 ISX-A RESULTS

In the design of ISX-A, special care was taken to exclude organic contaminants and heavy metals from the vacuum vessel. The plasma cross section was circular, plasma heating was achieved exclusively by the circulating plasma current (ohmic heating), and plasma position was controlled by feedback-corrected amplifiers. The vacuum vessel and limiter were fabricated from stainless steel.

The ISX-A experimental program was divided into three areas of specialization: a study of plasma-wall interactions done jointly with the Metals and Ceramics Division of ORNL, a collaborative effort with General Atomic Company to investigate the phenomenon of impurity flow reversal, and the measurement of plasma parameters and confinement times. Confinement studies were done for two methods of vacuum vessel conditioning: discharge cleaning, and titanium gettering. Examples of data for these two methods are presented here.

4.3.1 Behavior of Plasma Parameters Following Discharge Cleaning

Discharge cleaning, in which a low-power plasma is generated by the repetitive discharges of a relatively small capacitor bank into the tokamak ohmic heating windings, is a standard method for "scrubbing" the liner walls. For the confinement sequence 01128G.A, discharge cleaning was applied continuously for ten hours prior to

commencing the experiment. Thus, any titanium surfaces in the vacuum chamber were loaded with hydrogen. The sequence was done at a toroidal field of 14.8 kG and a plasma current of 130 kA. A gas injection system was used to "puff" gas into the vacuum liner once a discharge was initiated, and thus increase plasma density as the discharge progressed.

For a four-discharge average in the sequence, Fig. 4-4 gives plots of chord-integrated and central electron temperatures derived from x-ray data. The central electron temperature averages approximately 700 eV throughout the discharge, peaking slightly during the density rise and again at the end. X-ray data are in good agreement with the laser values of 780 and 750 eV for peak T_e at 130 and 150 ms, respectively. Because of a peculiarity in the computer timing for ISX-A, x-ray data are not available for the first 30 ms of the discharge.

Data from a single discharge typical of the sequence is illustrated in the next figures. Temperature and density vs time are plotted in Fig. 4-5. A comparison of this figure with Fig. 4-4 reveals temperature variations of ~15%, typical of shot-to-shot differences encountered even in good sequences, and illustrates the additional information provided by a time history of a single discharge. Table 4-3 lists calculations for x-ray data from this discharge. The counting rate at peak density was somewhat high, but with pileup corrections the linear fit to the data was good, and statistical variations were small. Thus, reliable temperature and density data were available for the Z_{eff} calculation plotted in

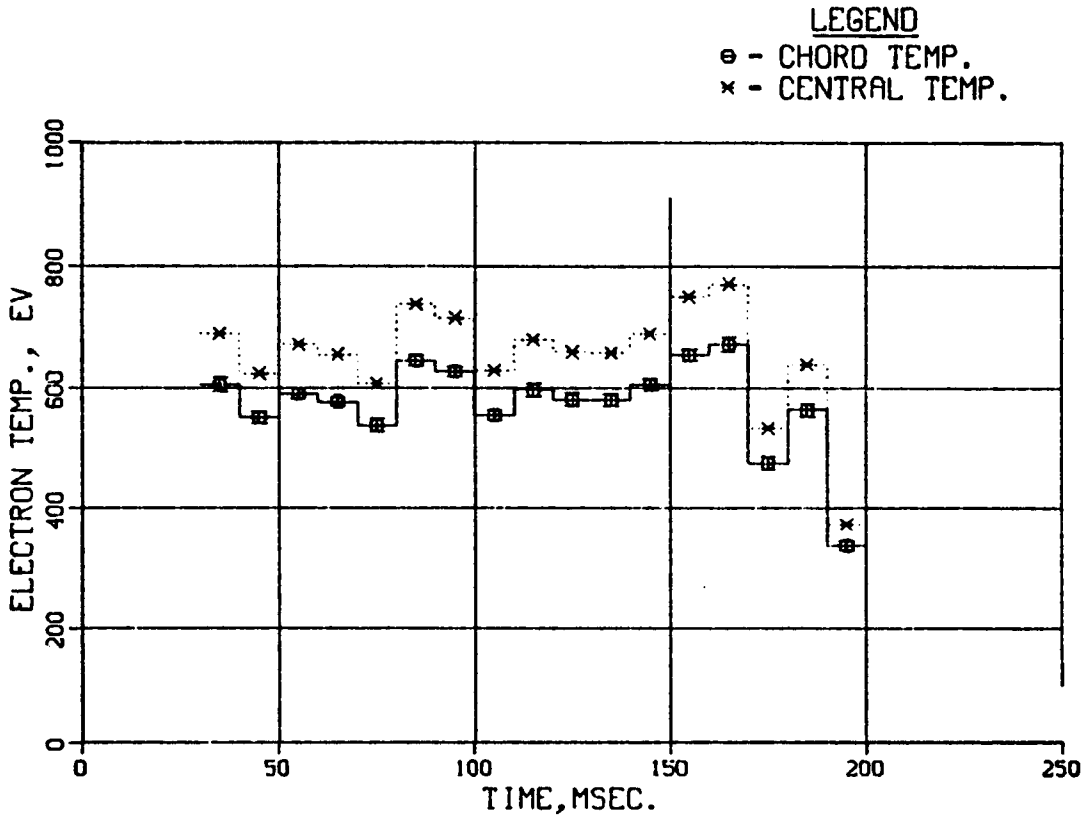

FIGURE 4-4. A plot of T_e vs time for an average of four ISX-A discharges taken after discharge cleaning

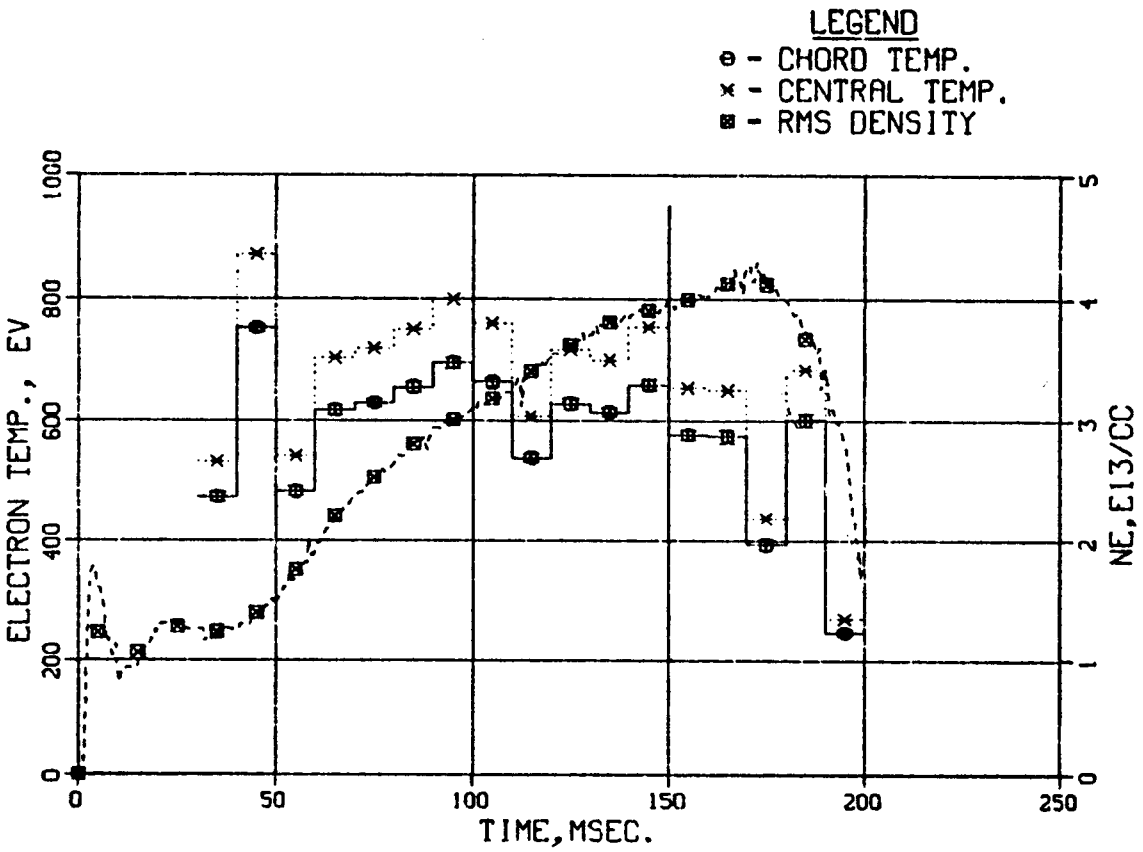

FIGURE 4-5. Plots of T_e and N_e vs time for a single ISX-A discharge taken after discharge cleaning

TABLE 4-3. Calculated x-ray data for an ISX-A discharge in a confinement study following discharge cleaning

LO	HI	TIME	TE	TE PEAK	COD	ERR	TOTCTS	ZEFF
4	9	35.	473.70	531.29	0.95	7.68	1905.	6.00
4	8	45.	752.26	870.96	0.98	5.53	2151.	6.00
4	9	55.	482.06	541.19	0.94	7.67	1808.	6.00
4	9	65.	617.33	703.92	0.95	7.60	1863.	4.88
4	8	75.	629.57	718.87	1.00	5.73	1918.	4.75
4	10	85.	655.73	750.98	0.99	9.13	1933.	3.21
4	10	95.	695.35	799.93	0.97	9.06	2015.	2.14
4	9	105.	663.68	760.76	1.00	7.22	2068.	2.37
4	9	115.	538.37	608.35	0.95	7.39	2025.	3.15
4	10	125.	628.40	717.44	0.98	8.90	2165.	2.24
4	9	135.	614.61	700.59	0.96	7.14	2161.	2.40
4	10	145.	658.84	754.80	0.99	8.92	2013.	1.59
4	9	155.	577.12	655.05	0.94	7.36	1967.	1.85
3	9	165.	574.01	651.29	0.99	10.26	1563.	1.23
2	6	175.	394.02	437.84	0.99	8.76	592.	1.02
2	7	185.	601.10	684.14	0.99	9.97	1053.	1.00
2	4	195.	247.10	269.86	0.99	4.75	117.	1.01

Fig. 4-6. At the times available from laser measurements, x-ray and laser Z_{eff} values are comparable: 2.01 at 130 and 150 ms from resistivity calculations, and ~2.1 and 1.6 for x-ray data at corresponding times.

The most interesting feature of the Z_{eff} plot is the steady decrease in Z_{eff} with time, from ~4.4 at 65 ms to ~1.2 at 165 ms. In the same time, the density rises from $\sim 2.2 \times 10^{13}$ to $\sim 4.2 \times 10^{13}$, line-average value. From the definition of Z_{eff},

$$Z_{eff} = \frac{N_H + N_i Z_i^2}{N_e} \qquad (4\text{-}1)$$

taking $N_H \simeq N_e$ and assuming that the total impurity content of the plasma is relatively constant,

$$Z_{eff} - 1 \propto \frac{1}{N_e} \qquad (4\text{-}2)$$

Qualitatively, this is the behavior exhibited, except that Z_{eff} falls much more than would be expected from a simple dilution of impurities by the injected hydrogen. One possible reason for this is that the extreme gas puff used to produce the density increase cools the plasma edge and reduces the impurity influx from the vacuum walls, so the plasma actually loses impurities as the discharge progresses.[60]

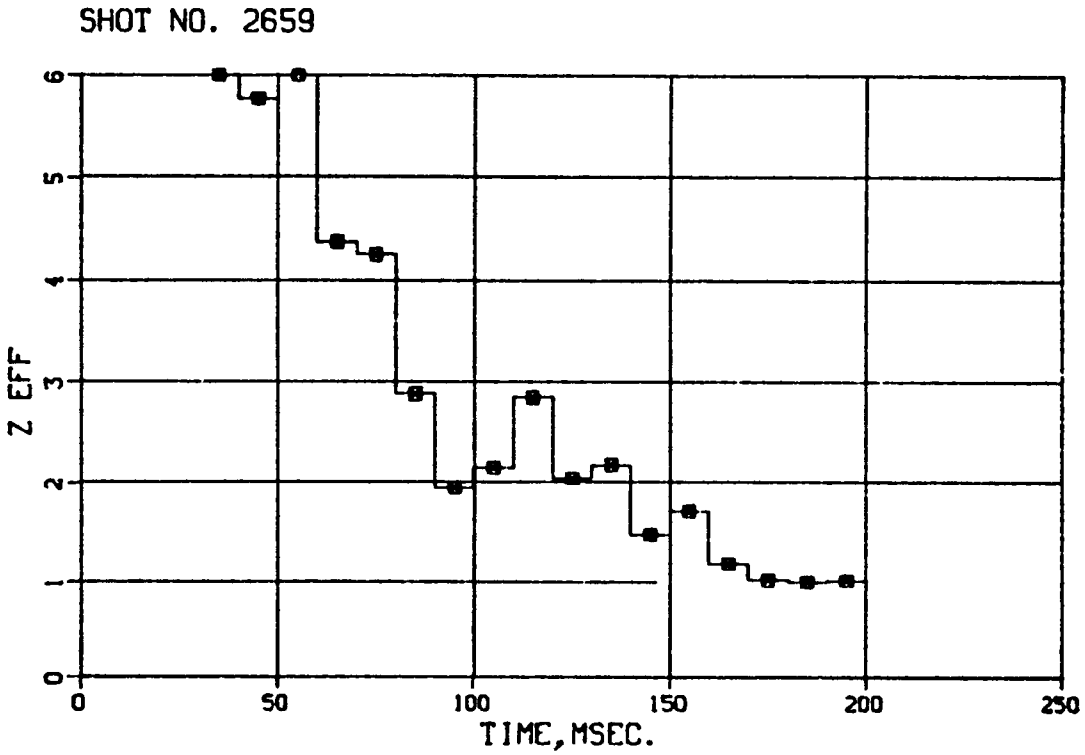

FIGURE 4-6. A plot of Z_{eff} vs time for a single ISX-A discharge taken after discharge cleaning

4.3.2 Behavior of Plasma Parameters Following Titanium Gettering

A second method of conditioning the ISX-A vacuum vessel was titanium gettering; this technique was expected to reduce impurity recycling from vacuum walls. Titanium evaporators were installed as part of the collaborative experiment with General Atomic and used especially in conjunction with impurity flow reversal experiments, but some confinement studies were also done under gettered conditions. One such study involved sequence 02188D.1JX, done at a toroidal field of 12.8 kG and a plasma current of 120 kA. Because of the fresh titanium surfaces, these experiments began with a very low base pressure and required strong gas injection to increase plasma density.

Data from six discharges in this sequence were averaged to calculate the T_e vs time plots shown in Fig. 4-7. X-ray intensities were too low to provide T_e data before 50 ms, but from 50 to 150 ms, central T_e averaged ~500 eV. This is considerably below the laser values of 857 and 670 eV obtained at 110 and 130 ms. However, this sequence evidenced wider variations between individual discharges than is typically observed from x-ray data, and similar sequences earlier and later in the day produced peak T_e values from laser measurements ranging from 525 eV to 1070 eV.

Figure 4-8 shows data from one shot in the sequence. Note the change in density by over an order of magnitude during the discharge and the fluctuations in T_e over the 50-150 ms time span. Table 4-4 lists calculations for this discharge. Total counts per spectrum are rather low, especially during the first half of the discharge, and some COD values indicate more spectral nonlinearity than usual. Data

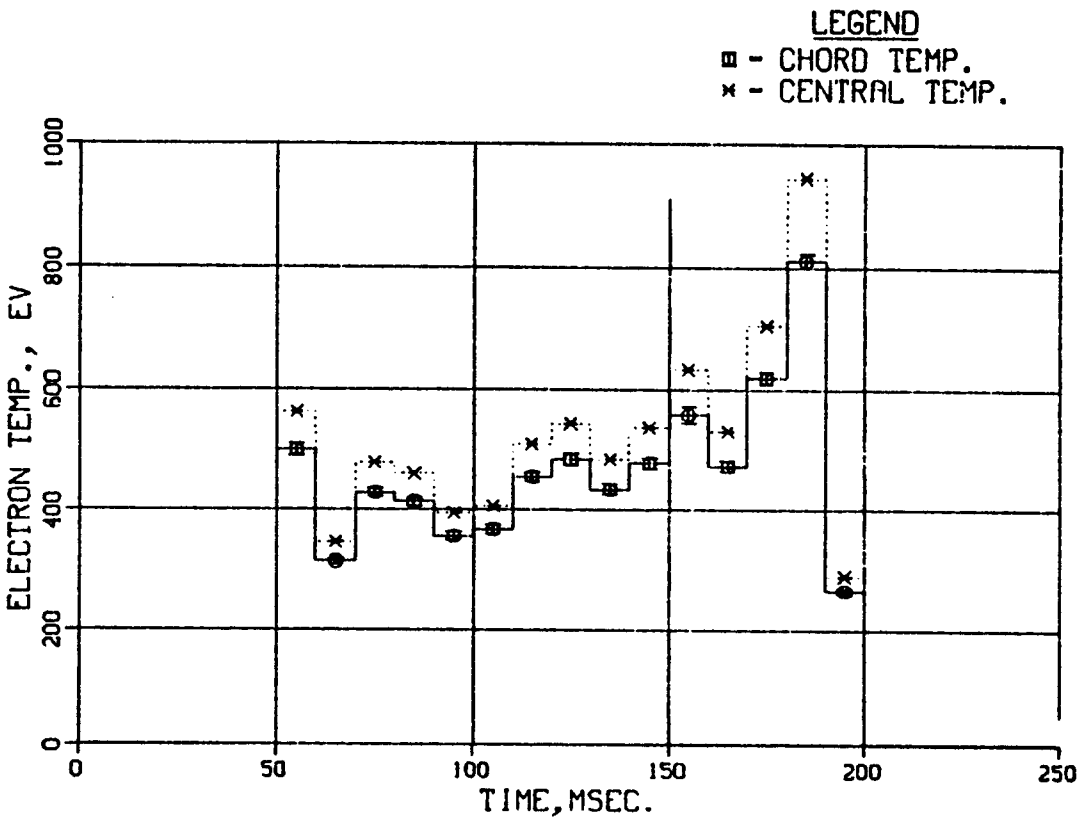

FIGURE 4-7. A plot of T_e vs time for an average of six ISX-A discharges taken after titanium gettering

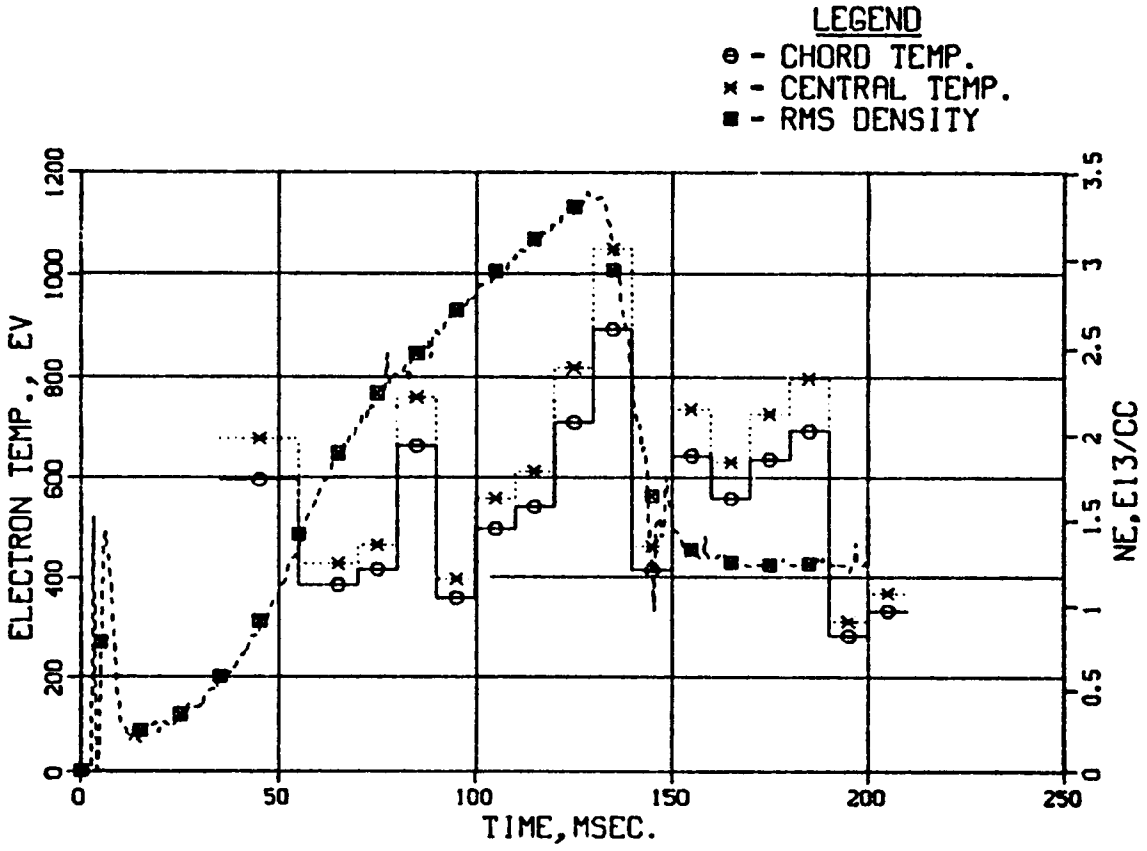

FIGURE 4-8. Plots of T_e and N_e vs time for a single ISX-A discharge taken after titanium gettering

TABLE 4-4. Calculated x-ray data for an ISX-A discharge in a confinement study following titanium gettering

LO	HI	TIME	TE	TE PEAK	COD	ERR	TOTCTS	ZEFF
2	6	45.	595.50	677.33	0.83	10.41	109.	6.00
2	4	65.	384.30	426.56	0.92	4.38	210.	6.00
2	4	75.	416.16	463.64	0.91	4.28	254.	6.00
2	7	85.	663.66	760.73	0.85	11.60	274.	3.16
2	5	95.	359.12	397.43	0.93	7.14	244.	4.04
2	6	105.	496.79	558.68	0.90	9.91	162.	1.70
2	6	115.	541.42	612.01	0.97	9.40	209.	1.80
2	8	125.	710.53	818.79	0.92	13.70	310.	1.39
2	10	135.	892.97	1050.21	0.74	17.47	458.	1.20
2	6	145.	414.22	461.37	0.98	8.78	551.	3.73
2	8	155.	643.88	736.41	0.86	12.65	735.	2.27
2	8	165.	557.90	631.84	0.98	12.58	839.	3.78
4	9	175.	636.81	727.73	1.00	7.44	1722.	6.00
4	10	185.	693.30	797.38	0.93	8.63	1693.	6.00
2	4	195.	283.84	311.35	1.00	4.95	72.	4.38
2	4	205.	333.81	368.32	0.86	5.29	45.	2.28

from PIN diodes for this sequence indicates very strong sawtooth oscillations on the x-ray signals, especially during the 80-140 ms time interval.[61] There is evidence from other x-ray energy data that these oscillations change the x-ray spectral distribution, and thus present varying temperature information to the detector, so apparently the erratic T_e values and less linear spectra are caused by the generally fluctuating plasma conditions. Figure 4-9 reveals another interesting feature of this sequence; the average of six discharges shows clear signs of characteristic iron radiation as well as the usual thermal spectra. The feature at 140-150 ms is also recorded in PIN diode data, and corresponds to a large burst of MHD activity during the density decay shown in Fig. 4-8.

Figure 4-10 plots the behavior of Z_{eff} as calculated for the single discharge 4343. The values between 100 and 140 ms agree well with resistivity calculations of $Z_{eff} = 1.65$ and 1.57 at 110 and 130 ms, respectively. As in the last example, Z_{eff} derived from x-ray data falls sharply during the discharges and reaches a minimum value of 1.2 at 135 ms, approximately at peak density. This low value of Z_{eff} is interesting, considering the evidence for iron radiation present in Fig. 4-9. X-ray line radiation is decidedly atypical in tokamak discharges; this is one of very few sequences which show any evidence of it. Since Z_{eff} is so low, this might be an instance where the detector is seeing wall radiation. Several aspects of this sequence are intriguing: evidence of strong fluctuations in x-ray output from the three-axis plot and PIN diode signals, large fluctuations in temperature from discharge to discharge, evidence of

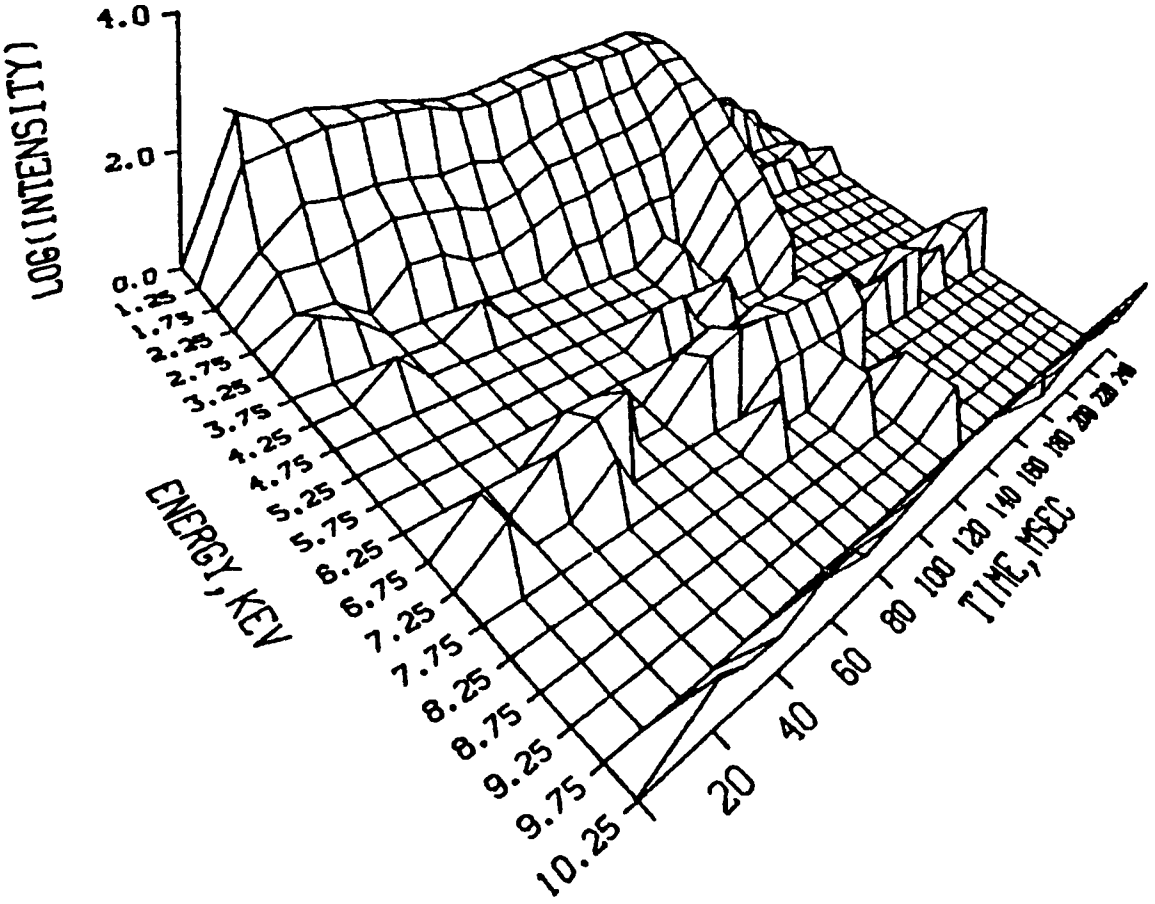

FIGURE 4-9. A three-axis plot of x-ray spectra vs time for an average of six ISX-A discharges taken after titanium gettering

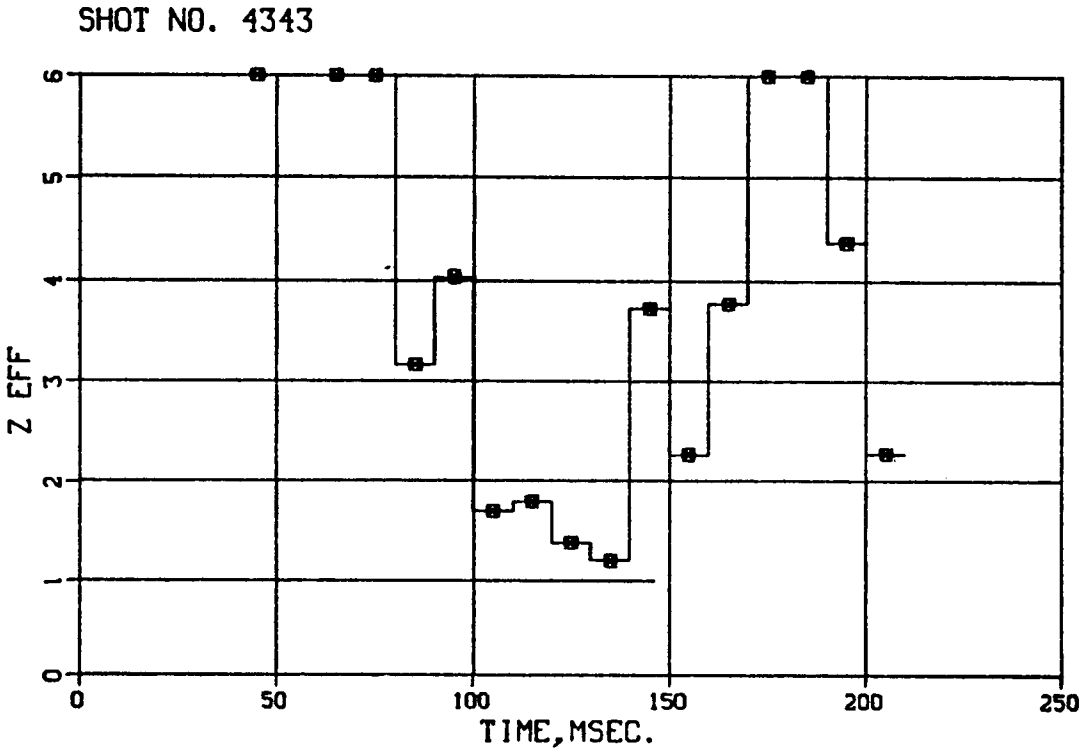

FIGURE 4-10. A plot of Z_{eff} vs time for a single ISX-A discharge taken after titanium gettering

iron line radiation, and yet a low value of Z_{eff} from both x-ray and resistivity calculations.

4.4 ISX-B RESULTS

ISX-B, the present Oak Ridge tokamak, uses toroidal field coils and power supplies from ISX-A, but is essentially a new machine. The vacuum vessel has a rectangular cross section to accommodate elliptical or D-shaped plasmas, and the confining and stabilizing windings are arranged to generate these plasma shapes on demand. ISX-B is also designed to apply a variety of heating methods to the plasma: resistive, neutral beam, and electron cyclotron. Access for pellet fueling experiments and a wide variety of diagnostic apparatus is provided in this machine. A large part of the experimental program on ISX-B has been devoted to exploring the higher-β operating parameters possible with the plasma heating methods available.

4.4.1 Behavior of T_e During Pellet Injection

One proposed method of refueling a fusion power reactor is by firing a pellet of frozen hydrogen into the established plasma. The pellet sublimes to provide fuel to continue the reaction. Pellet injection experiments on ISX-B have been successful in introducing a pellet into an experimental plasma; abrupt changes in density (~30-50%) and temperature (reduction to ~100 eV) are seen in the plasma. These experiments provide a demonstration of the time resolution of the x-ray measurements.

Figure 4-11 is a plot of temperature and density vs time for a particularly dramatic pellet shot. The marked drop in temperature and

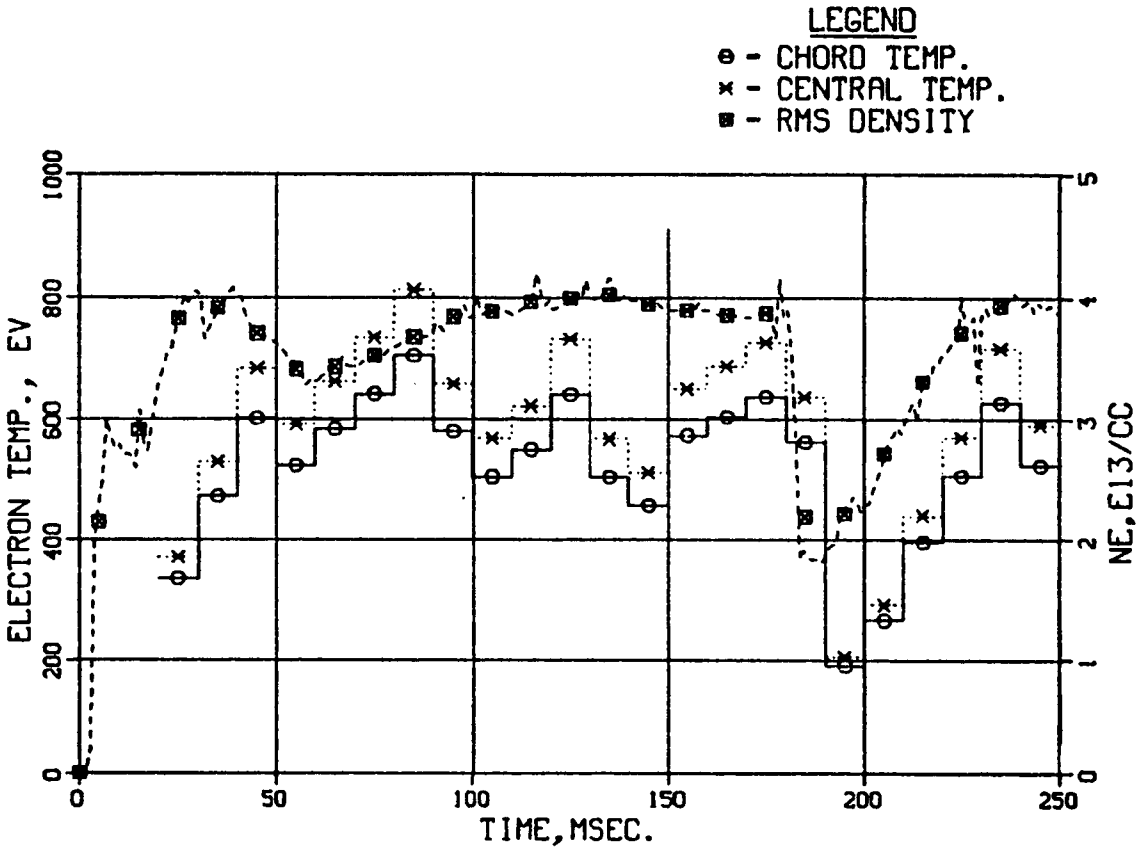

FIGURE 4-11. Plots of T_e and N_e vs time for a pellet-injection experiment on ISX-B

the discontinuity in density are apparent at ~185 ms. Since the temperature from x-ray data is averaged over 10 ms, the minimum temperature shown in Fig. 4-11 is somewhat higher than the Thomson-scattering value of ~120 eV, but the x-ray plot does show the recovery time scale for T_e quite well.

The density trace in this figure does not represent what really happens during pellet injection, since the microwave interferometer cannot follow abrupt density changes of such magnitude. Of course, the pellet and associated gas burst from the injector represent a substantial increase in density. The amount of this increase cannot be given with real certainty, but a reasonable estimate makes $N_e \sim 5.1 \times 10^{13}$/cc at 185 and 195 ms. For these values, the plot of Z_{eff} vs time given in Fig. 4-12 can be corrected to $Z_{eff} \sim 1.2$ at 185 ms, and $Z_{eff} \sim 1.1$ at 195 ms. Resistivity calculations for 150 and 170 ms give Z_{eff} of 1.13 and 1.34 respectively, so again, x-ray and resistivity values are in close agreement. Corrected density estimates indicate that Z_{eff} decreases slightly with pellet injection, as would be expected from a dilution of the plasma impurities by the injected hydrogen.

4.4.2 Behavior of Plasma Parameters During NBI

ISX-B is designed to accept neutral beams from two injectors, with a maximum planned power level of 1.8 MW. Injection heating increases both electron and ion temperatures in a plasma, and thus allows tokamak experiments to be carried out at higher plasma pressures β_p

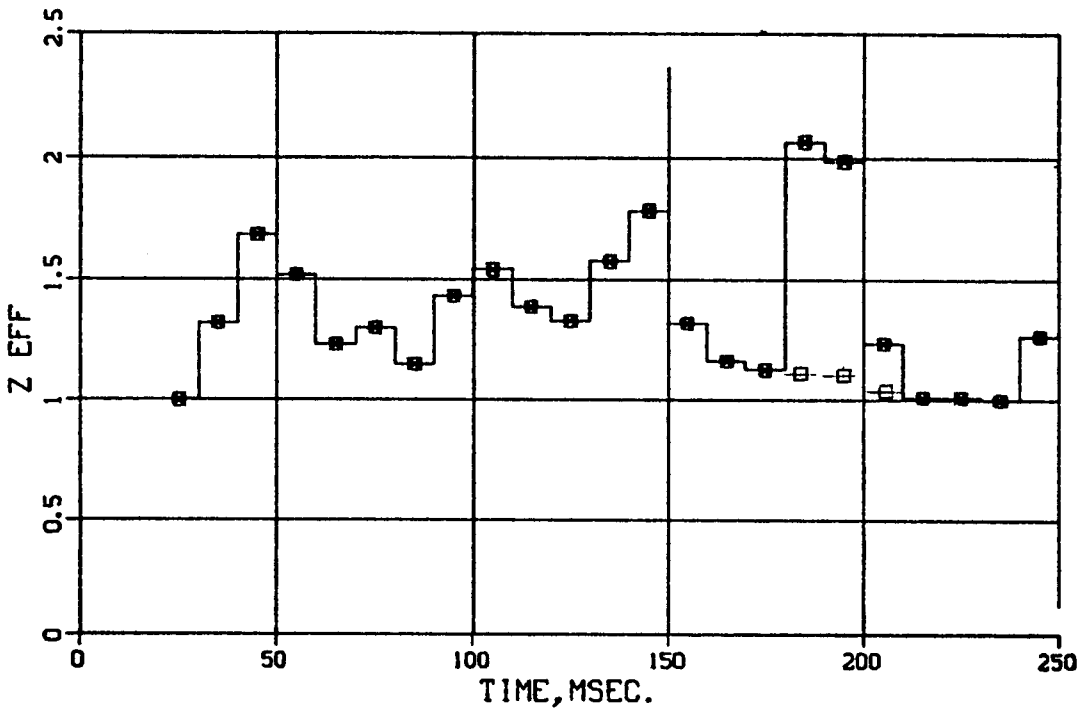

FIGURE 4-12. A plot of Z_{eff} vs time for a pellet-injection experiment on ISX-B

$$\beta_p = \frac{8\pi\ N(T_e + T_i)}{B^2_{poloidal}} \qquad (4\text{-}3)$$

than can be reached by resistive heating alone. Several NBI sequences have been done on ISX-B. One such sequence in which a single injector was used to provide 450 kW of injected power is 103092.DHX. This is approximately 30% more power than was available for the ORMAK injection experiment described earlier. The toroidal field strength was 9.2 kG, and plasma current was ~110 kA for this experiment. Figure 4-13 shows T_e values calculated for an average of ten discharges in the sequence. Injection begins at 70 ms and lasts until 160 ms. Preinjection temperature is ~400-450 eV, in good agreement with a laser value of 491 eV. X-ray data show the temperature rising steadily during injection and for ~30 ms after injection stops, to reach a maximum central value of ~1300 eV. Laser data indicate central temperatures of 930 eV at 110 ms and 1040 eV at 130 ms, about 20% higher than x-ray values.

A single discharge from this sequence provides the data for Fig. 4-14. The density trace demonstrates a phenomenon called "density clamping" at approximately 110 ms. Until this time, the plasma density increases, due to influx of hydrogen from the gas puff, but past this time, the density is held approximately constant for the duration of injection. Once NBI stops, the density resumes its initial rising trend. This phenomenon is the subject of current investigation, and is not yet understood.

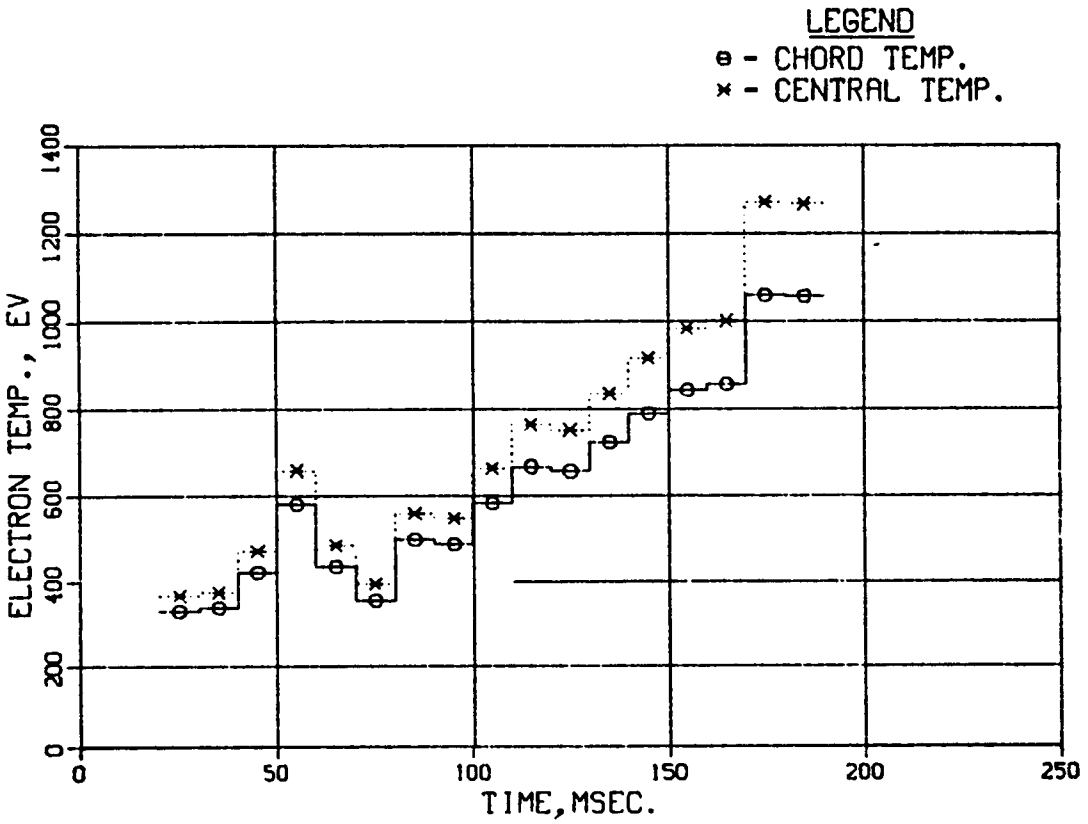

FIGURE 4-13. A plot of T_e vs time for an average of ten discharges in an ISX-B injection sequence

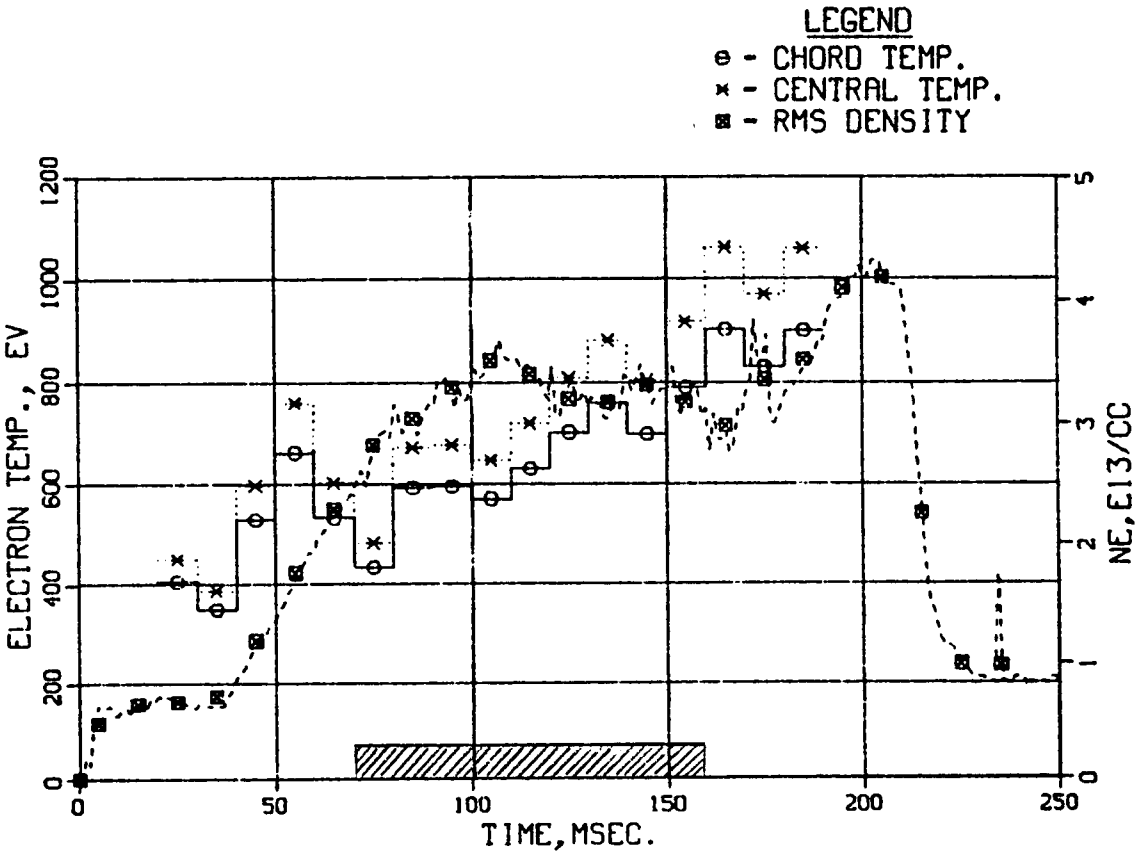

FIGURE 4-14. Plots of T_e and N_e vs time for a discharge in an ISX-B injection sequence

The temperature behavior of the single discharge is quite similar to that of the ten-discharge average. A three-axis plot given in Fig. 4-15 shows a well-behaved thermal spectrum and no signs of line radiation, except at very late times (~140-170 ms).

The calculations in Table 4-5 reveal satisfactory spectral linearity, small statistical errors, and adequate count rates. The Z_{eff} values are plotted in Fig. 4-16.

An interesting feature of this plot is that Z_{eff} rises during injection from a very low value to a maximum of ~4 at 150 ms. Resistivity calculations for this sequence do not indicate this trend, giving Z_{eff} ~3.07 at 71 ms and ~2.68 at 110 and 130 ms. X-ray data show that this rising trend is typical of this particular sequence but not of injection sequences in general. (An earlier ISX-B injection sequence shows Z_{eff} falling during injection.) Since x-ray spectral data and the interferometer density trace for this discharge are both apparently noise-free and statistically valid, the Z_{eff} calculation should also be valid. There is evidence from optical spectrometry that the interior concentrations of heavy elements such as iron tend to decrease during NBI,[62] but the x-ray spectra show no real evidence of iron lines, so the observed Z_{eff} increase in this case must be due to lighter elements.

This example illustrates several interesting properties of a high-β plasma: density clamping and the question of gas feed rate vs particle transport in the plasma, temperature behavior during NBI, and Z_{eff} behavior during NBI and the question of how impurity transport is affected by injection. For such studies, where there is a possibility

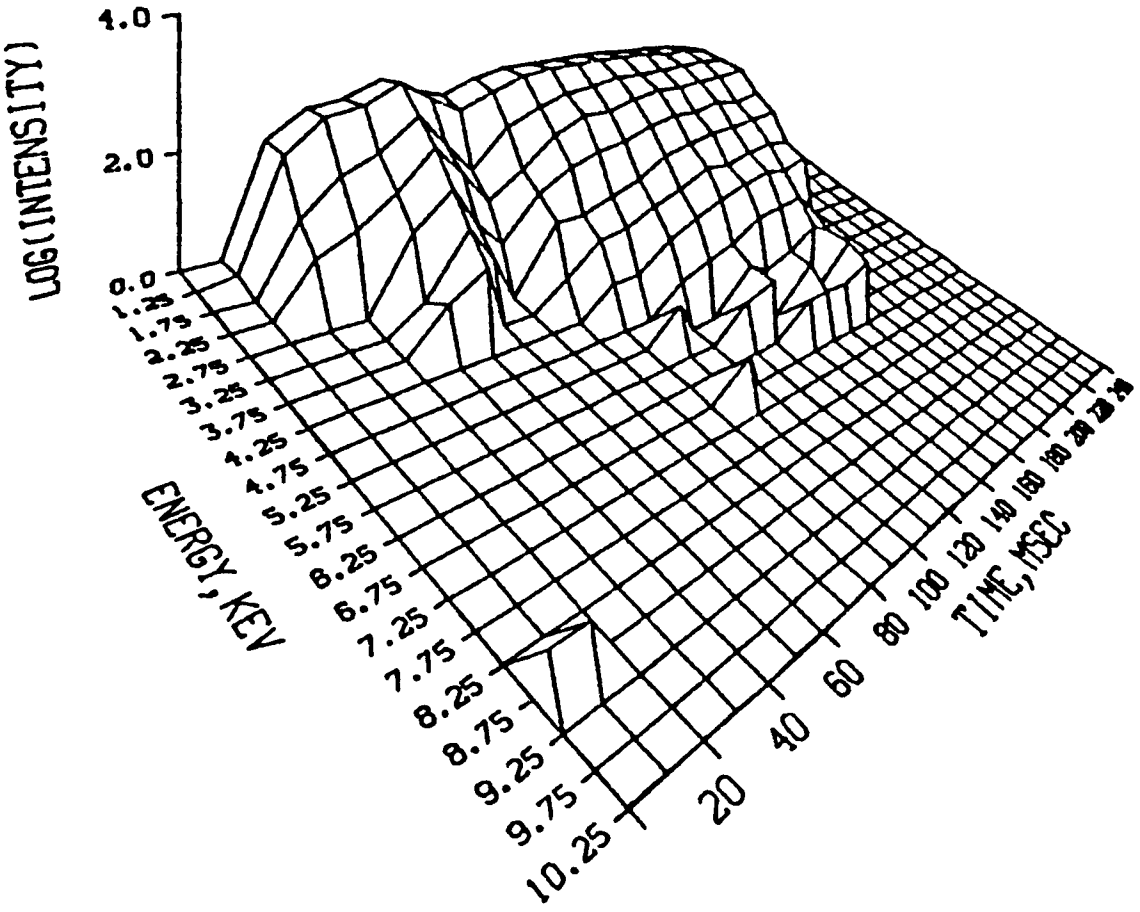

FIGURE 4-15. A three-axis plot of x-ray energy spectra vs time for a discharge in an ISX-B injection sequence

TABLE 4-5. Calculated x-ray data for an ISX-B discharge in a NBI sequence

LO	HI	TIME	TE	TE PEAK	COD	ERR	TOTCTS	ZEFF
2	4	25.	405.09	450.73	0.95	4.62	100.	3.28
2	4	35.	350.03	386.96	1.00	4.16	334.	6.00
2	7	45.	529.42	597.62	0.90	10.95	507.	3.64
2	7	55.	662.52	759.33	0.99	9.65	1235.	4.30
2	6	65.	533.92	603.02	0.98	8.67	449.	1.54
2	5	75.	433.28	483.69	0.95	7.10	199.	1.07
2	7	85.	592.63	673.84	0.95	10.74	452.	1.15
2	8	95.	595.74	677.62	0.98	12.09	854.	1.56
2	8	105.	570.97	647.61	0.96	11.73	1165.	2.03
3	9	115.	630.84	720.43	0.99	10.21	1299.	2.43
3	9	125.	702.24	808.48	0.98	9.77	1511.	3.01
4	11	135.	760.78	881.66	0.96	10.21	1672.	3.76
4	10	145.	698.19	803.45	0.91	8.56	1728.	4.58
4	12	155.	789.95	918.47	0.96	11.50	1787.	4.45
4	10	165.	902.08	1062.00	0.98	8.25	1863.	4.10
4	12	175.	831.12	970.78	0.94	11.31	1923.	4.22
2	8	185.	900.28	1059.66	0.91	12.84	230.	1.03

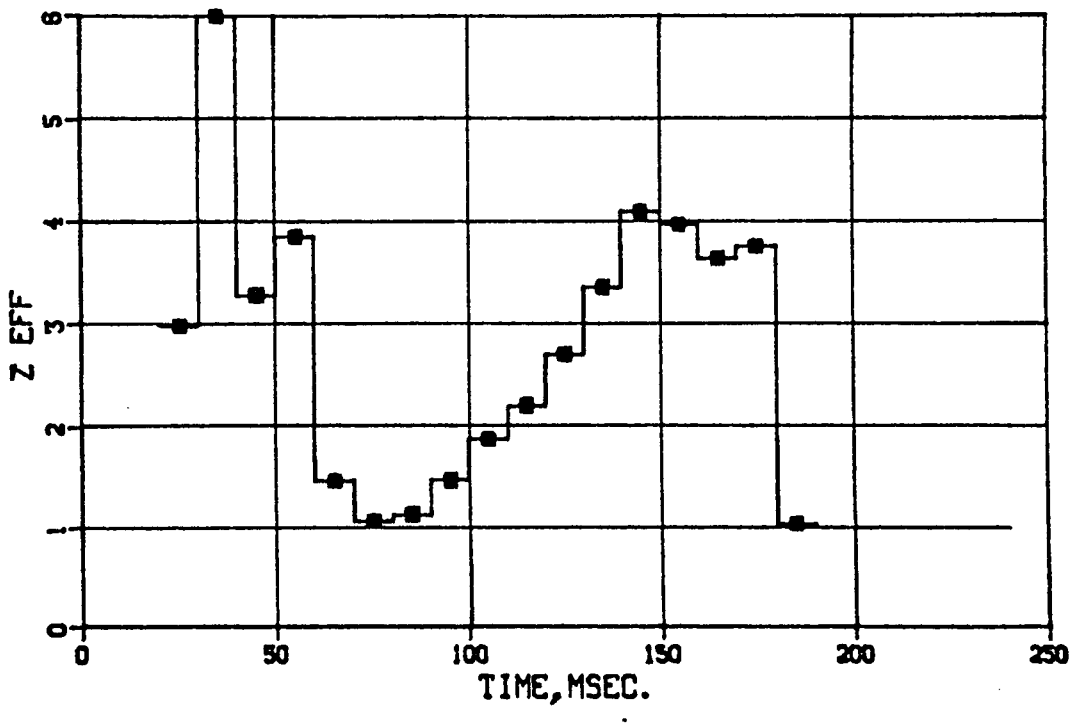

FIGURE 4-16. A plot of Z_{eff} vs time for a discharge in an ISX-B injection sequence

that new instability modes or other transient phenomena may appear, a diagnostic that can analyze a single discharge is especially valuable.

4.4.3 Behavior of Plasma Parameters During ECH

One alternative to neutral beam injection for supplying power to an established plasma is electron cyclotron heating,[63] a method in which radio-frequency power at the electron cyclotron resonant frequency

$$\omega_e = \frac{eB}{m} \qquad (4-4)$$

is applied to increase the total energy of the confined electrons. For ECH experiments on ISX-B, the power source was a gyrotron supplied by the Naval Research Laboratory, operating at ~35 GHz and a nominal 100 kW power level. Heating pulses lasted ~15 ms, and were applied at ~120 ms into the plasma discharge for the cases considered here.

X-ray data are available for eight discharges with ECH and five comparison discharges without ECH. These sequences are averaged to provide data for the three-axis plots shown in Figs. 4-17 and 4-18. Plots of T_e and N_e vs time for the two cases are shown in Figs. 4-19 and 4-20. A comparison of these figures does not show any obvious electron heating by the applied microwave power. Tables 4-6 and 4-7 list results of calculations for the two cases. Note that in each case, spectral linearity, statistics, and counting rate are all within reasonable bounds. In this example, x-ray and laser temperature

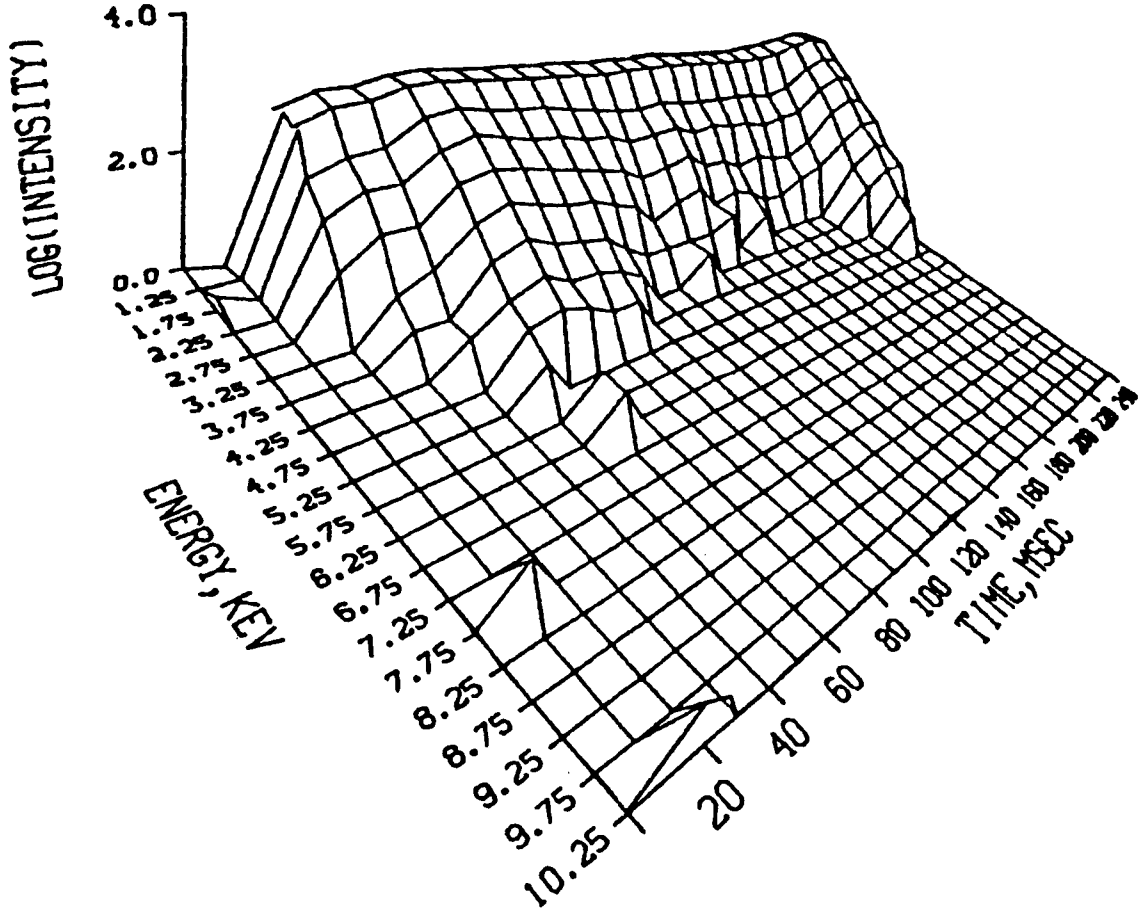

FIGURE 4-17. A three-axis plot of x-ray energy spectra vs time for an eight-discharge sequence with ECH

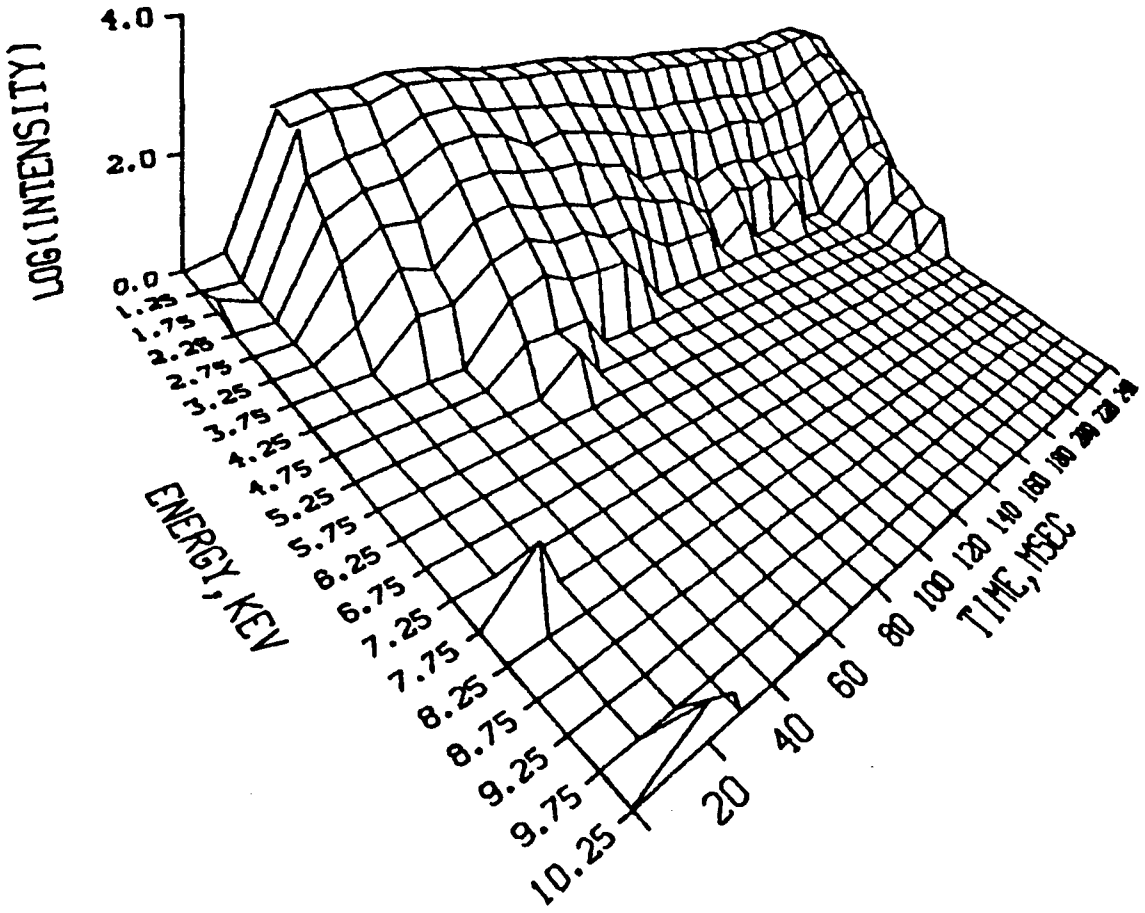

FIGURE 4-18. A three-axis plot of x-ray energy spectra vs time for a five-discharge sequence without ECH

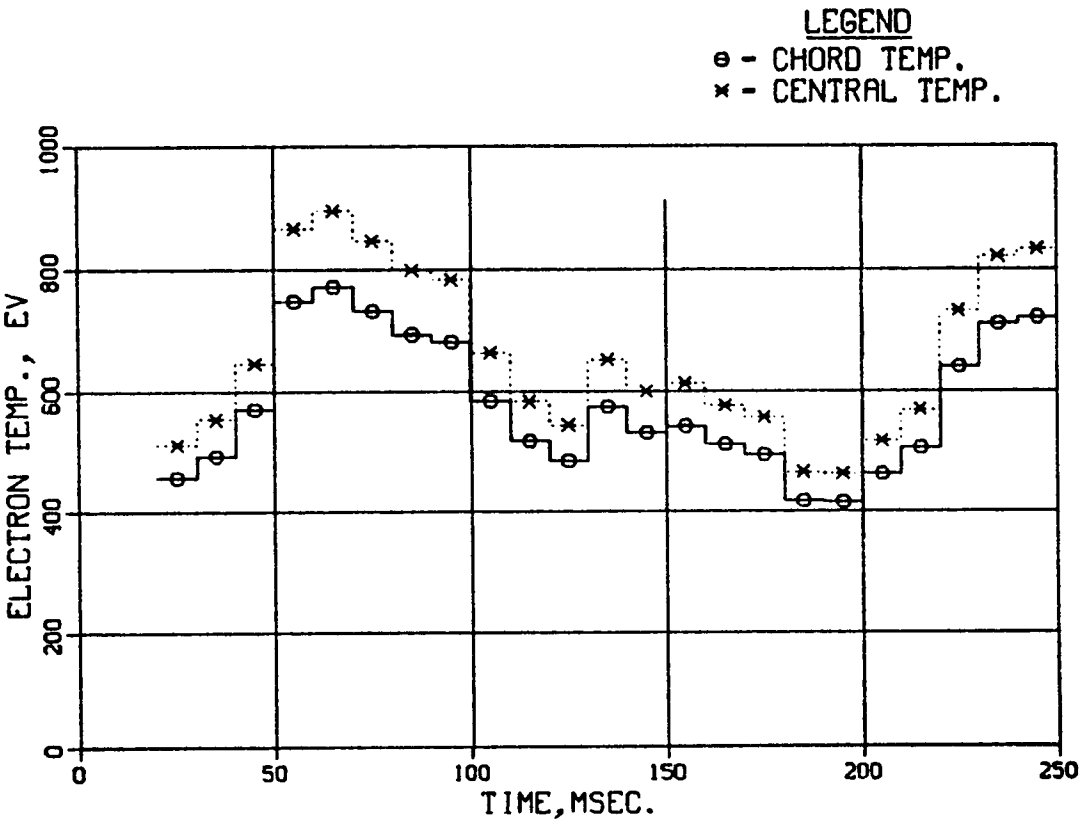

FIGURE 4-19. A plot of T_e vs time for an average of eight discharges with ECH

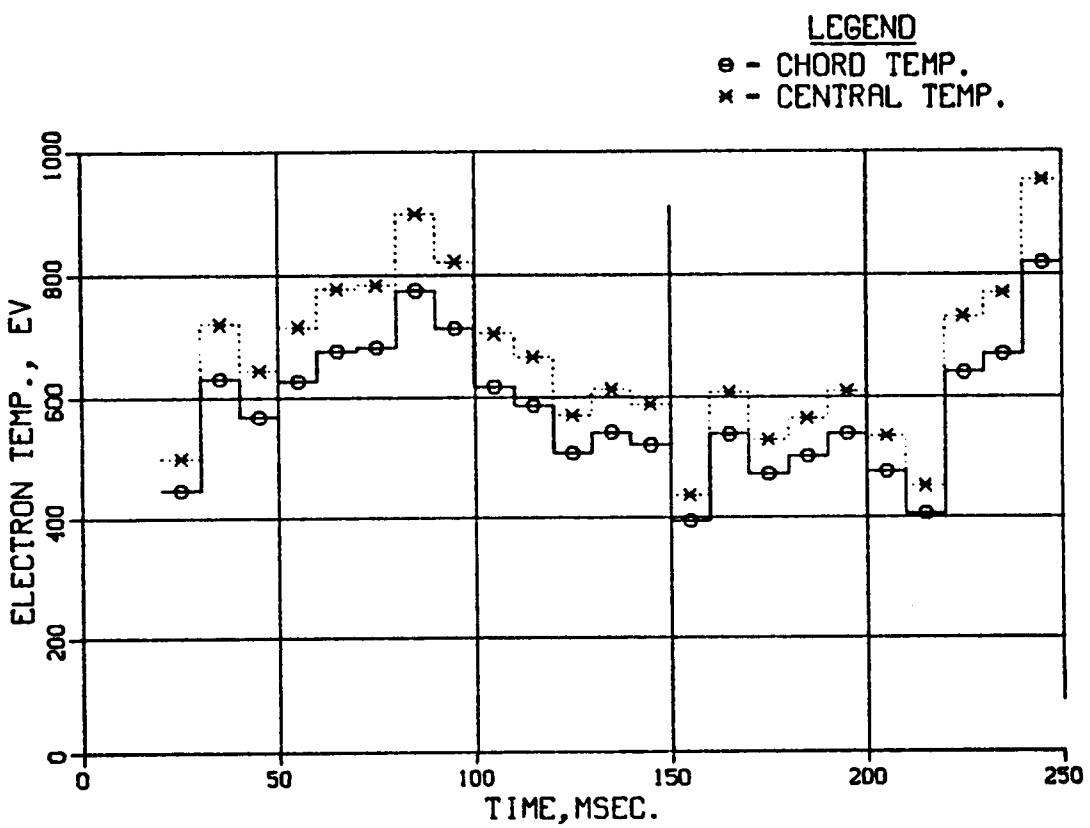

FIGURE 4-20. A plot of T_e vs time for an average of five discharges without ECH

TABLE 4-6. Calculated x-ray data for an average of eight discharges with ECH

LO	HI	TIME	TE	TE PEAK	COD	ERR	TOTCTS	ZEFF
2	5	25.	457.47	512.12	0.99	6.62	330.	0.00
2	7	35.	493.12	554.32	0.98	10.79	580.	0.00
2	8	45.	570.86	647.48	0.97	12.80	635.	0.00
2	10	55.	748.60	866.37	0.99	15.19	1203.	0.00
3	9	65.	771.28	894.89	0.99	9.88	1427.	0.00
2	9	75.	732.62	846.36	0.99	13.29	1189.	0.00
2	9	85.	694.80	799.25	0.99	13.60	1007.	0.00
2	9	95.	682.12	783.54	1.00	13.80	907.	0.00
2	8	105.	584.53	664.01	0.99	12.28	784.	0.00
2	7	115.	517.72	583.62	0.97	10.43	704.	0.00
2	7	125.	484.76	544.39	0.99	10.84	593.	0.00
2	8	135.	575.04	652.54	0.97	12.82	623.	0.00
2	7	145.	531.46	600.06	0.97	10.49	651.	0.00
2	7	155.	542.43	613.22	0.96	10.79	585.	0.00
2	6	165.	512.00	576.80	0.99	8.56	556.	0.00
2	7	175.	494.87	556.40	0.98	11.05	520.	0.00
2	6	185.	418.22	466.06	0.98	8.81	495.	0.00
2	6	195.	416.17	463.65	1.00	8.95	448.	0.00
2	6	205.	462.88	518.51	0.98	8.88	463.	0.00
2	6	215.	505.93	569.56	1.00	8.61	541.	0.00
2	8	225.	640.79	732.61	0.99	11.86	1005.	0.00
3	10	235.	712.02	820.65	1.00	11.82	1454.	0.00
2	9	245.	722.00	833.08	0.98	13.34	1113.	0.00

TABLE 4-7. Calculated x-ray data for an average of five dicharges without ECH

LO	HI	TIME	TE	TE PEAK	COD	ERR	TOTCTS	ZEFF
2	6	25.	447.31	500.16	0.99	9.01	364.	0.00
2	7	35.	630.80	720.38	0.99	10.43	575.	0.00
2	7	45.	568.67	644.84	0.99	10.45	629.	0.00
3	9	55.	627.37	716.18	0.99	10.32	1284.	0.00
3	10	65.	676.97	777.17	0.97	11.86	1386.	0.00
2	9	75.	682.78	784.35	0.99	13.45	1120.	0.00
2	8	85.	774.86	899.40	0.99	11.66	938.	0.00
2	8	95.	712.86	821.70	0.99	11.78	907.	0.00
2	8	105.	617.99	704.72	0.98	12.01	892.	0.00
2	7	115.	586.94	666.94	0.99	10.25	745.	0.00
2	7	125.	507.55	571.49	0.98	10.66	652.	0.00
2	7	135.	542.24	613.00	0.99	10.84	491.	0.00
2	7	145.	521.10	587.66	0.99	11.02	448.	0.00
2	6	155.	394.50	438.40	0.98	8.96	475.	0.00
2	7	165.	538.60	608.63	0.98	11.10	439.	0.00
2	6	175.	473.00	530.47	1.00	8.77	473.	0.00
2	6	185.	502.59	565.58	0.96	8.81	443.	0.00
2	7	195.	539.87	610.16	0.98	11.25	390.	0.00
2	6	205.	477.13	535.35	0.98	8.83	448.	0.00
2	6	215.	406.75	452.67	0.98	8.78	529.	0.00
2	8	225.	640.21	731.91	0.99	11.85	1008.	0.00
3	10	235.	670.92	769.69	0.97	11.87	1429.	0.00
2	11	245.	818.26	954.39	0.98	16.93	1101.	0.00

results do not agree. X-ray data show no evidence of electron heating at 120-140 ms, within experimental accuracy; laser data given in Fig. 4-21 shows a temperature increase of ~60%, from ~800 eV central T_e at 118 ms to ~1300 eV central T_e at 130 ms.

This is another case where diagnostic results are mixed. Thomson scattering and a second-harmonic cyclotron diagnostic register a significant rise in T_e during ECH.[64] Optical spectrometry results are not easily interpreted for this experiment but show no evidence of significant heating.[65] Loop-voltage measurements appear to be ambiguous, showing no clear, consistent dip during ECH, but yielding somewhat lower values for the ECH sequence than for the comparison discharges. Calculated Z_{eff} from resistivity measurements is approximately constant during ECH, at Z_{eff} ~4. This value agrees well with x-ray Z_{eff} results for a typical ECH discharge, plotted in Fig. 4-22.

In summary, the ECH experiment provides an example where conclusions based on x-ray and on laser data do not agree; x-ray data indicate no significant electron heating due to ECH. However, temperature measurements in the absence of ECH are in good agreement for the two techniques, and Z_{eff} values also match well. In view of the controversial results obtained by other diagnostics, it seems safe to conclude that this interesting experiment is not well understood and needs further study.

ORNL-DWG 79-3473R FED

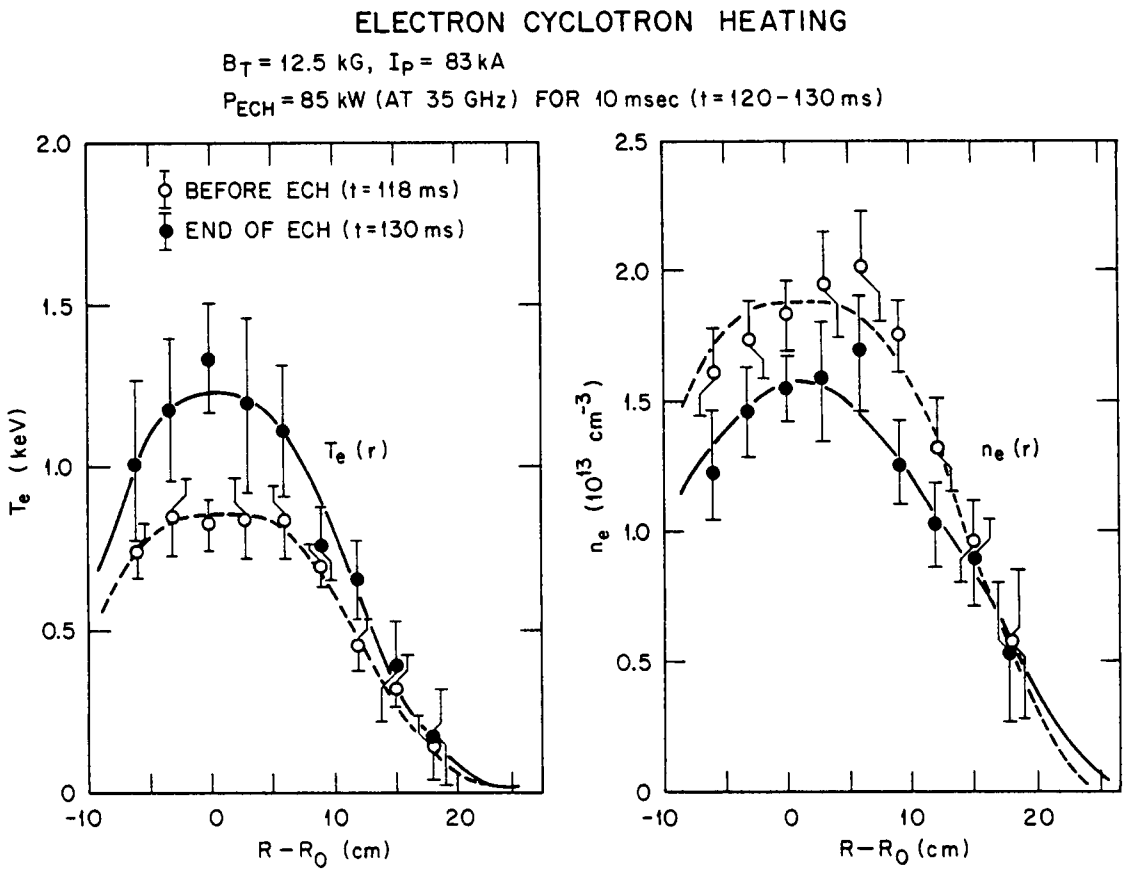

FIGURE 4-21. Plots of laser-derived T_e and N_e profiles for an ECH sequence on ISX-B

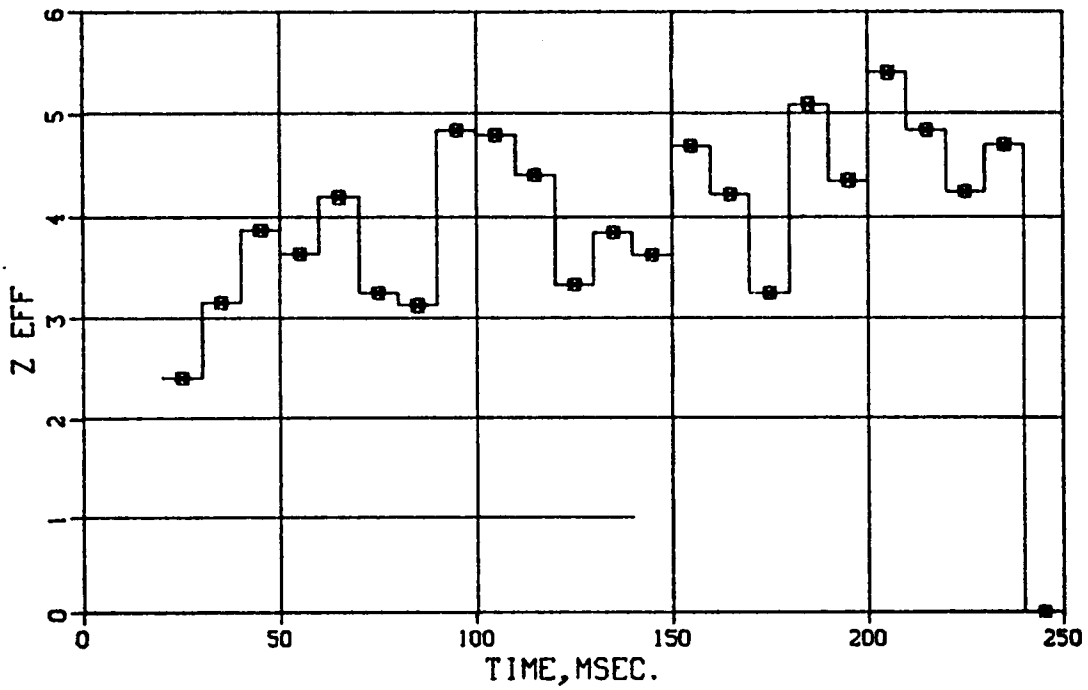

FIGURE 4-22. A plot of Z_{eff} vs time for a discharge in the ECH sequence

CHAPTER 5

SUMMARY AND CONCLUSIONS

5.1 INTRODUCTION

The objective of this research was to accomplish time-resolved measurements of T_e and Z_{eff} throughout a single plasma discharge in the Oak Ridge tokamak. The x-ray data necessary for these measurements would also provide a qualitative evaluation of plasma conditions by revealing line radiation or nonthermal spectral distributions. To meet this objective, the equipment required for data acquisition was developed and tested. The theoretical problems of extracting T_e and Z_{eff} from chord-integral spectra were carefully considered, and the effects of plasma model variations and instrumental errors on the accuracy of analytical results were evaluated. The computational procedure derived from this study was appraised by comparing the results of x-ray analysis for several distinct experimental cases with those from Thomson-scattering data. Several conclusions can be drawn from this research.

5.2 CONCLUSIONS FROM THEORETICAL CALCULATIONS

A careful consideration of the theory of x-ray emission from an impure plasma in a cylindrical geometry reveals that the T_e value derived from a chord-integrated spectrum is significantly lower than the central T_e, due to profile effects and the variation of impurity radiation enhancement with temperature. The quantitative effect is mainly a function of central temperature; impurity content and the explicit form of the models employed add second-order corrections.

The major effect of impurity species is an enhancement of the observed radiation intensity over what would be expected from a hydrogen plasma with equivalent $T_e(r)$ and $N_e(r)$. For a given impurity species, the enhancement is a function of T_e and concentration; the specific form of the plasma model only slightly affects the calculated enhancement. Thus, for known enhancement and T_e, Z_{eff} can be found.

A survey of possible error sources and an evaluation of their effects on the accuracy of T_e and Z_{eff} derivations shows that pulse pileup affects the data distribution most seriously. This error can be minimized by simply excluding distorted low-energy data from T_e calculations, and correcting for the loss in recorded count rate in Z_{eff} determinations. Statistical parameters (COD and SD) evaluated during the computations provide a check on the validity of the data.

5.3 CONCLUSIONS FROM EXPERIMENTAL DATA

The computational procedure derived from theory has been evaluated by applying it to a variety of experimental cases. Results of the x-ray derivations have been compared with those from Thomson-scattering measurements and resistivity calculations. These comparisons provide a check at one or two times during the discharge cycle. In most cases, agreement between the results is good. For the cases where agreement is poor (Z_{eff} behavior during NBI into a high-β plasma, and T_e behavior during ECH), there are conflicting results from other diagnostics as well. These cases need further study, and the time-resolved x-ray results should prove helpful in clarifying the processes involved. For on-line diagnosis of well-behaved plasmas,

the x-ray data supplements laser measurements, providing T_e and Z_{eff} time histories for individual discharges.

5.4 CAVEATS

The theoretical derivation of the computational procedure for x-ray data assumes that the plasma is Maxwellian, that no line radiation is present in the x-ray spectra, and that oxygen is the dominant impurity and is distributed as a uniform percentage of the total plasma. Where these assumptions are not valid, x-ray data may not provide correct results. The three-axis data display is a valuable aid in checking for nonthermal spectral components and line radiation. Extreme errors from excessive count rate and severe spectral distortion are prevented by limits on COD and total spectral counts.

5.5 ADVANTAGES

X-ray energy analysis offers several unique advantages as a plasma diagnostic. Since it analyzes radiation emitted in the normal course of tokamak operation, it does not perturb the experiment. (This may not be true for diagnostics which inject probes, beams, high-energy electromagnetic pulses, etc., into the plasma.) The equipment is relatively simple and requires no routine maintenance except for replenishing the liquid nitrogen in the detector dewar. Its calibration is easily checked, and it provides an independent determination of T_e. The technique can be extrapolated to reactor-grade plasma conditions. With computer data processing, it

provides an on-line diagnostic, measuring T_e and Z_{eff} discharge by discharge.

In summary, the favorable comparison of x-ray T_e and Z_{eff} derivations with accepted results inspires confidence in the x-ray technique and confirms the computational procedure. In cases where agreement is not good, the x-ray data provides additional information on conditions which merit further study. In all cases, the unique combination of time-resolved T_e and Z_{eff} measurements throughout a single tokamak discharge makes the x-ray energy spectrometer a valuable addition to the repertoire of tokamak plasma diagnostics.

LIST OF REFERENCES

LIST OF REFERENCES

1. Artsimovich, L. A., Nucl. Fusion 2 (1972) 215.

2. Furth, H. P., Nucl. Fusion 15 (1975) 487.

3. Rose, D. J. and Clark, M. Plasmas and Controlled Fusion, John Wiley and Sons, New York (1961) 228-255.

4. Arzimovich, L. A., Elementary Plasma Physics, Blaisdell Publishing Company, New York (1965) 81-89.

5. Boyer, K., Little, E. M., Quinn, W. E., Sawyer, G. A., and Stratton, T. F., Phys. Rev. Lett. 2 (1959) 279.

6. Greim, H. R., Kolb, A. C., and Faust, W. R. Phys. Rev. Lett. 2 (1959) 281.

7. Post, R. F., Bull. APS 23 (1978) 781.

8. Boyer, K., Little, E. M., Quinn, W. E., Sawyer, G. A. and Stratton, T. F. Phys. Rev. Lett. 2 (1959) 279.

9. Gerber, K. A. and Logan, B. G., "Filter and Film Method of Measuring the Temperature of a Hot, Dense, Low-Z Plasma from its Quantum Bremsstrahlung," NRL Report 7775 (1974).

10. Jahoda, F. C., Little, E. M., Quinn, W. E., Sawyer, G. A., and Stratton, T. F., Phys. Rev. 119 (1960) 843.

11. Robouch, B. V. and Rager, J. P., J. Appl. Phys. 44 (1973) 1527.

12. Bearden, A. J., Ribe, F. L., Sawyer, G. A., and Stratton, T. F., Phys. Rev. Lett. 6 (1961) 257.

13. Hill, K. W., private communication.

14. ORTEC, Inc., Oak Ridge, Tennessee, 1969 Catalog.

15. Silver, Eric, private communication.

16. Molvig, Kim, private communication.

17. Blanc, P., Brouquet, P., and Uhre, N. "Soft X-ray Spectrometry at High Count Rates," EURATOM-CEA Report EUR-CEA-FC-962 (1978).

18. Jahns, Gary, private communication.

19. Wing, W. R., private communication.

20. Gedcke, D. A., Elad, E., and Dyer, G. R., "Limitations on Si(Li) X-ray Energy Analysis Systems at High Counting Rates," (Proc. 6th National Conf. on Electron Probe Analysis, Pittsburgh, PA, 1971)

21. Lochte-Holtgreven, W., ed., Plasma Diagnostics, North Holland Publishing Co., Amsterdam (1968) 428.

22. Jackson, J. D., Classical Electrodynamics, John Wiley and Sons, New York (1967) 411.

23. Artsimovich, L. A., Nucl. Fusion 2 (1972) 229.

24. England, A. C., Mihalczo, J. T., Dyer, G. R., and Pearce, J. W., "Diamagnetic Measurements," Fusion Energy Division Annual Progress Report for Period Ending December 31, 1977, ORNL-5405 (1978) 59.

25. Arzimovich, L. A., Elementary Plasma Physics, Blaisdell Publishing Co., New York (1965) 123-125.

26. Cambel, A. B., Plasma Physics and Magnetofluid-Mechanics, McGraw-Hill, New York (1963) 61.

27. Engelmann, F. and Curatoto, M., Nucl. Fusion 13 (1973) 497.

28. Stauffer, F. J. and Boyd, D. A., Infrared Physics 48 (1978) 755.

29. Lochte-Holtgreven, W., ed., Plasma Diagnostics, North Holland Publishing Co., Amsterdam (1968) 560.

30. Dyer, G. R. and Murakami, M., "A Low-Noise Data Collection System for the Thomson Scattering Diagnostic Apparatus on ORMAK" (Proc. 5th Symp. on Eng. Probl. of Fus. Res., Princeton, NJ, 1977) IEEE 73CH0843-3-NPS (1977) 403.

31. Elwert, G, Z. Naturforschg. 9a (1954) 641.

32. Post, R. F., "Impurity Radiation Losses from a High Temperature Plasma," RISO Report No. 18.

33. Status and Objectives of Tokamak Systems for Fusion Research, WASH-1295 (1974) 18.

34. Spitzer, L. and Härm, R., Phys. Rev. 89 (1953) 977.

35. Berry, L. A. et al., in "Plasma Physics and Controlled Nuclear Fusion Research" (Proc. 6th Int. Conf., Berchtesgaden, 1976) 1 (1977) 49.

36. Rome, J. A., private communication.

37. Kramers, H. A., Phil. Mag. 46 (1923) 836.

38. Gaunt, J. A., Phil. Trans. Roy. Soc. London A229 (1930) 163.

39. Elwert, G., Z. Naturforschg. 9a (1954) 641.

40. Stratton, T. F., "Plasma Temperatures by Spectroscopy in the x-ray Region" in Herzfeld, C. M., ed., Temperature, Its Measurement and Control in Science and Industry, Vol. 3, Part 1, Reinhold Publishing Corp., New York (1962) 665.

41. Draper, N. R. and Smith, H., Applied Regression Analysis, John Wiley and Sons, New York (1967) 6-35.

42. von Goeler, S., Stodiek, W., Eubank, H., Fishman, H., Grebenshchikov, S., and Hinnov, E., Nucl. Fusion 15 (1975) 301.

43. McWhirter, R., Proc. Phys. Soc. (London) 75 (1960) 520.

44. Stratton, T. F., "Plasma Temperatures by Spectroscopy in the x-ray Region" in Herzfeld, C. M., ed., Temperature, Its Measurement and Control in Science and Industry, Vol. 3, Part 1, Reinhold Publishing Corp., New York (1962) 665.

45. von Goeler, S., Stodiek, W., Eubank, H., Fishman, H., Grebenshchikov, S., and Hinnov, E., Nucl. Fusion 15 (1975) 301.

46. Isler, R. C. and Crume, E. C., Jr., Phys. Rev. Lett 41 (1978) 1297.

47. Crume, E. C., Jr., "A Simple Numerical Model for Steady-State Impurity Recycling," Fusion Energy Division, Theory Section Memo No. 77/98 (1977).

48. Dyer, G. R., Neilson, G. H., and Kelley, G. G., Nucl. Instrum. Methods 161 (1979) 365.

49. Instruction Manual for 7000 Series Si(Li) X-ray Detector, ORTEC, Inc., Oak Ridge, Tennessee (1971) p. 9.

50. Gedcke, Dale (ORTEC), private communication.

51. von Mises, R., Mathematical Theory of Probability and Statistics, Academic Press, New York (1964) 130-133.

52. Simon, A., An Introduction to Thermonuclear Research, Pergamon Press, New York (1959) 17.

53. Kramers, H. A., Phil. Mag. 46 (1923) 836.

54. Karzas, W. J. and Latter, R., Rand-Corporation Research Memorandum RM-2010-AEC (1957).

55. Karzas, W. J. and Latter, R., Astrophys. J. Supplement 51 (1961) 167.

56. Spiegel, M. R., Theory and Problems of Statistics, Schaum Publishing Co., New York (1961) 241-247.

57. Draper, N. R. and Smith, H., Applied Regression Analysis, John Wiley and Sons, New York (1967) 6-35.

58. Berry, L. A. et al., "Electron Heating Experiments," in Fusion Energy Division Annual Progress Report for 1976, ORNL-5275 (1977) 25-32.

59. Murakami, M., Isler, R. C., Lyon, J. F., Bush, C. E., Berry, L. A., Dunlap, J. L., Dyer, G. R., Edmonds, P. H., King, P. W., and McNeill, D. H., Phys. Rev. Lett. 39 (1977) 615.

60. Edmonds, P. H., private communication.

61. Dunlap, J. L., private communication.

62. Isler, R. C., seminar.

63. Dandl, R. A. et al., Phys. Fluids 9 (1966) 1498.

64. Murakami, M., private communication.

65. Isler, R. C., private communication.

66. Goulding, F. S., Walton, J., and Malone, D. F., Nucl. Instrum. Methods 71 (1969) 273.

67. Kandiah, K. and Sterling, A., "A Direct-Coupled Pulse Amplifying System for Nuclear-Particle Spectroscopy" in Semiconductor Nuclear-Particle Detectors and Circuits, National Academy of Sciences, Publication 15943 (1969) 495.

68. Landis, D. A., Goulding, F. S., and Jaklevic, J. M., Nucl. Instrum. Methods 87 (1970) 211.

69. Goulding, F. S. and Stone, Y., Science 170 (1970) 280.

70. Fairstein, E. and Hahn, J., Nucleonics 23 (1965) 50.

71. Milam, Kelley and Karlovac, Nevin, (ORTEC, Inc.), private communication.

72. Wilkinson, P., Proc. Cambridge Philos. Mag. 46 (1950) 508.

73. Francis, J., Bell, P. R., and Gundlach, J., Rev. Sci. Instrum. 22 (1951) 133.

74. Heath, R. L., "The Application of High-Resolution Solid State detectors to X-ray Spectrometry - A Review" in Heinrich, K. ed., Advances in X-ray Analysis, Vol. 15, Plenum Press, New York (1972) 1-35.

75. Drude, Paul, The Theory of Optics, Dover Publications, New York (1959) 77-79.

76. Dyer, G. R., Neilson, G. H., and Kelley, G. G., Nucl. Instrum. Methods 161 (1979) 365.

77. Rozen, S., Nucl. Instrum. Methods 11 (1961) 316.

78. Heath, R. L. and Johnson, L. O., IEEE-TNS 16 (1969) 58.

79. Lochte-Holtgreven, W. ed., Plasma Diagnostics, North Holland Publishing Co., Amsterdam (1968) 41-42.

80. Melissinos, A. C., Experiments in Modern Physics, Academic Press, New York (1966) 438-453.

APPENDICES

APPENDIX A

ENERGY ANALYZER SYSTEM

A.1 INTRODUCTION

The success of an experiment designed to provide time-resolved data by energy spectrometry depends on the performance of the x-ray detector and associated pulse-processing electronics. Some essential system characteristics include adequate energy resolution, freedom from jamming due to high count rates or overload pulses caused by high-energy radiation, reliable unattended operation, and low system deadtime. Ease of energy calibration and good long-term stability are also important. Because of the large amount of data that is produced, the spectrometer must interface with a data storage system and provide data in a form compatible with computer processing and reduction.

Since this spectrometer differs from commercially available high-resolution systems in several areas of design philosophy and technique, the system components will be described in some detail. The compromises in energy resolution and count rate which affect the interpretation of the data will be discussed, along with the mechanical arrangement of the detector in relation to the plasma. An understanding of the measuring method and its effect on a collected energy spectrum is essential to the data reduction which produces the T_e and Z_{eff} measurements discussed in Chapter 2.

A.2 ELECTRONIC SYSTEM

The spectrometer electronic system comprises a cryogenic x-ray detector and preamplifier, a linear pulse-shaping amplifier, a pulse processor for peak detection and tail-pileup rejection, a multichannel parallel pulse-height analyzer with buffered storage registers, and a data transfer interface to a PDP-8 computer. The organization of these components is shown in Fig. A-1. For convenience in checking the gain calibration, the system includes an oscilloscope display, but this is not used during normal data collection.

A.2.1 Detector

The x-ray detector is a commercially manufactured unit, ORTEC Model 7416, designed for use in the soft x-ray energy range. The detecting element is a lithium-compensated silicon diode 4 mm in diameter and 3 mm thick, mounted in a vacuum cryostat and cooled by liquid nitrogen. The cryostat x-ray window is 0.012-mm thick beryllium. The cryostat also encloses the first-stage transistor and feedback components of the preamplifier.

The energy range and efficiency of the spectrometer are determined by the detector. Absorption in the x-ray window, the thin gold electrode on the detector, and the partially active silicon just under the electrode determine the low-energy response of the system. Detector transparency limits the high-energy response. Over the 1-10 keV energy range of interest, the detector efficiency is essentially 100%. (See Chapter 3, Section 3.3 for further comments.)

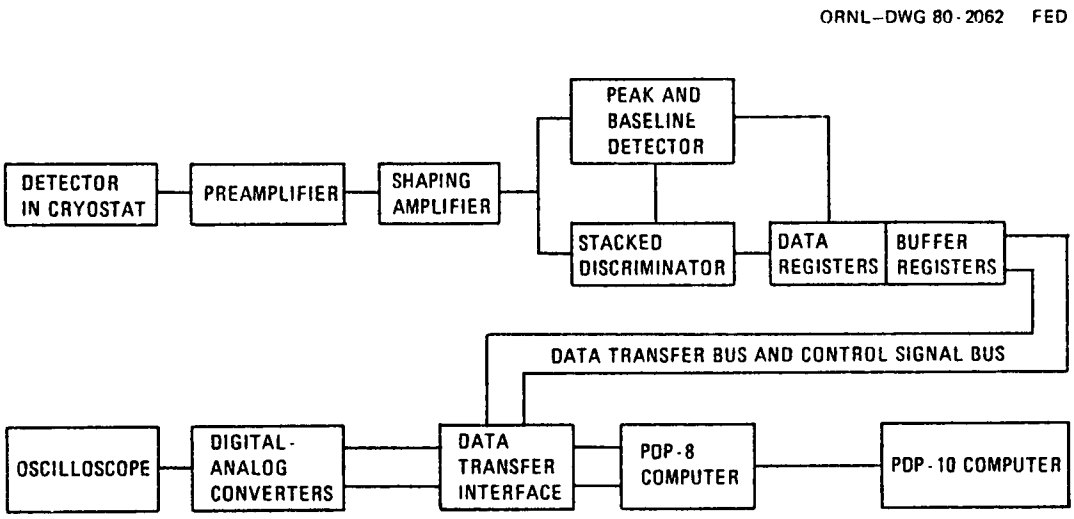

FIGURE A-1. A block diagram of the pulse-height analysis and data collection system for the x-ray energy spectrometer

A.2.2 Preamplifier

The charge-sensitive preamplifier was supplied with the detector, and is an ORTEC Model 117B. Since the spectrometer must count at rates of the order of 10^5 per second, the dynamic range of the preamplifer charge loop must be adequate. Dynamic range is a function of the feedback technique used in the charge loop, so the design of the charge-sensitive stage is an important factor in selecting a detector-preamplifier system.

In general, detector manufacturers use optical feedback[66] in the charge-sensitive stage. In this technique, a controlled light source induces a gate-to-channel leakage current in the first-stage FET; this leakage current is regulated to equal the mean current from the x-ray detector. This method has been remarkably successful in reducing electronic noise at low counting rates and thus improving system energy resoluton. However, it has several disadvantages at the high rates necessary for the present application. In practice, the light source is pulsed[67,68] to reset the charge loop output whenever it exceeds a preset level; the reset time varies between 10 and 100 μs, and can become the major fraction of the total counting time at high counting rates. Further, the reset operation introduces large signals of polarity opposite to the normal counting pulses into the following electronic stages, causing severe overloads unless sophisticated gating techniques are used to prevent them. Finally, the optical feedback scheme may not generate sufficient leakage current in a given FET to prevent charge-loop latchup during periods of rapid counting.

These considerations led to the selection of the old-fashioned resistive feedback method for the present system.

Figure A-2 shows the arrangement of the 117B preamplifier. The feedback resistor value was selected to provide a dynamic range of 10^6 counts/second of 5 keV photons, by the following procedure: one ion pair is produced in the detector for approximately 3.8 eV of deposited energy,[69] so a photon of 5 keV will produce 1300 ion pairs. At 10^6 photons per second, the average current from the detector is

$$\bar{I} = \frac{5000}{3.8} \times 10^6 \times 1.6 \times 10^{-19} \text{ coulombs/sec} \qquad \text{(A-1a)}$$

or

$$\bar{I} = 2.1 \times 10^{-10} \text{ amperes.} \qquad \text{(A-1b)}$$

The charge loop output v_o can rise to approximately 10 volts while maintaining linear operation; input voltage v_{in} at the FET gate is approximately zero, so the voltage across R_f is

$$v_o - v_{in} = 10 \text{ volts} \qquad \text{(A-2)}$$

The value of R_f is selected to supply the current $\bar{I}$ at the given charge-loop output:

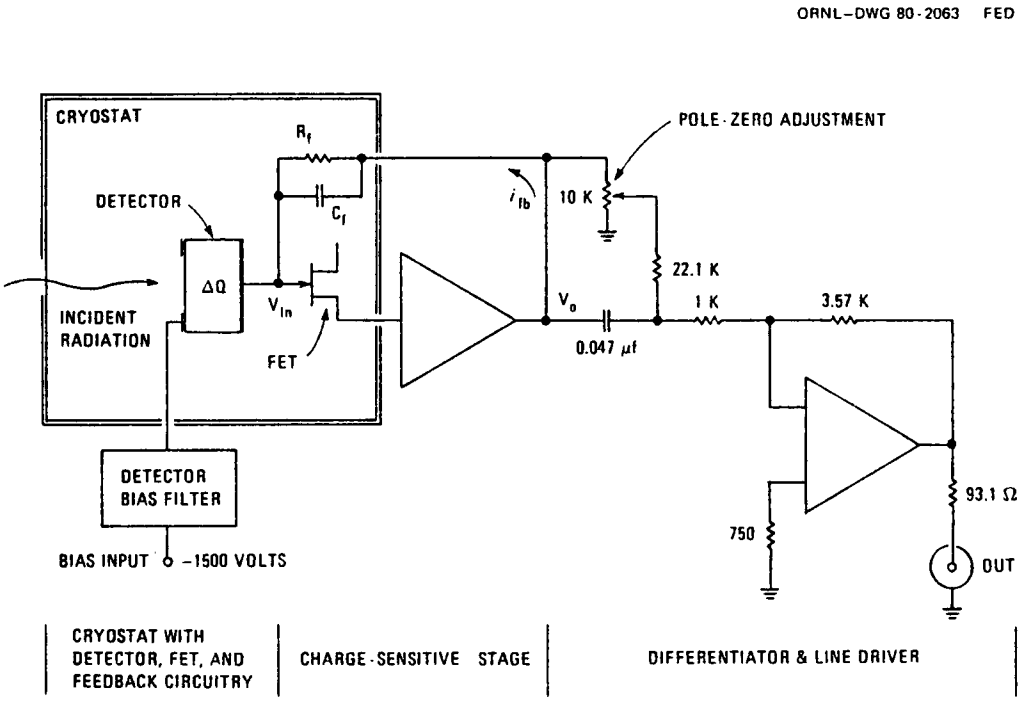

FIGURE A-2. A block diagram of the lithium-drifted silicon x-ray detector and preamplifier

$$R_f \simeq \frac{10 \text{ volts}}{2.1 \times 10^{-10} \text{ amperes}} \simeq 5 \times 10^{10} \text{ ohms} \qquad \text{(A-3)}$$

The manufacturer was requested to install a resistor which would not exceed this value. Measurements of charge-loop output voltage made at high counting rates confirm the dynamic range calculations.

As Fig. A-2 indicates, the preamplifier incorporates an active differentiator to shorten the output pulse from the charge-loop time constant of approximately 2 ms to the differentiator time constant of 47 μs. A pole-zero trim removes undershoot from the differentiator/line driver output pulse. The rise time of the line driver output pulse is approximately 150 ns.

A.2.3 Linear Amplifier

The linear amplifier is the component of the energy spectrometer which determines pulse width and provides a linear gain in pulse height to match the requirements of the pulse-height analyzer. In an energy spectrometer, each x-ray photon produces an electrical pulse; pulse height in volts is proportional to photon energy. Energy resolution of the spectrometer is limited by electronic noise, mostly originating in the preamplifier input circuitry. This noise appears as a fluctuation in the amplifier baseline voltage, and consequently as a fluctuation in pulse height for pulses with the same initial energy. The amount of preamplifier noise which passes through the linear amplifier is a function of the pulse rise time, which is

related to pulse duration. In general, narrower pulses from the linear amplifier imply a faster rise time, a broader bandwidth, and an increase in noise output, compared to wider pulses. Thus, energy resolution deteriorates as pulse width is decreased. On the other hand, narrower pulses imply a higher count rate acceptance, since more pulses can be crowded into a given time interval without overlapping. Clearly, some compromise between best energy resolution and highest count throughput is necessary. Table A-1 lists the energy resolution inherent in the linear amplifier output for various shaping times and corresponding pulse durations for the spectrometer under discussion. Both delay-line and resistive-capacitive shaping data are included. For all but the shortest time constant, energy resolution is better than 500 eV. Since total system energy resolution is 500 eV at best, limited by the pulse-height analyzer, a shaping time of at least 0.25 μs gives adequate energy resolution in the linear amplifier.

Most commercial linear amplifiers use R-C (resistive-capacitive) shaping circuits to determine pulse width. A single R-C differentiator and several stages of R-C integration are normally employed to provide a pulse shape which is approximately Gaussian, since this shape minimizes amplifier noise contributions.[70] The limited number of integrations practical in an amplifier (two to five is usual) causes the falling pulse edge to be longer than the leading edge by a factor of 1.5 or more, and since system noise (and energy resolution) is an inverse function of pulse rise time, R-C shaping does not provide the optimum pulse shape to minimize pileup.

TABLE A-1. Spectrometer energy resolution for various linear amplifier shaping times and pulse lengths

Shaping Method	Shaping Time (μs)	Pulse Length (μs)	Resolution (eV)
DL	0.1	0.4	500
RC	0.1	0.5	460
DL	0.25	1.0	433
RC	0.25	1.4	410
DL	0.5	2.0	315
RC	0.5	2.8	311
DL	1.0	4.0	264
RC	1.0	5.5	264

A pulse-shaping technique which more nearly equalizes pulse rise- and fall-times is delay-line shaping followed by R-C integration (only one or two stages is sufficient for pulse smoothing here). Figure A-3 illustrates the difference in pulse lengths produced by delay-line shaping with two integrations (top pulse) and R-C differentiation followed by active integration as used in an ORTEC 450 linear amplifier (bottom pulse), when each amplifier is adjusted for approximately equal rise time. Consultation with designers at ORTEC[71] confirmed the opinion that delay-line shaping offered superior performance in high-count-rate applications, but these experts believed no commercially available delay-line amplifier provided adequate base-line stability for the anticipated 10^5 per second count rate. Therefore, the amplifier shown schematically in Fig. A-4 was designed for the energy spectrometer.

The amplifier operates at a fixed time constant and fixed gain, following initial calibration. The pulse-amplifying chain consists of five operational stages. An input amplifier drives a shorted delay line to differentiate the input pulse. The differentiated pulse is amplified and integrated in two following stages, and the fourth stage provides for gain calibration. The fifth stage adds a second integration and serves as the pulse output amplifier. A sixth stage is not in the pulse-amplifying chain, but stabilizes the output baseline. Adjustments are provided to terminate the delay line precisely, to compensate for resistive losses along the delay line (this is analogous to pole-zero compensation in R-C circuitry, and eliminates baseline undershoot which would have the time constant of

ORNL-DWG 80-2077 FED

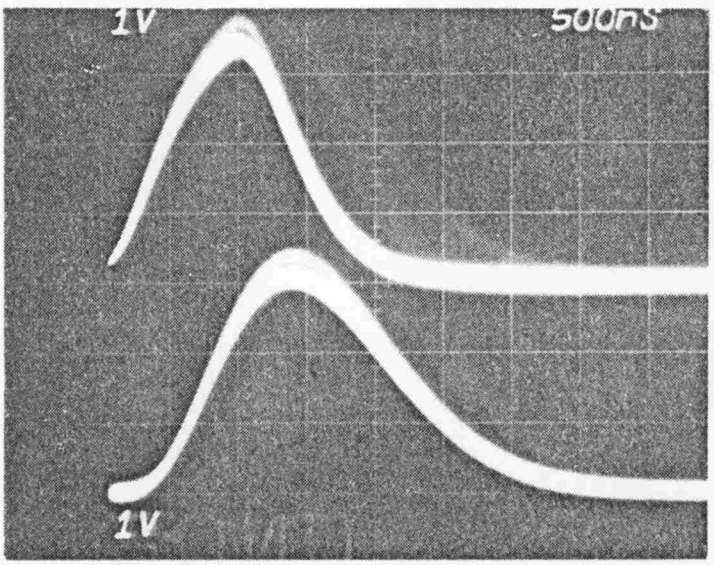

FIGURE A-3. A comparison of delay-line (top) and resistive-capacitive (bottom) amplifier pulses

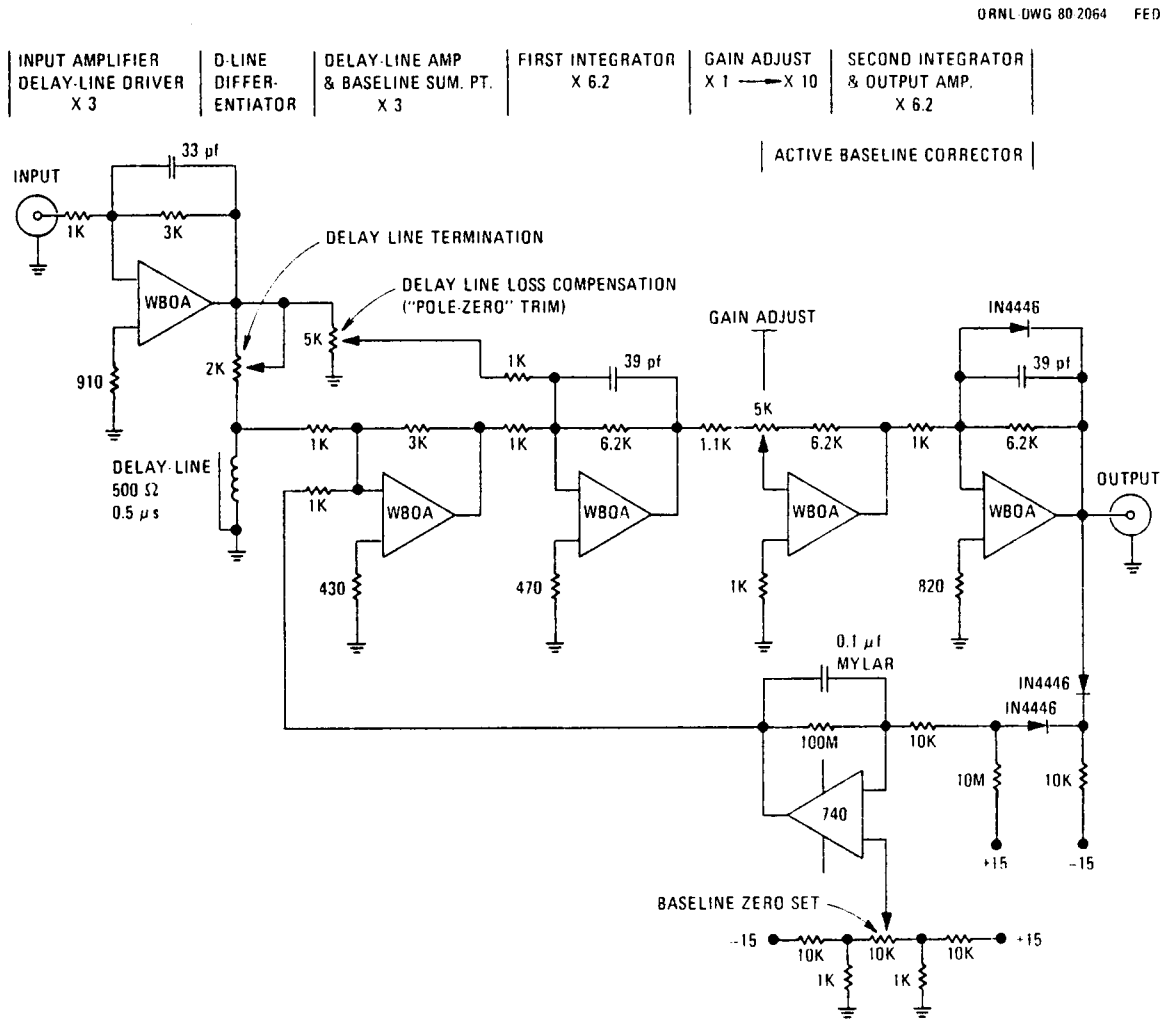

FIGURE A-4. A schematic diagram of the delay-line shaping amplifier used in the x-ray energy spectrometer

the input pulse), to adjust amplifier gain for energy calibration, and to set the output baseline at zero.

The five pulse-amplifying stages use the discrete-transistor operational amplifier circuit given in Fig. A-5. The nominal open-loop gain of this circuit with a load resistance of 10^3 ohms is approximately 70 db. At a closed-loop gain of 20 db, the frequency response extends from d.c. to approximately 50 MHz. Components are inexpensive (approximately $3.00 per amplifier) and readily available, and the circuit is easily stabilized for unity gain. With ± 15 volt supplies, the output voltage is linear to greater than ± 10 volts.

The baseline stabilizing circuit used in the linear amplifier is one of several designed and tested for this application. Its unique characteristic is that it samples the negative peaks of the amplifier baseline noise and corrects the amplifier output to keep the negative "edge" of the baseline at a constant reference point. Thus the baseline zero-set potentiometer is adjusted to a negative potential, with a value one-half the baseline noise width. This method stabilizes the baseline even at very high counting rates. (Most restorer circuits are effective only up to approximately 50% duty cycle of the output stage.)

Disadvantages associated with this circuit are that the baseline must be adjusted to zero for a given time constant and a specific gain. Further, the amplifier must be carefully adjusted to eliminate pulse undershoot due to improper delay line termination or compensation. Fulfilling these requirements presents no difficulty in the present application.

ORNL-DWG 80-2065 FED

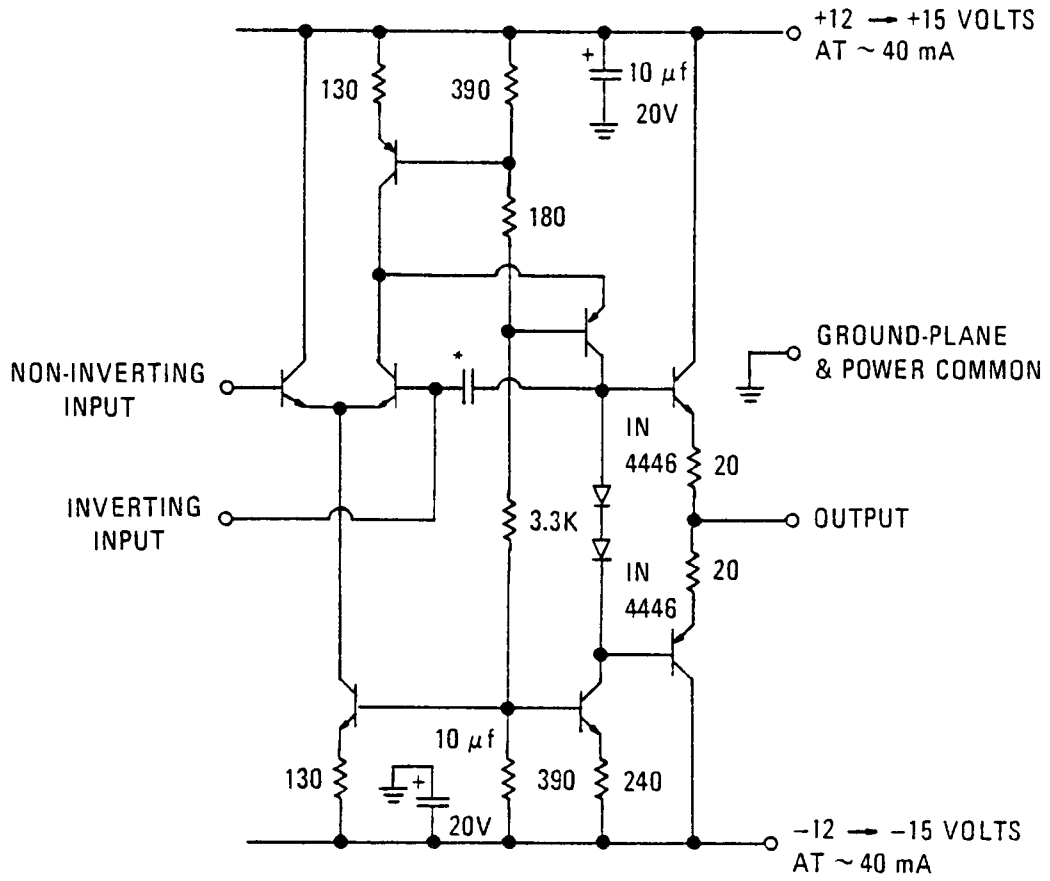

NPN TRANSISTORS –2N 2222 OR 2N 3904
PNP TRANSISTORS –2N 2907 OR 2N 3906
* – CAPACITOR ~ 1 → 5 pf AS NEEDED FOR STABILITY

FIGURE A-5. A schematic diagram of the discrete-transistor operational amplifier

The sequence of oscilloscope photographs in Fig. A-6 illustrates the stability of peak and baseline positions with increasing count rate, ranging from 5000 per second initially to 225,000 per second, measured with a digital counter at the linear amplifier output. The pulse peak has shifted slightly at the highest rate, but the system resolution is still good enough to distinguish the Mn Kβ x-ray at 6.4 keV from the more intense Kα peak at 5.9 keV. Long-term stability of the baseline is excellent, being essentially the input voltage drift of the monolithic amplifier used in the correcting integrator; no readjustment has been necessary during a year of continuous operation of the linear amplifier.

A.2.4 Stacked-Discriminator Pulse-Height Analyzer

Commercial pulse-height analyzers used for nuclear spectrometry normally use a circuit originated by Wilkinson[72] which measures the time for a linear ramp to rise from zero to the pulse height being measured. This technique is easily adapted to measure small increments in pulse height (or a large number of energy channels) with very good linearity. However, even very sophisticated versions of this circuit take a significant time interval (usually considerably longer than the pulse duration) to measure a single pulse height; this introduces a deadtime (the time the analyzer is busy with a measurement) which can be a large fraction of the total counting time. At count rates of 10^5 per second, the deadtime of a conventional pulse height analyzer approaches 100% of the counting time. For this reason, a parallel-analysis or "flash" analog-to-digital technique is used in the present spectrometer. The pulse height is analyzed within

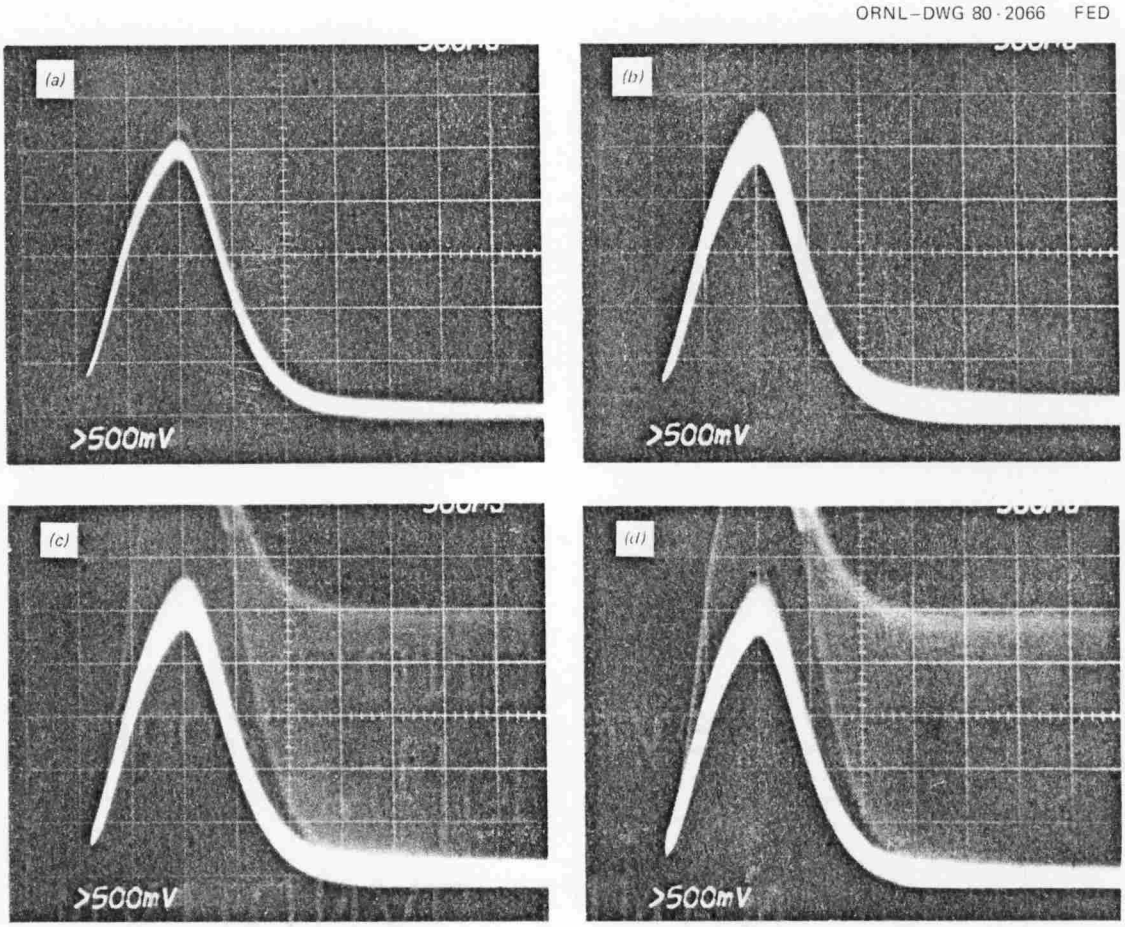

FIGURE A-6. Linear amplifier output for various counting rates: (a) 5000 c/s, (b) 50,000 c/s, (c) 150,000 c/s, (d) 225,000 c/s

the time duration of the pulse itself, so the analysis process contributes no deadtime of its own to that inherent in the linear-amplifier pulse width.

The stacked discriminator analyzer of Fig. A-7 revives a technique used by Bell and co-workers[73] at Oak Ridge National Laboratory during the early 1950's. The linear amplifier pulse is applied simultaneously to the inverting input of each of 20 fast voltage comparators. The noninverting inputs of successive comparators are biased progressively higher by a resistive voltage divider spanning the range from zero to the reference voltage (6.0 volts here). As a pulse rises in amplitude, successive latches are tripped until the pulse peak is reached; an arrangement of exclusive-OR gates detects the highest latch tripped in the stack of 20, and signals the respective memory register that a pulse falling within that channel has been processed. The fall-time of the pulse is available for data storage and latch-reset operations.

The pulse-height analyzer is calibrated to cover the 1-10 keV energy range by adjusting the linear amplifier gain. Energy calibration is done with an adjustable mercury-relay pulse generator, which is previously adjusted to agree with the 5.9 keV x ray from iron-55. The calibrated analyzer follows the formula

$$E_n = \frac{n}{2} + 0.25 \qquad \text{(A-4)}$$

where n is the channel number and E_n is the mean energy of channel n

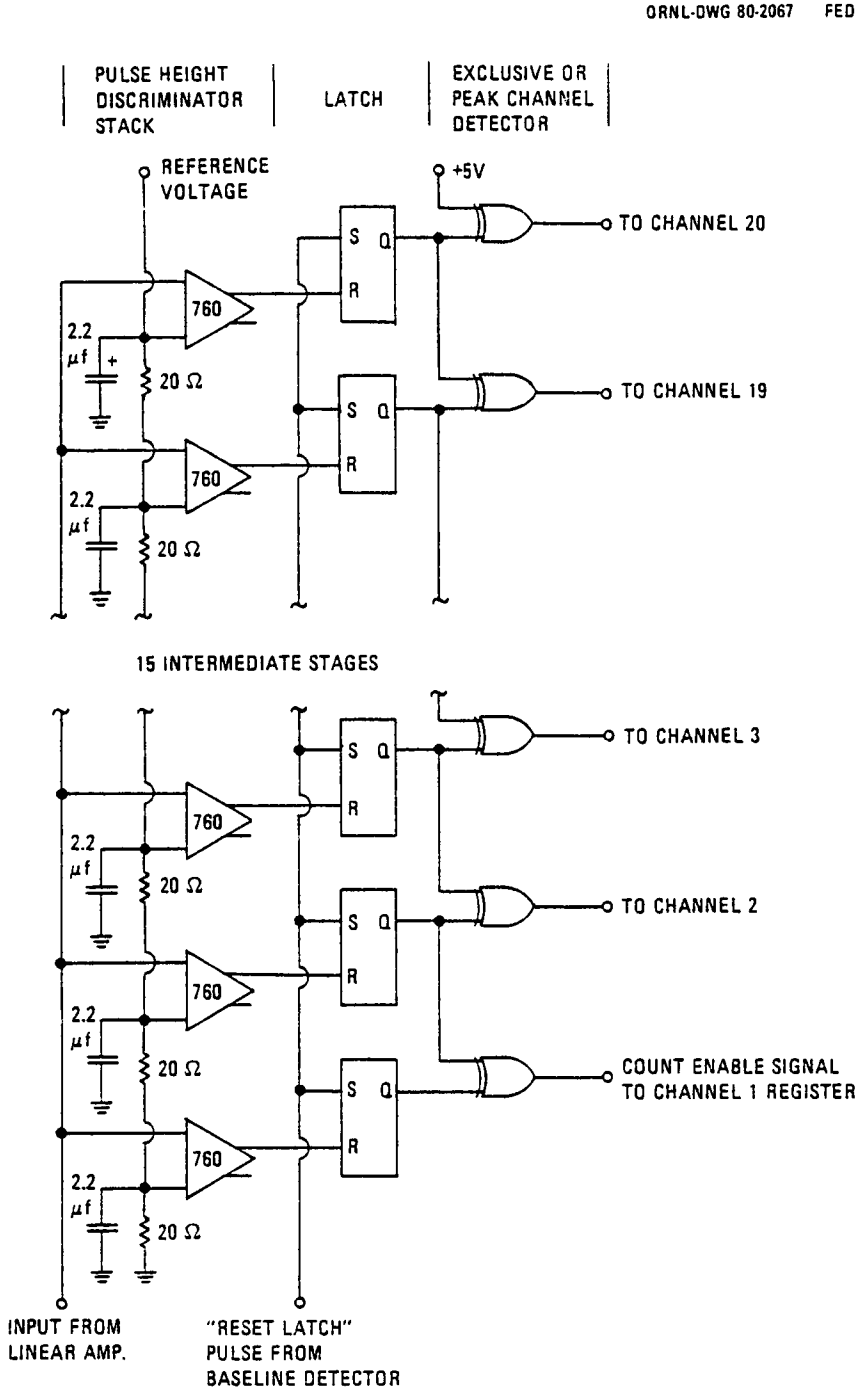

FIGURE A-7. A schematic diagram of the stacked-discriminator pulse-height analyzer

in keV. Thus, channel 1 is set to span the range 0.5 - 1.0 keV, with mean energy 0.75 keV. Note that channel 20 registers all pulses above the 6.0 volt reference level. This corresponds to all energies above 10 keV, so channel 20 records the total number of high-energy events detected.

A.2.5 Pulse Peak and Baseline Detector

Although the stacked discriminator automatically records the peak height of an input pulse, it does not detect the time of occurrence of the peak; additional circuitry is required to notify the memory registers that a pulse peak has occurred and must be counted in the proper channel. Figure A-8 includes the diagram for this function. The linear amplifier signal is inverted by a gain-of-one buffer and processed by an active differentiator. The differentiator output is positive for a rising signal from the linear amplifier, and negative for a falling signal; at the pulse peak, the differentiator output switches from a positive to a negative level, as shown in Fig. A-9. This positive-to-negative transition is detected by the following discriminator, which triggers a one-shot circuit to set an R-S flip-flop. This triggers a second one-shot which generates a "STORE DATA" pulse, signalling that a linear amplifier pulse peak has occurred and that the peak height latched into the stacked discriminator is to be counted in the proper memory register.

Once the peak has occurred, the pulse processor inspects the linear amplifier signal for a return to a low potential as set by the baseline threshold adjustment. At high counting rates, there is a probability that a second pulse will occur before the preceding pulse

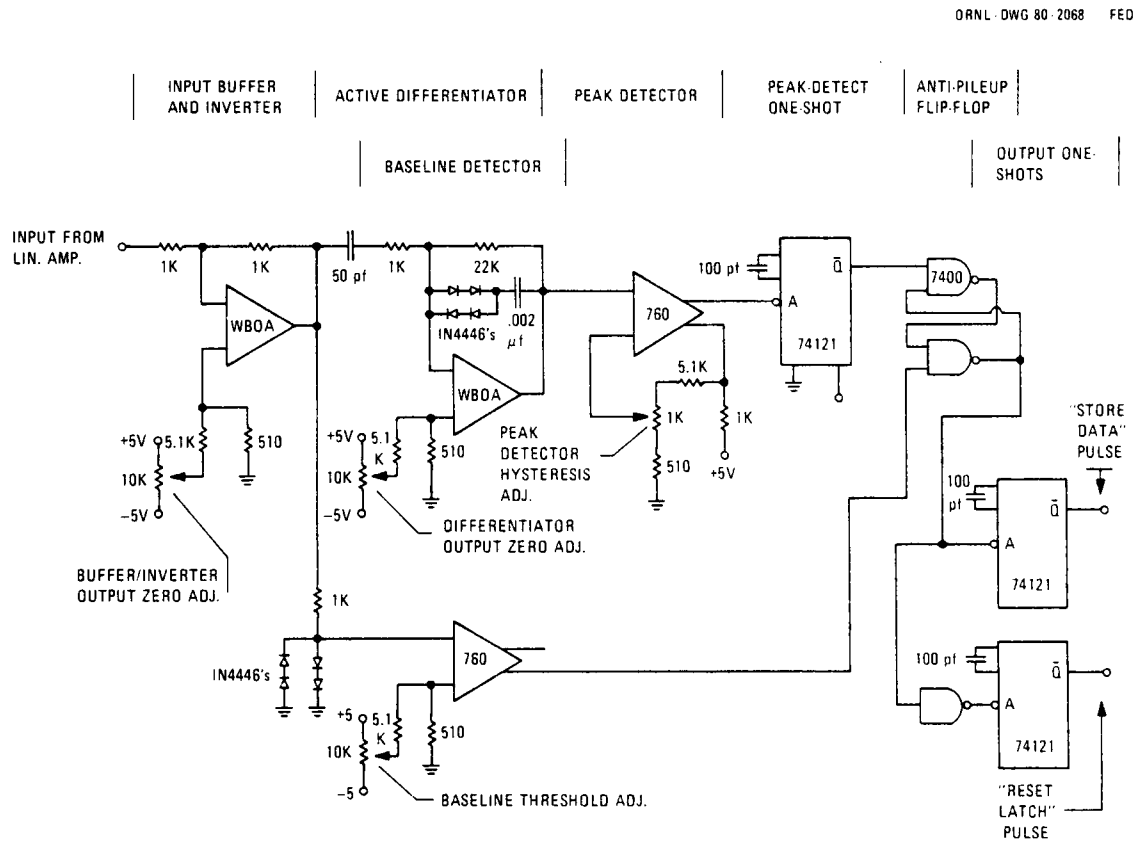

FIGURE A-8. A schematic diagram of the pulse peak- and baseline-detector and tail pileup rejector

ORNL-DWG 80-2157 FED

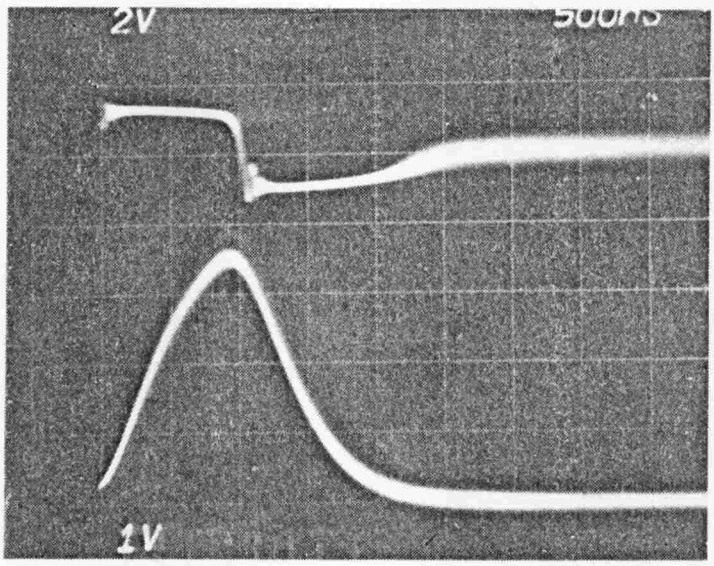

FIGURE A-9. Active differentiator (top) and linear amplifier (bottom) output waveforms

has fallen to the linear amplifier baseline potential. If this happens, the second pulse will "pile up" on the first, and the second pulse height will be too large. An analysis of this distorted pulse is prevented by the baseline detector, which does not reset the stacked discriminator latches or the anti-pileup flip-flop until the linear amplifier output falls to the baseline.

While this circuit rejects tail pileup pulses, it cannot detect pileup which occurs on the leading edge of an amplifier pulse. R. L. Heath[74] points out that leading-edge pileup rejection requires a fast inspection channel in addition to the signal channel. Since the preamplifier rise time (~150 nS) is comparable to the pulse rise time (~500 nS) of the linear amplifier, a leading-edge pileup rejection circuit was not judged worthwhile. Instead, some pileup was accepted as inevitable, and calculations to correct for its effects were undertaken (see Appendix B).

A.2.6 Data Registers

Multichannel analyzer data are stored in data registers arranged as shown in Fig. A-10. Each channel is furnished with a sixteen-bit memory. The coincidence of a true enable level from a discriminator-stack exclusive-OR gate and a "STORE DATA" pulse from the peak-height detector enters one count in the memory.

The DM7554 memory circuits used here incorporate a counting register, buffer register, and three-state (active UP, active DOWN, and open) output stage. This allows the memory to simultaneously collect data for a current energy spectrum and transfer data from the preceding spectrum to a mass data storage device. The buffer outputs

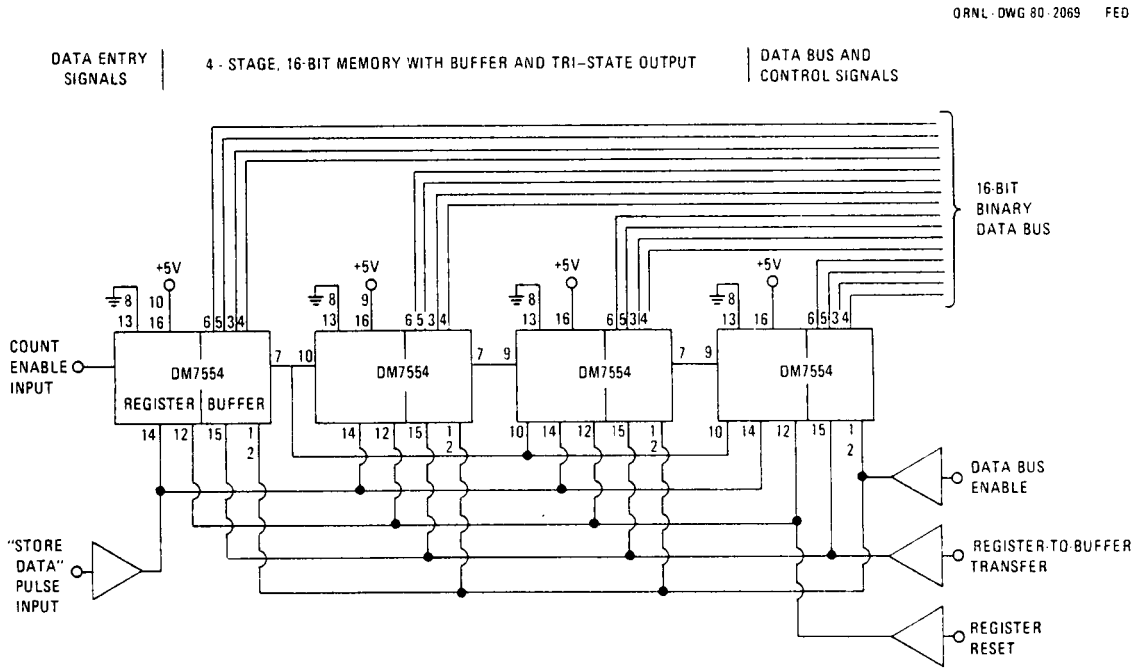

FIGURE A-10. A schematic diagram of the 16-bit buffered data register for one channel of the pulse-height analyzer

for all 20 channels are tied to a data bus which is controlled by a PDP-8 computer through a data transfer interface.

A.2.7 Pulse-Processing Sequence

The sequence of events in the pulse-height analysis process is illustrated in Fig. A-11. The linear amplifier pulse is input to the stacked discriminator and the peak and baseline detector. As the pulse rises, the baseline detector comparator trips; it does not reset until the linear amplifier signal falls below the baseline threshold. Successive stacked discriminators trip until the pulse peak occurs. The transition from rising to falling edge is signalled by the active differentiator, and the peak detector comparator initiates a "STORE DATA" pulse which stores one count in channel n of the multichannel memory. Any subsequent amplifier signals are ignored until the baseline detector resets and initiates a "RESET LATCH" pulse to the stacked-discriminator latches. This entire analysis sequence occurs within the time span of a single linear amplifier pulse.

A.2.8 Data Transfer Interface

Spectrometer data are taken under control of a PDP-8 computer during each tokamak discharge. The counting interval, data transfer to buffer registers, counting register reset, and data transfer from buffer to computer storage are all controlled through the circuitry depicted in Fig. A-12.

The timing sequence for data collection is as follows: a pulse from the tokamak control room signals the computer that a plasma discharge is beginning. The computer sends a register-to-buffer

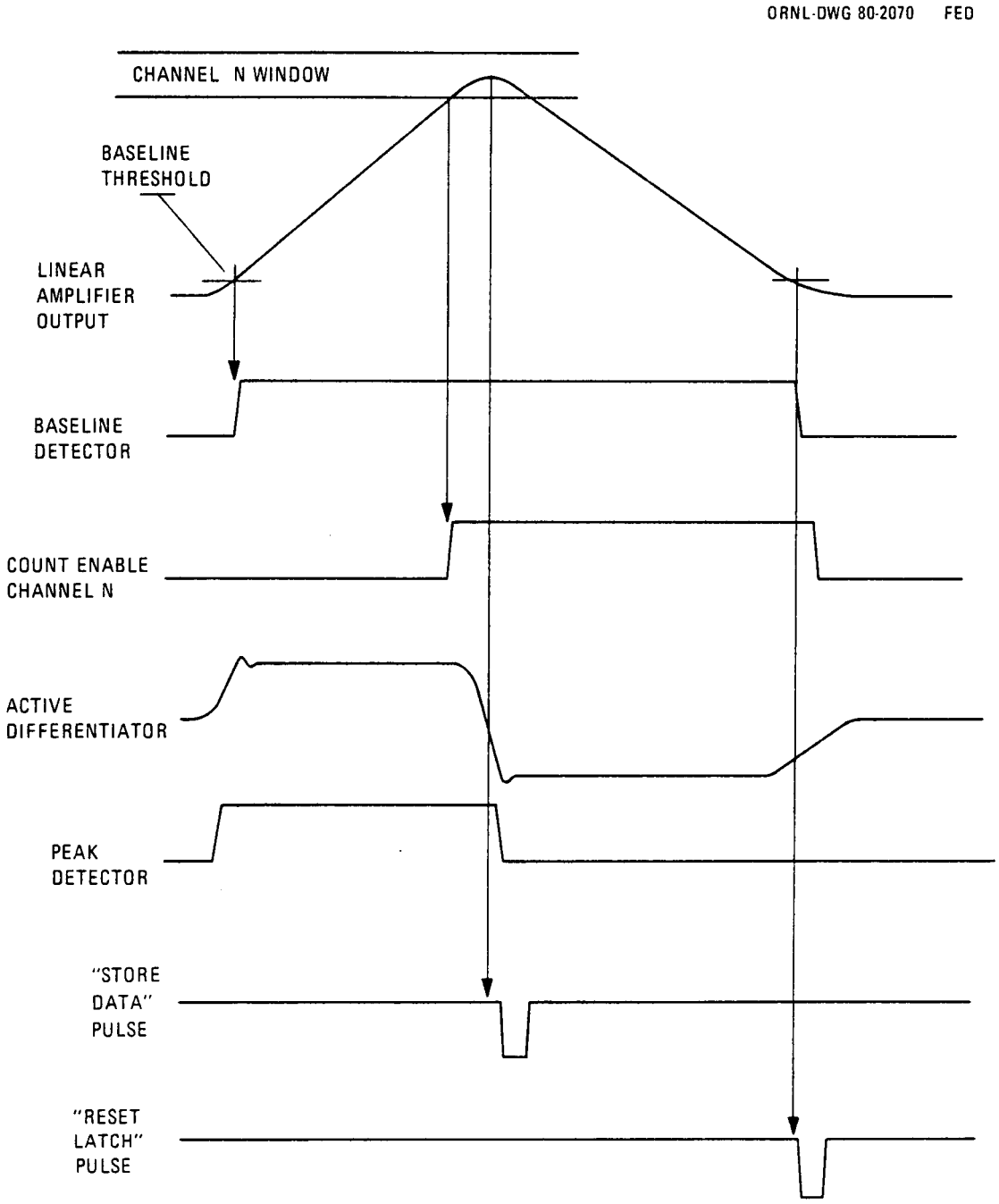

FIGURE A-11. The timing diagram for the pulse-height analysis

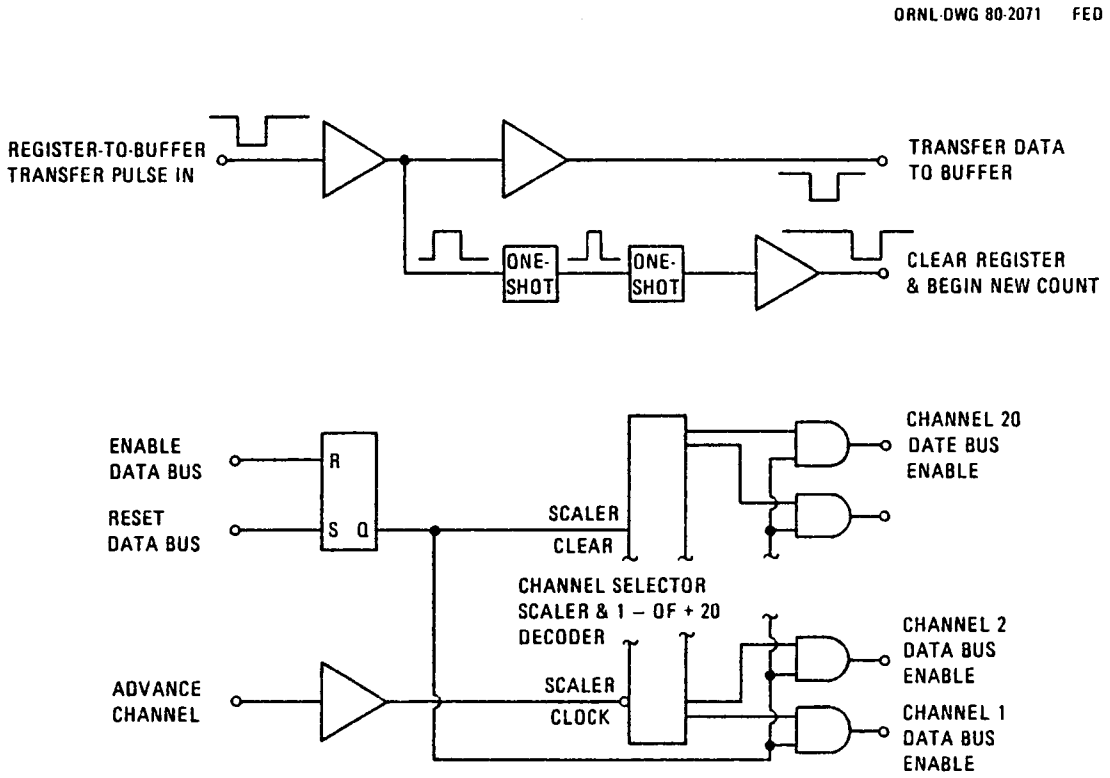

FIGURE A-12. A schematic diagram of the data transfer interface

transfer pulse to the interface; this transfers the counting register contents to the buffer and resets the counting registers. The transfer and reset pulses from the interface are each 1 μs long and are separated by 0.5 μs. The computer measures a 10-ms interval (the standard time interval per spectrum has been 10 ms for the history of the experiment) and sends another transfer pulse to the interface. The first spectrum enters the buffer, and the counting registers are reset and immediately begin to collect the second spectrum. (The 1-μs reset pulse introduces negligible dead time into the data accumulation interval.) As Fig. A-13 shows, the computer enables the data bus; and channel 1 data appears as the tri-state output of the first data buffer is activated. The computer reads this data and steps through succeeding channels by sending channel advance pulses to the interface channel selector scaler. When all channels have been read, the computer resets the channel-selector scaler and waits for the duration of the 10-ms counting interval before repeating the readout operation. Total readout time for 20 channels of data is approximately 100 μs. The computer is programmed to store a maximum of 25 spectra per plasma discharge.

A.3 COMPUTER SYSTEM

From the time the first spectra were recorded in November, 1976, the computer system has changed in several ways. The basic data collection is still done by the original PDP-8, but final data storage and processing have evolved through several stages along with the tokamak itself. The computer system for each tokamak version is briefly described below.

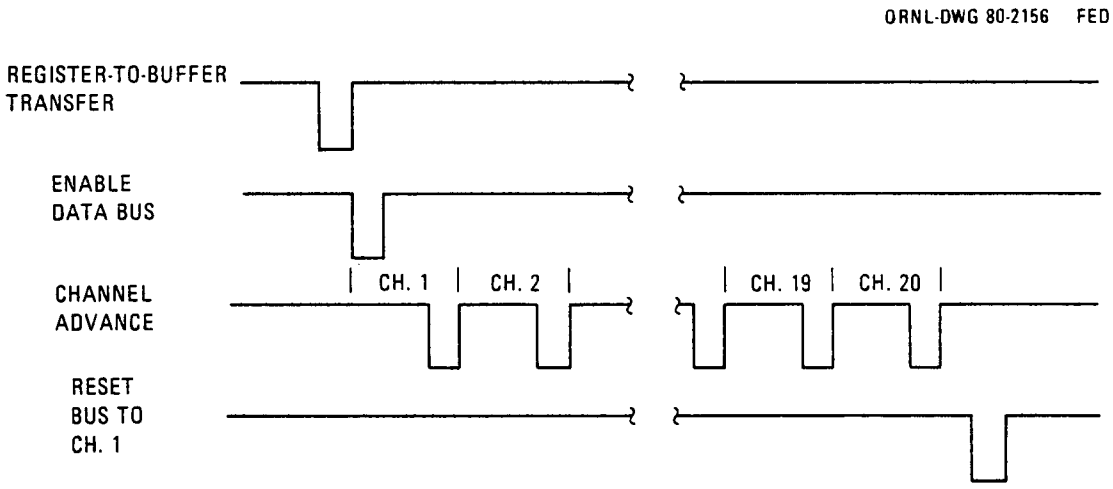

FIGURE A-13. A timing diagram for data transfer from the pulse-height analyzer to the PDP-8

A.3.1 ORMAK Computer System

The ORMAK computer system consisted of the PDP-8 with DECtape data storage and a CRT display. Initially, the computer was programmed to store a maximum of 20 spectra per plasma discharge and to display 400 (20 spectra with 20 data points each) unprocessed data points on the CRT screen. A reel of DECtape could hold data from 66 shots.

Data processing was done off-line. Fortran programs written for the PDP-8 performed weighted and unweighted least-squares linear fits to individual spectra and to summed data from several consecutive tokamak shots. Calculated temperatures were printed out on a teletype terminal.

A.3.2 ISX-A Computer System

The longer discharge times of ISX-A required an expansion to 25 spectra per discharge. As ISX-A began operation, the computer system was modified to store data on floppy disks instead of DECtape; a floppy disk could store 136 shots, even with the expanded format.

A Tektronix storage-CRT terminal was added to the system, and the programming was modified to allow data processing between tokamak discharges. Programs provided for printout of unprocessed data, calculation of electron temperature, plotting T_e vs time for a tokamak discharge, and plotting $\ell n(I)$ vs E for a selected spectrum. All data processing was carried out by the PDP-8.

A.3.3 ISX-B Computer System

The data-handling system was considerably expanded and modified as ISX-B was installed. The PDP-8 computer now operates in conjunction with a CAMAC data- handling system to transmit data from both the x-ray spectrometer and a pyroelectric radiometer to the Fusion Energy Division PDP-10 for storage and processing, following each plasma discharge. The data processing programs are still available at the minicomputer, but the PDP-10 is routinely used for data processing.

PDP-10 programs are available to print out unprocessed data, calculate T_e and Z_{eff} (using microwave interferometer electron density data) for each spectrum, and plot T_e and N_e vs time for a plasma discharge. The temperature calculation corrects for profile effects and pulse pileup and estimates peak temperature from spectrometer data. A quasi-three-dimensional plot of $\ell n(I)$ vs E vs t provides a quick check for non-thermal spectra, line radiation, and other undesirable features.

A.4 VACUUM AND COLLIMATION SYSTEM

The vacuum and collimation system for the x-ray energy spectrometer is illustrated in Fig. A-14. A vacuum path between plasma and detector is necessary to reduce attenuation of the thermal x-rays from the plasma. Since any attentuation in the 1-10 keV energy range must be considered in computing the true shape of an energy spectrum, the system is designed to open directly into the tokamak vacuum vessel. This arrangement eliminates all absorbers between the plasma and the detector except for the beryllium cryostat window.

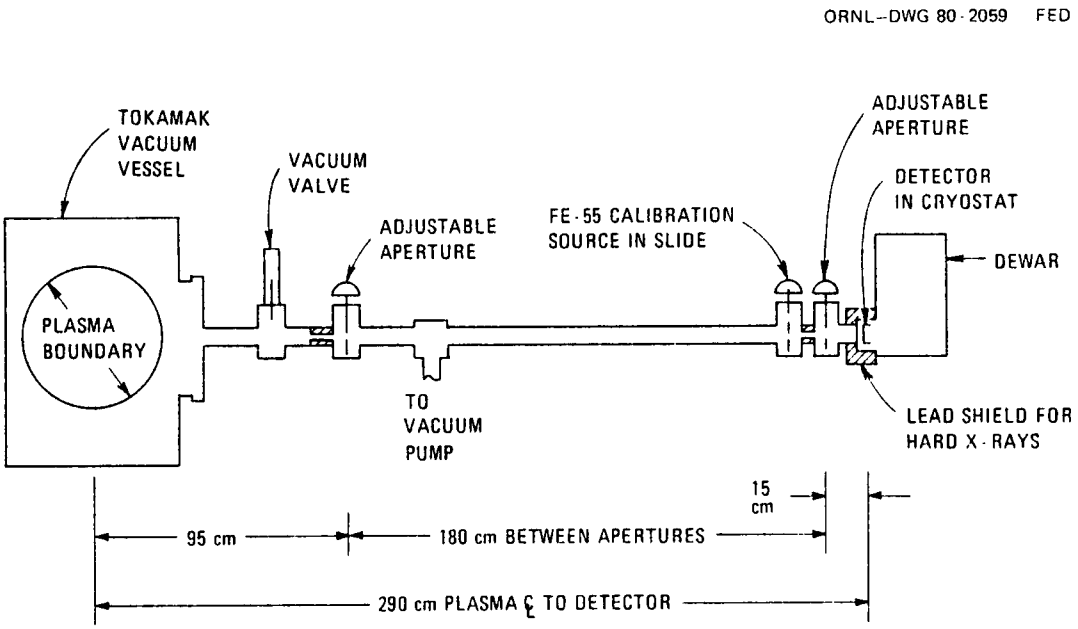

FIGURE A-14. The arrangement of the vacuum and collimation system for the x-ray energy spectrometer on ISX

This window is only 0.012-mm thick, so it does not seriously attenuate the lowest energy of interest.

The mechanical arrangement of the detector, apertures, and tokamak vacuum vessel defines the plasma volume which illuminates the detector. In the original system used on ORMAK, fixed collimating apertures were employed; experience with that system revealed the need for adjustable apertures to provide optimum counting rate to the spectrometer. In the present system, each of two apertures is adjustable from 0.033 cm to 0.528 cm in five binary steps. A third slide carries an iron-55 x-ray source which can be moved in front of the detector to check energy calibration.

An absolute intensity calculation for the spectrometer system must be made to find plasma impurity levels, so it is necessary to compute the plasma volume within the detector field of view as well as the solid angle subtended at the plasma by the detector. The system components relevant to these calculations are shown in Fig. A-15. Apertures d_1 and d_2 ($d_1 > d_2$) define the illuminating plasma volume. This volume is a thin truncated cone, but is approximated in the following calculations by a cylinder with a diameter equal to that of the cone at the plasma center line.

A basic principle of photometry allows the flux incident on the detector to be treated as if it all originated within a thin disk located at the plasma center line.[75] At this location, the solid angle subtended by the detector is defined by aperture d_2 (since $d_2 \leq d_1$), for any point within diameter d_a, as

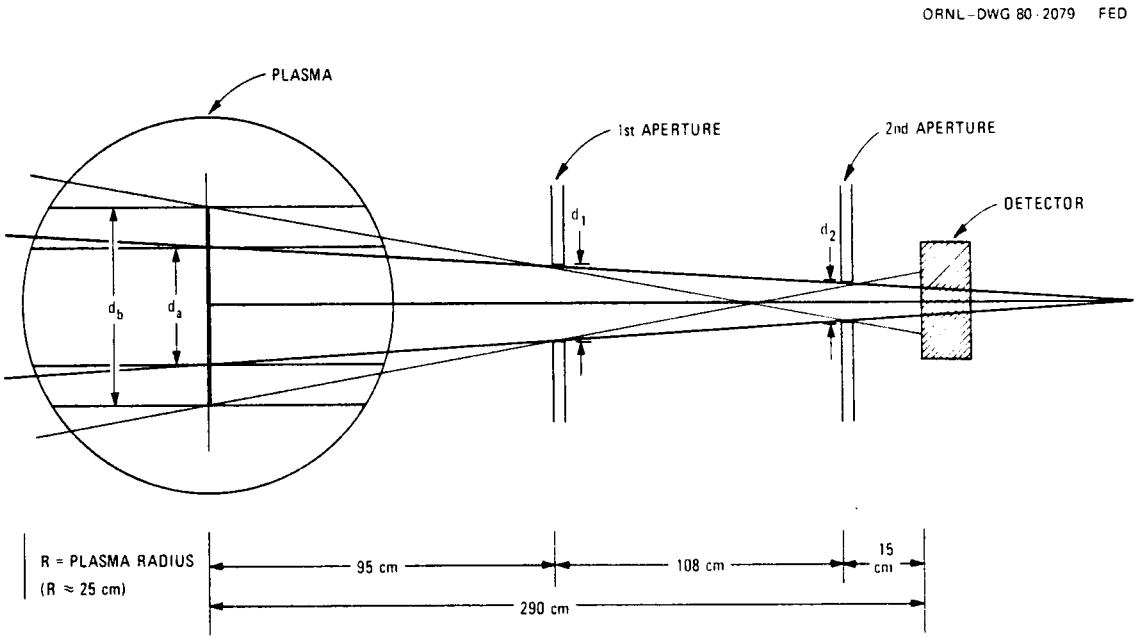

FIGURE A-15. The detector-plasma geometry for ISX

$$\Omega = \frac{\pi \left(\frac{d_2}{2}\right)^2}{(275)^2} \qquad (2\text{-}5)$$

On the annulus between r_a (= $d_a/2$) and r_b the solid angle is reduced by the intrusion of the edge of aperture d_1 into the line of sight. Figure A-16 illustrates this effect. The solid angle ω is reduced in this region by the fraction f of the detector which remains visible, becoming $\omega' = f\omega$, or

$$\omega' = \frac{2\omega}{\pi} (\alpha - \sin \alpha \cos \alpha) \qquad (A\text{-}6)$$

where α depends on the radial location within the annulus. For radius r, $r_a \leq r \leq r_o$,

$$\alpha = \cos^{-1} \frac{r - r_a}{r_b - r_a} \qquad (A\text{-}7)$$

Thus, within the plasma disk of diameter d_a, the total solid angle ω is visible; this part of the plasma fully illuminates the detector area visible through d_2. In the annulus, ($r_a \leq r \leq r_b$), the solid angle is reduced by the factor f, so the visible detector area is partially illuminated by plasma within the annulus. Outside the disk

ORNL–DWG 80-2060 FED

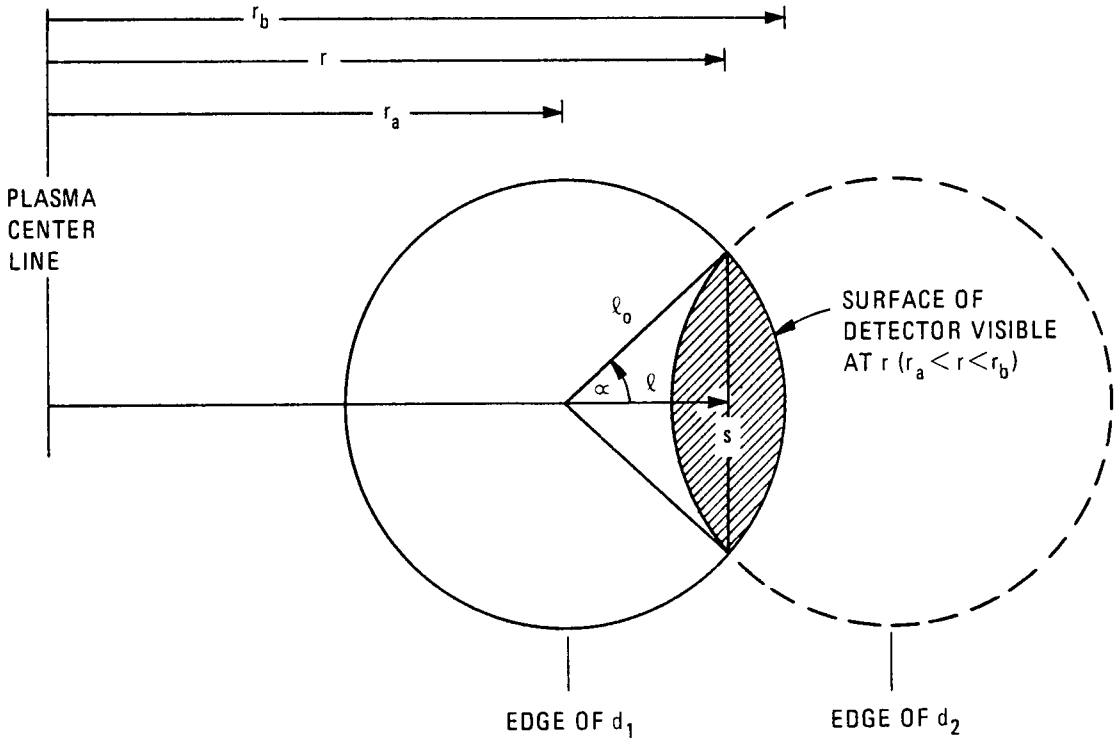

$$s = 2\left\{\int_{-\alpha}^{\alpha} d\theta \int_{0}^{\ell_0} r\,dr - \ell_0 \sin\alpha\ \ell_0 \cos\alpha\right\}$$

$$s = 2\ell_0^2\,(\alpha - \sin\alpha\cos\alpha)$$

$$\ell = r - r_a \qquad \ell_0 = r_b - r_a \qquad \alpha = \cos^{-1}\left(\frac{\ell}{\ell_0}\right)$$

FRACTION OF DETECTOR ILLUMINATED:

$$f = \frac{s}{\pi\ell_0^2} \text{ OR } f = \frac{2}{\pi}(\alpha - \sin\alpha\cos\alpha)$$

FIGURE A-16. The fraction of the detector area visible from the plasma annulus ($r_a \leq r \leq r_b$)

diameter d_b, the detector is shielded from the plasma, so radiation from this region does not illuminate the detector at all.

The shading of the plasma annulus by aperture d_1 does not produce any change in the spectral quality of the radiated energy, but only a reduction in the intensity received at the detector from this region. The total flux incident on the detector from both the unvignetted central disk and from the annulus can be duplicated by that from an unvignetted disk of diameter d_p ($d_a \leq d_p \leq d_b$) just enough larger than d_a to contribute an additional flux equal to that from the annulus. Thus

$$\Omega \cdot \pi \, r_p^2 = \Omega \cdot \pi r_a^2 + 2\pi \int_{r_a}^{r_b} r dr \cdot \Omega \cdot \frac{2}{\pi} (\alpha - \sin\alpha \cos\alpha) \qquad \text{(A-8)}$$

and the effective diameter of the plasma volume which illuminates the area of the detector subtended by the solid angle ω is

$$d_p = 2 \left\{ (r_a)^2 + \frac{4}{\pi} \int_{r_a}^{r_b} r(\alpha - \sin\alpha \cos\alpha) \, dr \right\}^{\frac{1}{2}} \qquad \text{(A-9)}$$

Given the sizes of d_1 and d_2 and the distances separating the plasma center line, apertures and detector, numerical values can be found for d_a, d_b, d_p and Ω. Formulas for d_a and d_b are

$$d_a = d_2 + \frac{275}{180} (d_1 - d_2) \qquad \text{(A-10)}$$

and

$$d_b = d_1 + \frac{95}{180}(d_1 + d_2) \qquad \text{(A-11)}$$

For possible combinations of d_1 and d_2, Table A-2 lists the geometrical parameters of the collimation system.

While the general arrangement of the ORMAK collimation system was similar to that of ISX, the geometrical parameters were different. Figure A-17 illustrates the ORMAK geometry. The relevant parameters for ORMAK are d_1 = 0.380 cm, d_2 = 0.033 cm, d_a = 0.793 cm, d_b = 0.871 cm, d_p = 0.826 cm, and $\Omega = 1.98 \times 10^{-8}$ steradians.

TABLE A-2. Geometrical parameters for the ISX collimation system

d_1(cm)	d_2(cm)	d_a(cm)	d_b(cm)	d_p(cm)	Ω(Steradians)
.528	.528	.528	1.085	.778	2.90×10^{-6}
.528	.264	.667	.946	.789	7.24×10^{-7}
.528	.132	.737	.876	.797	1.81×10^{-7}
.528	.066	.772	.842	.802	4.52×10^{-8}
.528	.033	.789	.824	.804	1.13×10^{-8}
.264	.264	.264	.543	.389	7.24×10^{-7}
.264	.132	.334	.473	.395	1.81×10^{-7}
.264	.066	.369	.438	.399	4.52×10^{-8}
.264	.033	.386	.419	.400	1.13×10^{-8}
.132	.132	.132	.271	.195	1.81×10^{-7}
.132	.066	.167	.233	.196	4.52×10^{-8}
.132	.033	.184	.219	.199	1.13×10^{-8}
.066	.066	.066	.136	.097	4.52×10^{-8}
.066	.033	.083	.118	.098	1.13×10^{-8}
.033	.033	.033	.068	.049	1.13×10^{-8}

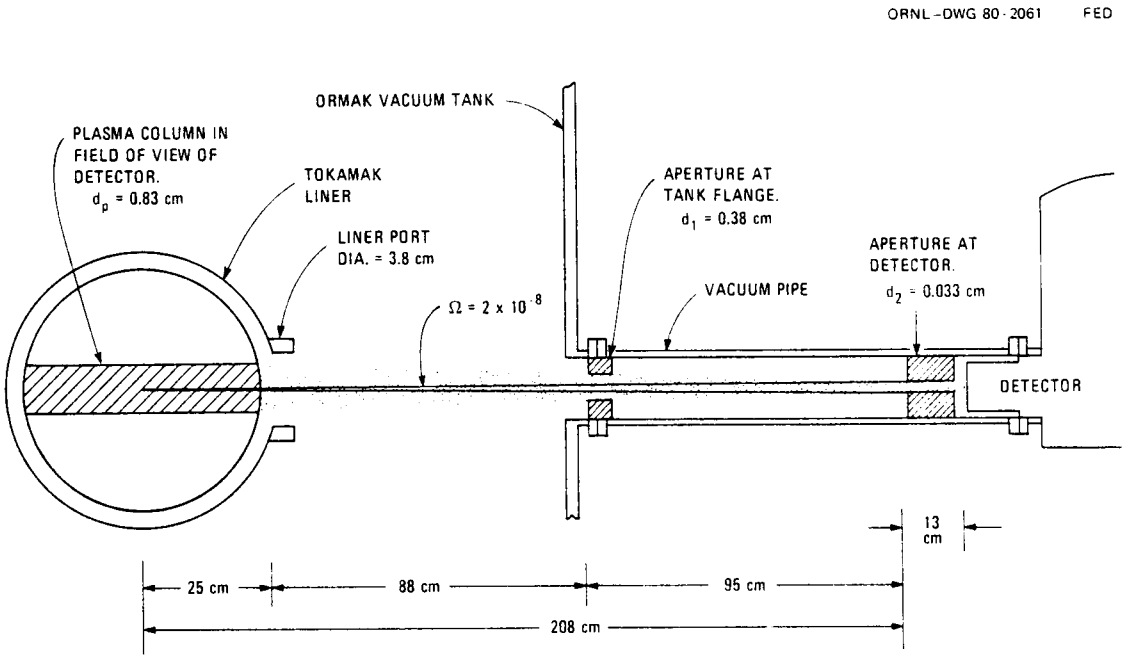

FIGURE A-17. The detector-plasma geometry for ORMAK

APPENDIX B

EFFECTS OF PILEUP ON TEMPERATURE MEASUREMENTS[76]

B.1 INTRODUCTION

When the present x-ray energy spectrometer is operating at high count rates (10^5 per second), some pulse pileup is inevitable. Effective pileup rejection requires a prompt inspection signal which is short compared with the data pulse resulting from the same detected photon.[77,78] Since the data pulse and preamplifier output rise times are approximately the same, no prompt signal is available. Because applicable pileup rejection methods are only partially effective, it is desirable to know how much pileup can be tolerated in experimental spectra without seriously affecting the results of data analysis.

Pileup occurs when a second photon is detected within the duration of a given pulse. The resulting composite pulse may be analyzed by the spectrometer and stored along with single-photon pulses, distorting the true energy spectrum. The pulse shape produced by the linear amplifier is shown in Fig. B-1, along with superimposed square and triangular pulse shapes of approximately the same duration. The expected spectral distortions for a square pulse represent a "worst-case" limit on pileup distortion, since any overlap results in maximum pileup. The triangular pulse is a compromise between realistic shape and mathematical tractability, and results of the triangular pulse model should more nearly predict experimental pileup effects.

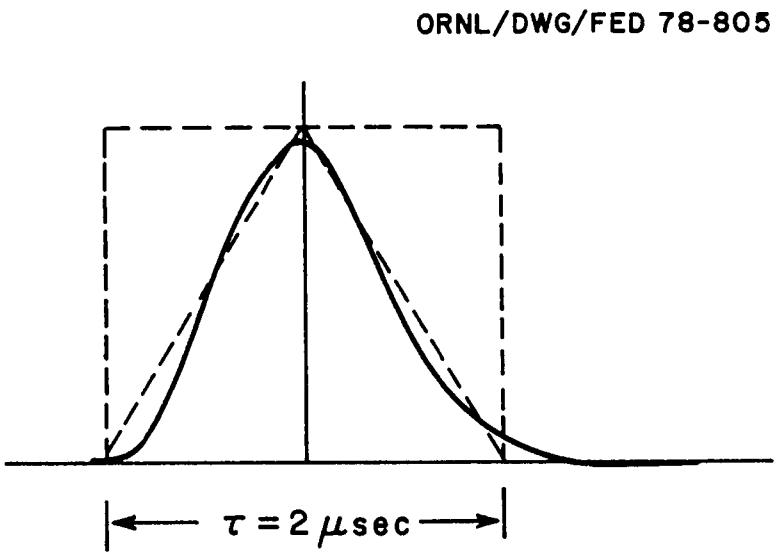

FIGURE B-1. Typical amplifier pulse shape, with square and triangular pulses of similar duration

B.2 SQUARE-PULSE PILEUP

The intensity distribution of photons from plasma bremsstrahlung and recombintation radiation has the form[79]

$$I(E) = \begin{cases} 0\ , \ E \leq E_o \\ \\ C' \ e^{-E/T_e}, \ E \geq E_o \end{cases} \qquad \text{(B-1)}$$

where electron and ion density, ion charge, and electron temperature are assumed constant. The cutoff energy E_o models the effect of the beryllium entrance window of the detector; in this analysis $E_o = 10^3$ eV. The normalized photon distribution function, f(E), is defined as

$$f(E) = \begin{cases} 0, \ E \leq E_o \\ \\ (C/E) \ e^{-E/T^e}, \ E \geq E_o \end{cases} \qquad \text{(B-2)}$$

This function is normalized,

$$\int_{E_o}^{\infty} f(E) \, dE = 1 \qquad \text{(B-3)}$$

and is related to the intensity distribution by the equation

$$I(E) = N_o \; E \; f(E) \qquad \text{(B-4)}$$

where N_o is the total number of photons in a spectrum. Thus, $N_o \; E \; f(E) \; dE$ gives the number of photons in the energy range $(E, E + dE)$.

Pulse pileup distorts the number distribution function of Eq. (B-2). Assume that each photon with energy E produces a square pulse of height E and width τ, and let the mean time between pulses be T. Given a first pulse, a second pulse starting within the interval 2τ piles up on the first [see Fig. B-2]. Both pulses are lost from their correct positions in the energy spectrum, and a single sum pulse is produced at energy

$$E_{sum} = E_1 + E_2 \qquad \text{(B-5)}$$

The expected number of single and sum pulses in a measured spectrum may be derived by Poisson statistics.[80] The number of single pulses expected is

$$N_1 = N_o \; e^{-2\tau/T} \qquad \text{(B-6)}$$

and the number of two-pulse sums is

$$N_2 = 0.5 \; N_o \; (2\tau/T) \; e^{-2\tau/T} \qquad \text{(B-7)}$$

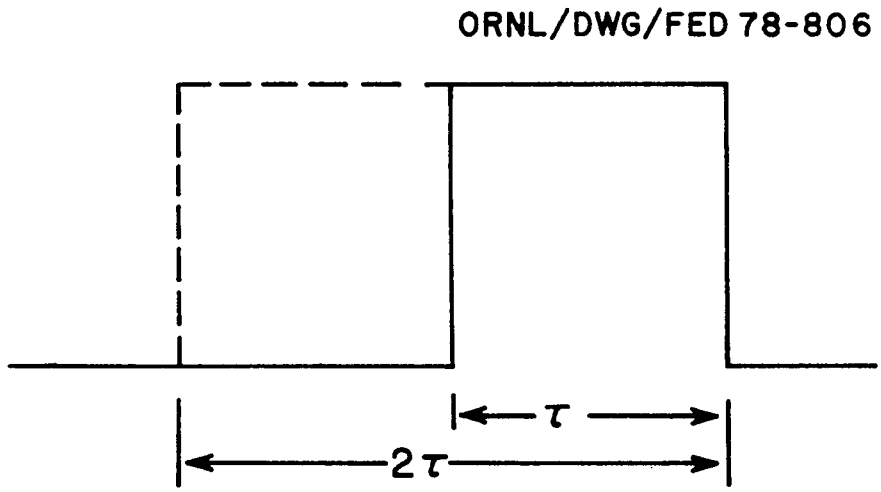

FIGURE B-2. A square pulse and the associated time interval during which pileup occurs

where the factor 0.5 accounts for the two pulses in the sum. Note that N_1 and N_2 are independent of energy. If the pileup fraction K is defined as

$$K = \tau / T \tag{B-8}$$

then for $K << 1$, Eqs. (B-6) and (B-7) can be expressed as expansions. To first order in K,

$$N_1 = N_o \ (1 - 2K) \tag{B-9}$$

and

$$N_2 = N_o \ K \tag{B-10}$$

Note that in this approximation, $N_1 + 2N_2 = N_o$, so for the condition $K << 1$, pileup events involving more than two photons are neglected.

An expression for the expected number of single-photon pulses having energy in (E, E + dE) may now be written as

$$d\, n_1(E) = N_1 \, f(E) \, dE. \tag{B-11}$$

The total energy of a two-photon sum pulse must satisfy Eq. (B-5), so for component energies E_1 and E_2,

$$E_2 = E - E_1. \tag{B-12}$$

For a fixed value of E_1, E_2 must be in $(E - E_1, E - E_1 + dE)$ in order to produce a sum pulse in $(E, E + dE)$. The expected number of pileup pulses $dn_2(E)$ with energies in $(E, E + dE)$ is found by integrating over the possible combinations of constituent pulses:

$$dn_2(E) = N_2 \, dE \int_{E_o}^{E-E_o} f(E_1) \, f(E - E_1) \, dE_1 \tag{B-13}$$

Equation (B-13) is analytic for the form of f(E) given by Eq. (B-2), so $dn_2(E)$ becomes

$$dn_2(E) = \begin{cases} 0 \, , & E \leq 2E_o \\ \\ 2 \, C \, N_2 \, f(E) \, dE \, \ell n \, \dfrac{E - E_o}{E_o} \, , & E \geq 2 \, E_o \, . \end{cases} \tag{B-14}$$

The total expected number of pulses dn(E) counted in $(E, E + dE)$ is obtained by combining Eqs. (B-11) and (B-14):

$$dn(E) = dn_1(E) + dn_2(E)$$

or

$$dn(E) = \begin{cases} N_o\, f(E)\, dE\, (1 - 2K), & E \leq 2E_o \\ \\ N_o\, f(E)\, dE\, \left(1 - 2K + 2CK \ln \dfrac{E - E_o}{E_o}\right), & E \geq 2E_o \end{cases} \qquad \text{(B-15)}$$

If an energy distribution function f(E), which includes the distortions due to pileup, is postulated to satisfy the equation

$$dn(E) = N_o\, f'(E)\, dE$$

then f'(E) can be identified from Eq. (B-15) as

$$f'(E) = \begin{cases} f(E)\, (1 - 2K), & E \leq 2E_o \\ \\ f(E)\, \left(1 - 2K + 2CK \ln \dfrac{E - E_o}{E_o}\right), & E \geq 2E_o \,. \end{cases} \qquad \text{(B-16)}$$

The expression for electron temperature T_e can be derived from Eq. (B-1):

$$T_e = - \left[\frac{d\,[\ell n\, I(E)]}{dE} \right]^{-1} \qquad \text{(B-17)}$$

Since ℓn I vs E is linear, T_e is independent of energy. If an intensity distribution function which includes pileup distortion is defined as

$$I'(E) = N_o\, E\, f'(E) \qquad \text{(B-18)}$$

in analogy with Eq. B-4, Fig. B-3 shows that $\ell n(I')$ vs E is approximately linear for higher values of E. The general behavior of $(T_e)d$, a temperature derived from an intensity spectrum distorted by pileup, is found as follows: select minimum and maximum energy limits for $\ell n(I')$ data, and fit a straight line to the $\ell n(I')$ vs E curve at intervals ΔE, using the standard linear least- squares method. Take the negative inverse slope of this line as $(T_e)d$. $(T_e)d$ is thus a function of the energy limits selected and the pileup fraction K. For the plots of $(T_e)d$ given in Fig. B-3, the upper energy limit is fixed at 8 keV, ΔE = 0.5 keV to correspond to experimental channel spacing, and $(T_e)d$ is plotted as a function of the minimum energy limit for various values of K.

From Fig. B-3a, $(T_e)d$ remains within 14% of the true value (T_e = 500 eV) even for K = 0.4, if the minimum energy limit is kept above 2.5 keV. Below this limit, the plots of $\ell n(I')$ vs E become sharply

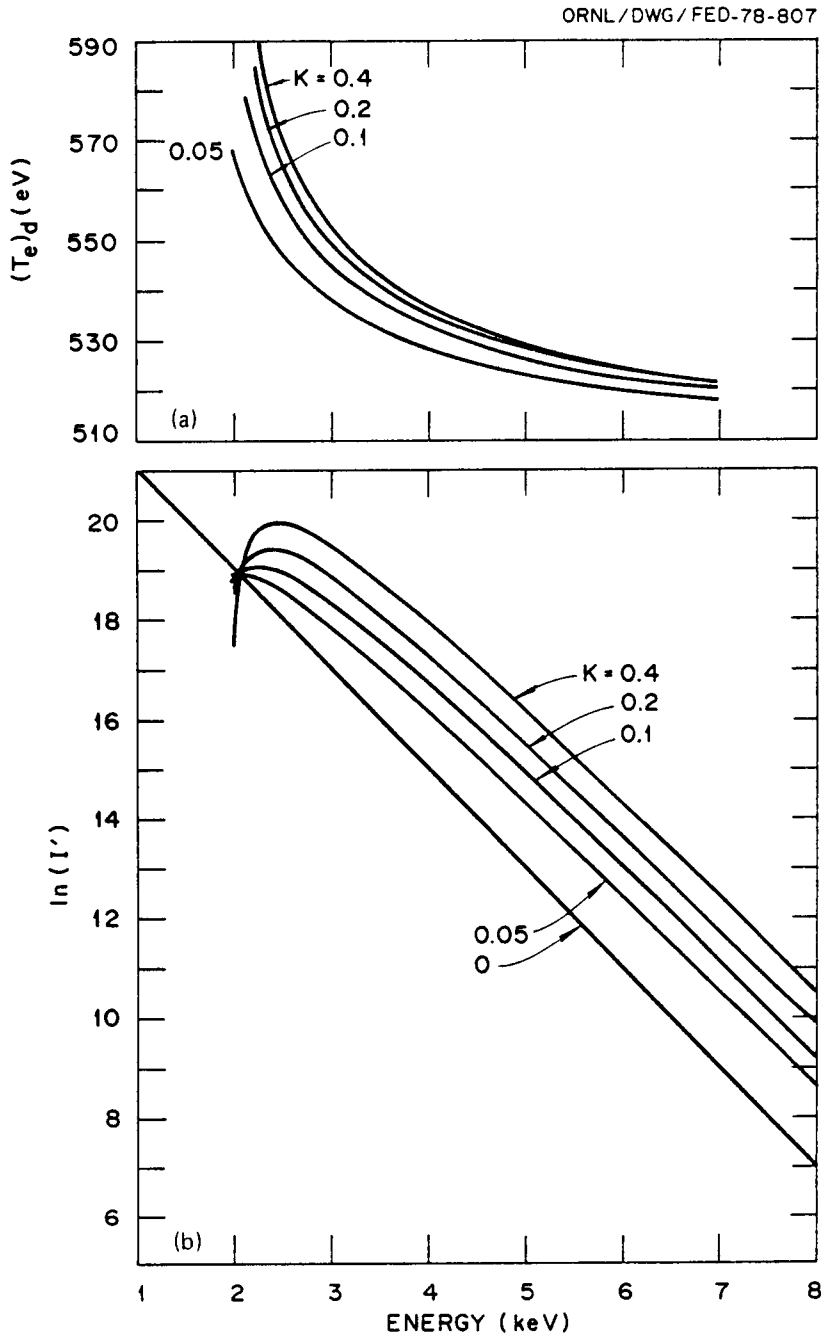

FIGURE B-3. Derived T_e and intensity vs energy for the square-pulse model, for various pileup fractions and temperatures

a. Derived T_e vs E for T_e = 500 eV
b. ℓn (I′) vs E for T_e = 500 eV

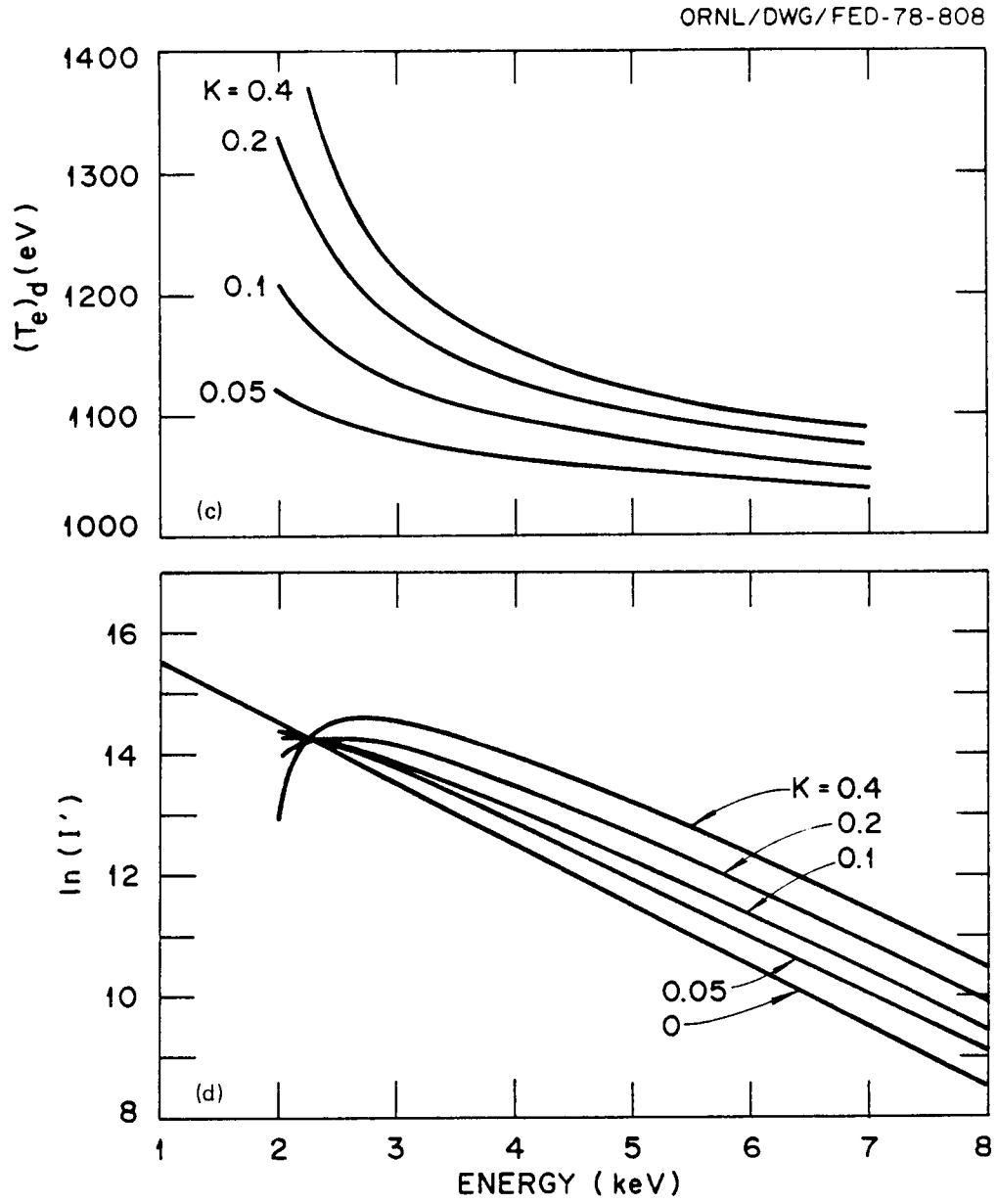

FIGURE B-3 (Continued)

c. Derived T_e vs E for T_e = 1 keV
d. ℓn (I′) vs E for T_e = 1 keV

nonlinear; so this part of the spectrum should not be used in temperature deviations, according to the square-pulse model. At a temperature of 1 keV, the nonlinearity in $\ell n(I')$ extends to higher energies, but for a minimum energy limit of 3 keV, $(T_e)d$ is still within 22% of T_e for K = 0.4.

B.3 TRIANGULAR-PULSE PILEUP

The foregoing treatment based on a square pulse gives worst-case results, since any overlap at all between pulses results in the maximum sum amplitude. A more realistic analysis may be performed by using the symmetrical triangular pulse sketched in Fig. B-1; this pulse represents a good compromise between physical realism and analytic simplicity.

A review of the pulse-height analysis process for the triangular pulse aids in understanding the pileup distortion associated with this model. The pulse-height analyzer examines each input pulse for a positive-to-negative slope transition; the first such transition in a pulse is identified as the peak, and subsequent transitions are ignored until the analyzer input falls below a preset baseline level. Thus, if pulse peaks are separated by a time $t \geqslant \tau$, each pulse is properly analyzed and stored. For peak separations in the interval $\tau/2 \leqslant t \leqslant \tau$, the first pulse is properly analyzed but the second pulse is lost. For peak separations $t \leqslant \tau/2$, the analyzer registers a piled-up pulse.

Since the effect of pulse pileup is to remove some single pulses from their true place in a spectrum and to insert sum pulses where

they do not belong, a number distribution function f'(E) which includes pileup effects is defined as

$$f'(E) = f(E) - f_{\ell}(E) + f_{g}(E) \qquad \text{(B-19)}$$

where f(E) is the undistorted function of Eq. (B-2), $f_{\ell}(E)$ accounts for losses from the true spectrum, and $f_{g}(E)$ is the sum- pulse gain term. As previously, only two-pulse pileup is considered.

B.3.1 Pileup Loss Term

The loss term is calculated by evaluating the probability that a given pulse with energy E is counted at some other energy, or is lost from the spectrum entirely; Fig. B-4 illustrates these circumstances. A preceding pulse beginning within the time interval (a) with respect to the given pulse causes the given pulse to be ignored by the analyzer, since the baseline is not reached between pulses. The probability that a preceding pulse begins within interval (a) is

$$P_{a} \simeq \tau/2T = 0.5\ K. \qquad \text{(B-20)}$$

A preceding pulse starting within interval (b) combines with the given pulse to produce a sum pulse, and again the given pulse is not counted correctly. The probability that this will happen is

$$P_{b} \simeq \tau/T = K \qquad \text{(B-21)}$$

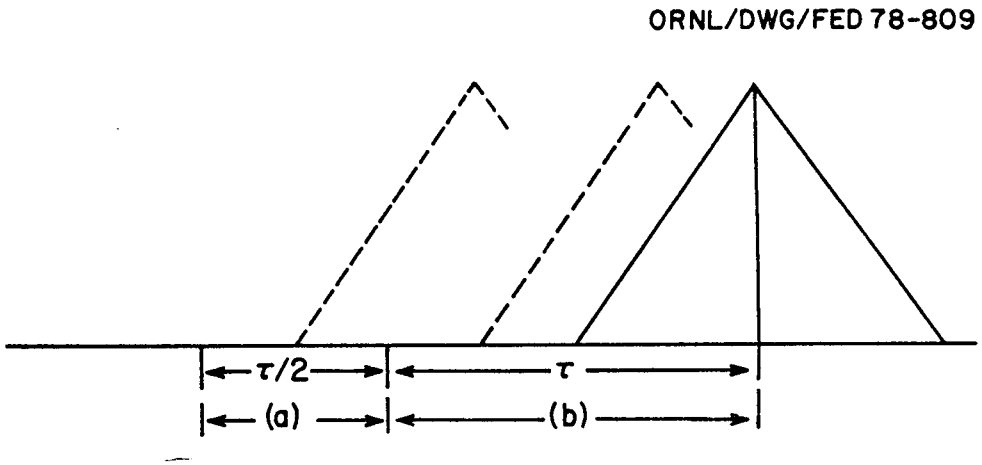

FIGURE B-4. A triangular pulse and associated time intervals during which loss and pileup occur

A pulse may start anywhere outside the intervals (a) and (b) without affecting the correct analysis of the given pulse. Thus, the counting loss at energy E due to pileup is

$$f_\ell(E) = f(E)\ (P_a + P_b)$$

or

$$f_\ell(E) = \frac{3}{2} K\, f(E)\ . \qquad \text{(B-22)}$$

B.3.2 Pileup Gain Term

Next, consider the gain term. A sum pulse of amplitude E_s can be produced by a range of component pulses, depending on the degree of overlap as well as component energy. Since all pulses have the same duration, the sum peak is always detected at the peaking time of the higher energy component; thus, it is convenient to express the sum pulse energy as

$$E_s = E_h + \alpha\, E_\ell \qquad \text{(B-23)}$$

where α is the degree of overlap of the component pulses and E_h and E_ℓ are the energies of the greater and smaller constituent pulses, respectively. It is obvious that E_s can be no smaller than E_o or $E_s/2$, whichever is greater, so the following relations hold:

$$\left.\begin{matrix} E_s/2 \\ \\ E_o \end{matrix}\right\} \leq E_h \leq E_s \qquad \text{(B-24)}$$

and

$$\left.\begin{matrix} E_s - E_h \\ \\ E_o \end{matrix}\right\} \leq E_\ell \leq E_h \qquad \text{(B-25)}$$

The pileup gain term contains a double integral, since the higher energy pulse can range from $E_s/2$ to E_s in amplitude and each value of E_h can sum with a range of E_ℓ amplitudes, depending on the value of α. Figure B-5 details the relation between the sum pulse and its components. From Eq. (B-23)

$$\alpha E_\ell = E_s - E_h \qquad \text{(B-26)}$$

and from Fig. B-5,

$$\alpha = 2t/\tau \qquad \text{(B-27)}$$

ORNL/DWG/FED 78-810

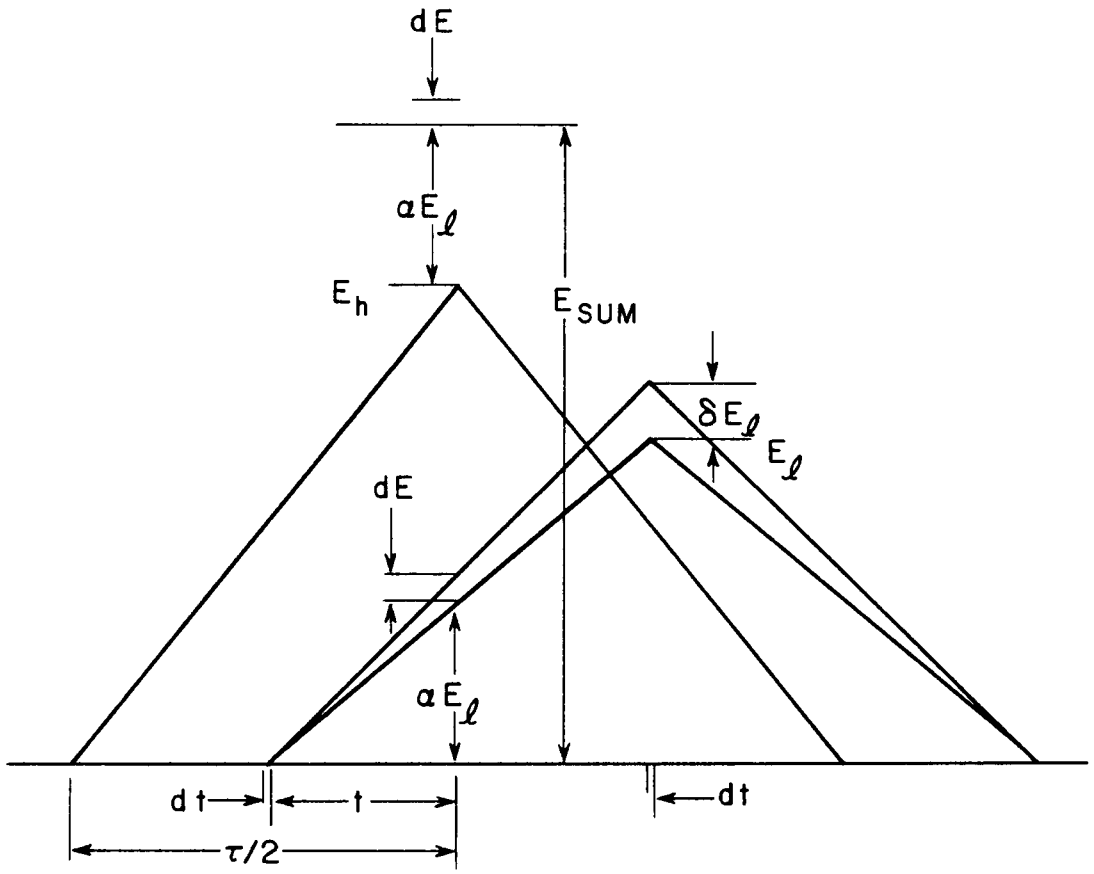

$\alpha = 2t/\tau$

$dE = \alpha \delta E_\ell$

$t = (\tau/2)\ \dfrac{E_{SUM} - E_h}{E_\ell}$

$t_{MAX} = \tau/2$

$t_{MIN} = (\tau/2)\ \dfrac{E_{SUM} - E_h}{E_h}$

$(E_\ell)_{MIN} = E_{SUM} - E_h$

$\alpha = 1$ for $(E_\ell)_{MIN}$

$(E_\ell)_{MAX} = E_h$

$\alpha = \dfrac{E_{SUM} - E_h}{E_h}$ for $(E_\ell)_{MAX}$

FIGURE B-5. A triangular sum pulse and its components

and

$$\alpha \, \delta \, E_\ell = dE \, . \tag{B-28}$$

Therefore, the probability that a pulse E_ℓ occurs in the interval (t, t + dt) with respect to the peak of the higher pulse and has the correct amplitude to sum with E_h to produce a pulse in the interval (E_s, E_s + dE) is

$$P_1 = f(E_\ell) \, \delta E_\ell \, \frac{dt}{T}$$

or

$$P_1 = (\tau/2T) \, f(E_\ell) \, \frac{dt}{T} \, dE \tag{B-29}$$

From Fig. B-5,

$$t = \frac{\tau}{2} \cdot \frac{E_s - E_h}{E_\ell} \tag{B-30}$$

and so

$$\frac{dt}{t} = \frac{dE_\ell}{E_\ell} \tag{B-31}$$

Combining Eqs. (B-29) and (B-31) produces

$$P_1 = (\frac{K}{2}\, dE)\, f(E_\ell)\, \frac{dE_\ell}{E_\ell} \tag{B-32}$$

The probability P_2 that any pulse within the range of E_ℓ will pile up with E_h to produce a sum pulse in the interval (E_s, E_s + dE) is found by integrating P_1 over the range of E_ℓ:

$$P_2 = \frac{K}{2}\, dE \int_{E_s-E_h}^{E_h} f(E_\ell)\, \frac{dE_\ell}{E_\ell} \tag{B-33}$$

Finally, the probability P_s that two pulses will sum to E_s within the interval dE is

$$P_s = f_g(E_s)\, dE = 2 \int_{E_s/2}^{E_s} P_2\, f(E_h)\, dE_h \,. \tag{B-34}$$

The factor of two in Eq. (B-34) is inserted because the lower energy pulse may sum on either its leading or trailing edge to produce E_s. From Eq. (B-34), the pileup gain distribution function is

$$f_g(E_s) = K \int_{E_s/2}^{E_s} f(E_h)dE_h \int_{E_s-E_h}^{E_h} f(E_\ell) \frac{dE_\ell}{E_\ell} \qquad \text{(B-35)}$$

B.3.3 Distribution Function Including Pileup Effects

The distribution function including pileup effects is obtained by inserting Eqs. (B-22) and (B-35) into Eq. (B-19):

$$f'(E) = f(E) \left(1 - \frac{3}{2} K\right) + K \int_{E/2}^{E} f(E_h)\, dE_h \int_{E-E_h}^{E_h} f(E_\ell) \frac{dE_\ell}{E_\ell} \qquad \text{(B-36)}$$

The effect of pileup on the x-ray intensity spectrum as predicted by the triangular pulse model is found by substituting Eq. (B-2) in Eq. (B-36) and using the definition for $I'(E)$ given in Eq. (B-18). The derived temperature $(T_e)_d$ is evaluated by the least-squares procedure outlined previously. Plots of $\ell n(I')$ and $(T_e)_d$ vs E are given in Fig. B-6. Note that spectral distortion is not as severe in this case as for the square-pulse model, though the curves for $\ell n(I')$ vs E still become decidedly nonlinear at approximately the same energies as before. For a minimum energy of 2.5 keV and T_e = 500 eV, $(T_e)_d$ is within 5% of T_e even for K = 0.4. At T_e = 1 keV and a minimum energy limit of 3 keV, $(T_e)_d$ is within 8% of T_e at K = 0.4.

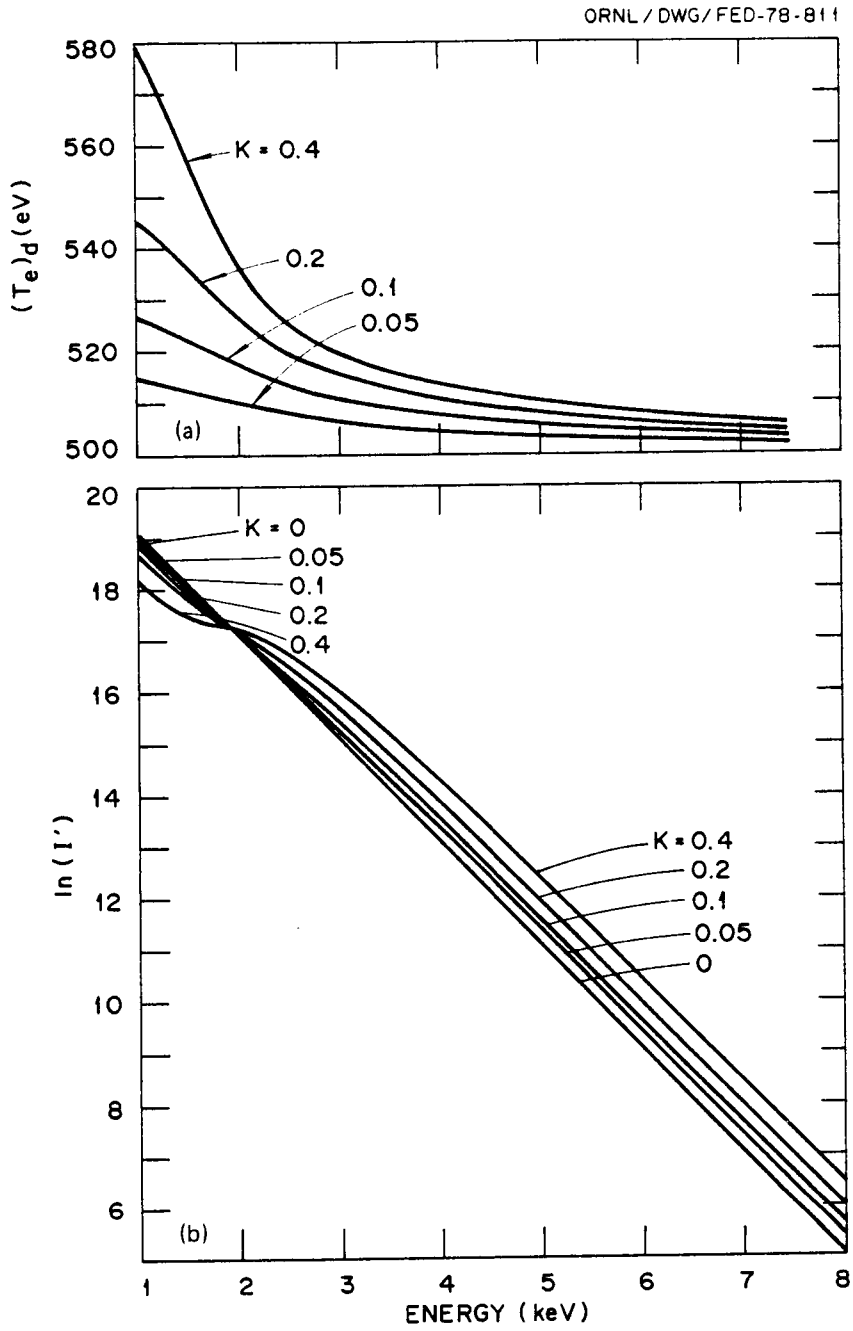

FIGURE B-6. Derived T_e and intensity vs energy for the triangular pulse model, for various pileup fractions and temperatures

a. Derived T_e vs E for T_e = 500 eV
b. ℓn (I′) vs E for T_e = 500 eV

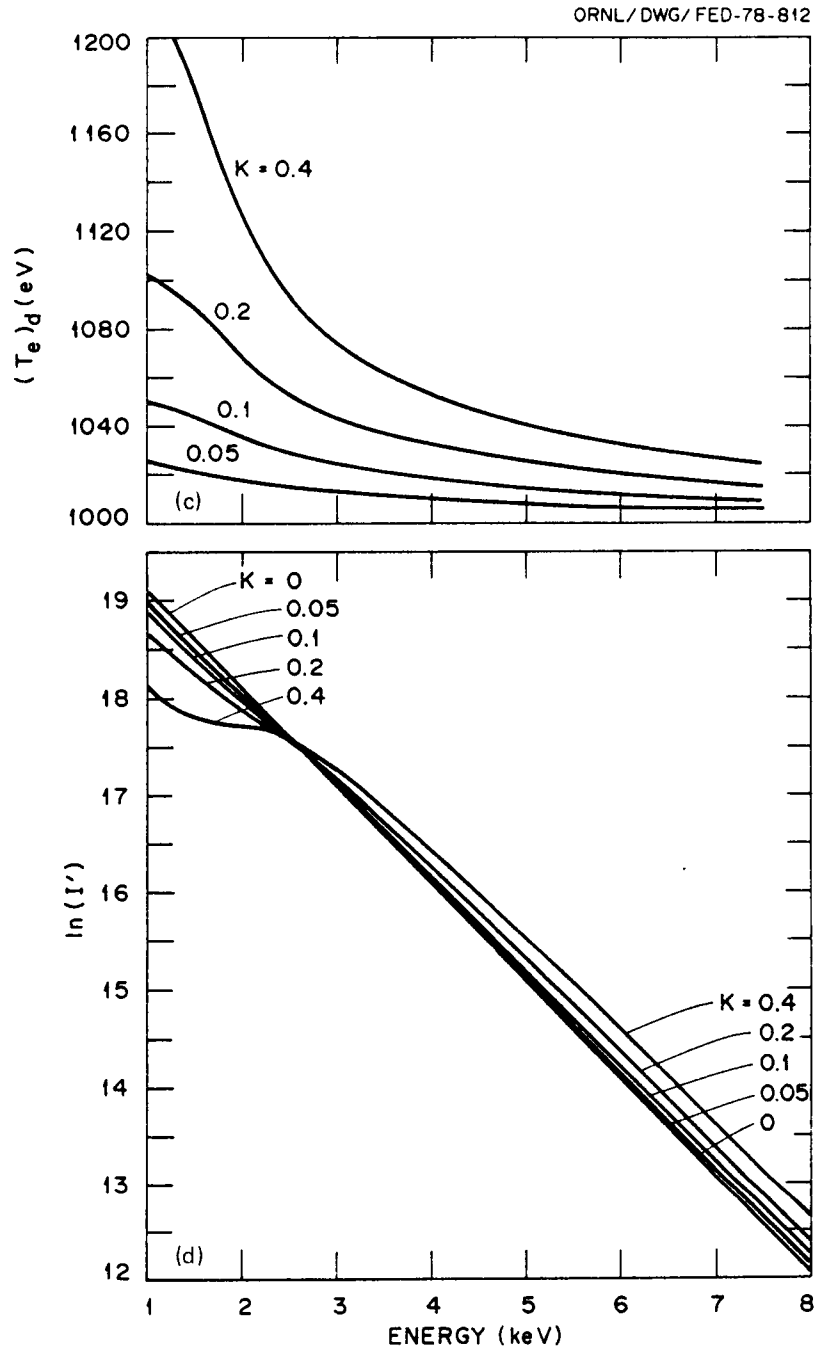

FIGURE B-6 (Continued)

c. Derived T_e vs E for T_e = 1 keV
d. ℓn (I′) vs E for T_e = 1 keV

B.4 CONCLUSIONS

Because the linear amplifier pulse shape in Fig. B-1 is approximated more closely by the triangular than the square pulse shape, the actual distortion of an x-ray intensity spectrum should be more accurately predicted by Fig. B-6. Both models are in qualitative agreement, showing that pileup does cause spectral distortion and should be minimized or avoided where possible. However, electron temperatures correct to within 10% can be derived from experimental data containing up to 40% pileup pulses, provided the badly distorted low-energy region of the spectrum is not used in the temperature derivation.

The similarity of the square and triangular pulse analytical conclusions suggests that small differences between real and assumed pulse shapes are not important. These results indicate that data from a single-detector energy spectrometer optimized for high-count-rate operation can be used even when the most desirable data collection rate is exceeded, so the effective dynamic range of the diagnostic is extended. The analysis assumes that detected radiation follows the exponential intensity expression of Eq. (B-1); where experimental conditions approximate this premise, good temperature derivations by x-ray analysis are possible even in the presence of considerable pileup.

APPENDIX C

SUMMARY OF DATA ANALYSIS PROCEDURES

C.1 INTRODUCTION

The analysis of energy spectrometer data to obtain numerical values for T_e and Z_{eff} must synthesize the operating characteristics and geometry of the equipment, the theory of radiation emission from the plasma, and the effects of several error sources. Since the discussion of these subjects is dispersed throughout several chapters and appendices, the relevant equations are collected here, and a concise outline of the analytical determination of T_e and Z_{eff} is given.

C.2 PROCEDURE FOR FINDING T_e

A single energy spectrum contains an array of numbers N_j, the counts recorded in channel j in a 10-ms counting interval. The average energy of channel j is

$$E_j = (\frac{1}{2} + 0.25) \text{ keV} \tag{C-1}$$

The x-ray intensity at E_j is found as the product

$$I_j = N_j E_j \tag{C-2}$$

and the logarithm of this intensity

$$\lambda_j = \ell n\ I_j \qquad \text{(C-3)}$$

is used in subsequent calculations.

If counting rate is too high, the experimental spectrum is distorted by pulse pileup, especially at lower energies. The spectrum is tested for pileup by comparing total counts in the spectrum with a table of predetermined limits. The most distorted low-energy channels are excluded from succeeding calculations to limit pileup-induced errors. For no more than 8% error in T_e due to pulse pileup, the lowest channel to be used in data analysis is given in Table C-1. Table C-1 is based on a pileup fraction

$$K = 10^{-4} \Sigma\ N_j \qquad \text{(C-4)}$$

A linear least-squares fit for the n points $(E_j,\ \lambda_j)$ in the spectrum, beginning with the lowest channel allowed by Table C-1, provides the chord-integrated temperature,

$$T_e(\text{chord}) = \frac{n(\Sigma\ E_j)^2 - \Sigma\ E_j^2}{n\ \Sigma\ E_j\ \Sigma\ \lambda_j - \Sigma\ E_j\ \lambda_j} \qquad \text{(C-5)}$$

and the zero-energy intercept

TABLE C-1. Lowest allowed channel vs total counts in a spectrum, for no more than 8% error in T_e from a least-squares fit

ΣN_n in 10 ms Spectrum	Pileup Fraction K	Lowest Allowed Channel in LSF
0-1500	0-0.15	2
1500-2000	0.15-0.2	3
2000-3000	0.2-0.3	4
3000-4000	0.3-0.4	5
≥4000	≥0.4	No calculation allowed

$$\lambda(E = 0) = \frac{\Sigma \lambda_j}{n} - \frac{\Sigma E_j}{n T_e(\text{chord})} \qquad \text{(C-6)}$$

The goodness of fit of the data points to the assumed straight line is tested by the coefficient of determination

$$\text{COD} = \frac{\left(n \Sigma E_j \lambda_j - \Sigma E_j \Sigma \lambda_j\right)^2}{\left(n \Sigma E_j^2 - (\Sigma E_j)^2\right)\left(n \Sigma \lambda_j^2 - (\Sigma \lambda_j)^2\right)} \qquad \text{(C-7)}$$

A linear fit is demonstrated when COD $\simeq$ 1; for COD $\leq$ 0.9, the spectrum needs to be examined for line radiation, non-Maxwellian components, or other features. The statistical reliability of the spectral data is tested by the variance of the slope

$$V = \frac{n \Sigma \lambda_j^2 - (\Sigma \lambda_j)^2}{n(n-2)} - \frac{\left(n \Sigma E_j \lambda_j - \Sigma E_g \Sigma \lambda_j\right)^2}{n(n-2)\left(n \Sigma E_j^2 - (\Sigma E_j)^2\right)} \qquad \text{(C-8)}$$

Since the temperature T_e is the negative inverse of the slope, the estimated standard deviation in T_e is

$$\text{SD} = \frac{V^{1/2}}{V - (1/T_e)^2} \qquad \text{(C-9)}$$

Finally, the chord-integrated value of T_e is corrected to give an estimate of the central value:

$$T_e(\text{central}) = y\ T_e(\text{chord}) \qquad \text{(C-10)}$$

where

$$y(\text{mean}) = 1.3 \times 10^{-4}\ T_e\ (\text{chord-integral, eV}) + 1.06 \qquad \text{(C-11)}$$

C.3 PROCEDURE FOR FINDING Z_{eff}

The ratio of observed x-ray intensity to the intensity expected from a pure hydrogen plasma is required to find Z_{eff}. The natural logarithm of the experimental intensity at the zero-energy intercept is found from the least-squares fit to the data points (E_j, λ_j). This quantity, given in Eq. (C-6), must be corrected for counting losses due to pileup. The fraction of total counts lost by pileup is given by K′, where K′ includes leading-edge pileup (which causes the spectral distortion mentioned in the last section) and trailing-edge pileup (which is rejected by the baseline inspection circuit in the pulse-height processor). For a symmetrical pulse shape, K′ = 2K, with K defined by Eq. (C-4). Since K′ of the total counts pile up, (1-K′) of the total is normal, and

$$I_{observed} = (1-K') \, I_{true} \tag{C-12}$$

Therefore the true λ extrapolated to zero energy is

$$\lambda(true) = \lambda(E = 0) - \ell n \, (1 - K') \tag{C-13}$$

where

$$K' = 2 \times 10^{-4} \, \Sigma \, N_j \tag{C-14}$$

Next, the expected intensity from a pure hydrogen plasma under identical conditions must be found. This calculation requires the values of T_e and N_e throughout the plasma. The x-ray spectrometer supplies the T_e value, but N_e must be obtained from a separate measurement by the microwave interferometer. This diagnostic supplies a chord-integral value of N_e, so peak N_e must be inferred from a model of the plasmaa profile; for plasma minor radius a,

$$a \, N_e(chord) = N_e(peak) \int_o^a (density \; profile \; function) \, dr$$

Thus, for a parabolic density profile,

$$N_e(peak) = 1.5 \, N_e(chord) \tag{C-15}$$

and for a triangular density profile,

$$N_e(\text{peak}) = 2\, N_e(\text{chord}) \tag{C-16}$$

The parabolic model is used routinely for Z_{eff} calculations.

Given peak values of N_e and T_e, and reasonable models for N_e (usually parabolic) and T_e (usually squared-parabolic) profiles, the x-ray intensity expected from pure hydrogen may be calculated for an energy interval corresponding to a spectrometer channel. This interval has been selected to correspond to channel 4.

$$I_H(\text{ch } 4) = C\, \Omega\, (dp)^2 \int_o^a N_e^2(r)\, T_e^{1/2}(r)\, \sinh \frac{250}{T_e(r)} \times e^{-2250/T_e(r)}\, dr \tag{C-17}$$

where

$$C = 2.4 \times 10^{-16} \tag{C-18}$$

$$N_e(r) = \left\{1 - \left(\frac{r}{a}\right)^2\right\} N_e(\text{peak}) \tag{C-19}$$

$$T_e(r) = \left\{1 - \left(\frac{r}{a}\right)^2\right\}^2 T_e(\text{peak}) \tag{C-20}$$

and Ω and (dp) are found in Appendix A, Table A-2 for specific aperture settings.

Since Eq. (C-17) is a classical bremsstrahlung calculation, the intensity obtained from it must be corrected for quantum-mechanical effects. The Gaunt factor for E = 2250 eV is given by the empirical formula

$$\ell n\ \bar{g}_{ff} = 0.26\ \ell n\ T_e(eV) - 2.08 \qquad (C-21)$$

so the corrected hydrogen intensity is

$$\lambda_H(2250) = \ell n\ I_H(2250) + \ell n\ \bar{g}_{ff} \qquad (C-22)$$

The extrapolated zero-energy point is

$$\lambda_H(E = 0) = \lambda_H(2250) + \frac{2250}{T_e(chord)} \qquad (C-23)$$

The enhancement η is the ratio of the observed intensity corrected for pileup effects to the hydrogen intensity, so

$$\ell n\ \eta = \lambda(true) = \lambda_H(E = 0) \qquad (C-24)$$

From the enhancement value, Z_{eff} can be estimated by the equation

$$Z_{eff} = 1 + \alpha(\ell n\ \eta)^{\beta} \qquad \text{(C-25)}$$

where

$$\alpha = (2.63 \times 10^{-7})\ T_e^{1.94} \qquad \text{(C-26)}$$

and

$$\beta = 3.75\ e^{-3.4 \times 10^{-4}\ T_e} \qquad \text{(C-27)}$$

Equation (C-25) is derived from an oxygen impurity model, with maximum Z_{eff} values of ~5.5. Therefore, calculated values in tables and plots of Z_{eff} are truncated to a maximum value of $Z_{eff} = 6$.

VITA

George Richard Dyer was born in Thomaston, Georgia on August 8, 1940. He attended Shepherd and John B. Gordon elementary schools, and graduated from R. E. Lee Institute in June, 1957. He attended Emory University in Atlanta, Georgia, and earned the Bachelor of Arts (1961) and Master of Science (1962) degrees there. In the fall of 1964 he enrolled as a part-time student at the University of Tennessee, Knoxville. He received the Doctor of Philosophy degree with a major in Physics in March, 1980.

Mr. Dyer is a member of Phi Beta Kappa, Sigma Xi, Sigma Pi Sigma, and the American Physical Society. His interests include astronomy, music, and electronics. He is employed in the Fusion Energy Division of the Oak Ridge National Laboratory.

He is married to Barbara Moore Dyer, of Gainesville, Georgia. They have two children, Virginia and Jefferson, live in Norris, Tennessee, and are active in the Andersonville Baptist Church.